In presenting the dissertation as a partial fulfillment of the requirements for an advanced degree from the Georgia Institute of Technology, I agree that the Library of the Institute shall make it available for inspection and circulation in accordance with its regulations governing materials of this type. I agree that permission to copy from, or to publish from, this dissertation may be granted by the professor under whose direction it was written, or, in his absence, by the Dean of the Graduate Division when such copying or publication is solely for scholarly purposes and does not involve potential financial gain. It is understood that any copying from, or publication of, this dissertation which involves potential financial gain will not be allowed without written permission.

7/25/68

FORMATION OF EXCITED HYDROGEN ATOMS BY CHARGE TRANSFER NEUTRALIZATION OF HIGH ENERGY PROTONS

A THESIS

Presented to

The Faculty of the Graduate Division

by

John Charles Ford

In Partial Fulfillment

of the Requirements for the Degree

Doctor of Philosophy

in the School of Physics

Georgia Institute of Technology

August, 1971

FORMATION OF EXCITED HYDROGEN ATOMS

BY CHARGE TRANSFER NEUTRALIZATION

OF HIGH ENERGY PROTONS

Approved:

Chairman

Date approved by Chairman: 25 August 1971

ACKNOWLEDGMENTS

I would like to express my gratitude to Dr. E. W. Thomas, who has served as faculty advisor to this thesis. His continual support and assistance have been most appreciated. I would also like to express my appreciation to Dr. D. W. Martin and Dr. T. F. Moran who served on the thesis reading committee; their suggestions and comments were responsible for many improvements in this manuscript.

The advice of Dr. J. L. Edwards was most helpful during the design of the present experiment. The assistance of Messrs. F. R. McCoy, O. E. Rausch, and R. J. Conrads in operating the experiment and reducing the data has been very valuable. Many thanks also go to Miss T. L. Sims for her help in the numerical analysis of the data.

Much of the success of this experiment was due to the high quality of workmanship in the construction of the various components of the experimental apparatus. I would, therefore, like to thank Messrs. J. D. Dameron, V. B. Reynolds, C. E. Cable, K. B. Springfield, and J. R. Bell for their contributions in fabrication of much of the apparatus. Many contributions to the assembly of the apparatus and electronic systems were made by Messrs. J. D. Dickey and M. Schacham.

I would also like to thank Mrs. Joyce Williams for the excellent typing of this thesis.

TABLE OF CONTENTS

TABLE OF CONTENTS (Continued)

TABLE OF CONTENTS (Continued)

TABLE OF CONTENTS (Concluded)

LIST OF TABLES

LIST OF TABLES (Continued)

LIST OF ILLUSTRATIONS

LIST OF ILLUSTRATIONS (Concluded)

ABSTRACT

The objective of this research was to measure with greater accuracy than heretofore possible the absolute cross section for the formation of atomic hydrogen in the 3s, 3p, and 3d states of excitation resulting from the impact of 75 to 350 kilovolt protons with various gaseous targets such as hydrogen, nitrogen, argon, and helium. In addition, a number of more complicated molecular targets such as methane, ethane, propane, carbon dioxide, carbon monoxide, and nitric oxide were used to produce 3s state excitation with the objective of establishing simple empirical rules for predicting molecular cross sections in terms of the cross sections for the constituent atoms.

In the present investigation, considerable effort has been directed toward providing a vivid understanding of many of the associated processes affecting the formation and decay of excited projectiles. These processes include, among others, the perturbation by static and motionally induced electric fields, the collisional excitation of neutrals, and the collisional destruction of excited states.

Finally, a study of the formation of excited hydrogen by the dissociation of H_2^+ and H_3^+ projectiles has been made.

A collimated beam of protons was allowed to traverse a differentially pumped target cell. The Balmer alpha radiation from the emerging beam displayed a distinctive spatial profile, variation of emission intensity with distance, which was determined by the relative production of 3s, 3p, and 3d state excitation, and each state's characteristic

lifetime. From this profile the relevant cross sections were inferred via a mathematical deconvolution procedure. The quantitative determination of the emission profile was obtained by a large number of simultaneous measurements of target density, projectile flux, and photon emission as a function of the distance from the target cell exit aperture.

The relative production of the 3s, 3p, and 3d states of excitation was found to be non-statistical; further, it was found that production of lower angular momentum states is preferred. The ratios of the cross sections for producing 3s, 3p, and 3d states by charge transfer are in disagreement with existing theory for the neutralization of protons by helium.

No simple rules were found for predicting the production of 3s hydrogen by the charge transfer neutralization of protons by complicated molecular targets.

The dissociation of H_2^+ and H_3^+ was found to produce an abundance of 3p and 3d state hydrogen; this contrasted strongly with the production of hydrogen by charge transfer.

CHAPTER I

INTRODUCTION

The study of atomic collisions has become one of the most productive fields of modern physics. With the application of quantum theory, a great deal has been learned about the structure and interaction of atomic systems. The impact of this knowledge upon technology has been considerable.

In atomic collision physics, we can usually focus our attention upon the interaction of two atomic systems. Generally, these systems are complicated structures containing many subatomic particles. Since the interaction of these particles is governed by the well understood electromagnetic force, the interaction of the conglomerate systems is understood in a basic sense; however, because there are many interacting particles, an exact mathematical analysis is seldom if ever possible. The problem of formulating a tractable theoretical description of atomic interactions is one of choosing the best set of simplifying assumptions. The ultimate success of the resultant theory is determined in the light of experimental observation. With modern techniques, a number of atomic processes have become amenable to experimental investigation. Over the past two decades, there has been an enormous expansion of experimental data.

Within the framework of atomic collision physics, a large number of interesting processes fall into a general category described as rearrangement collisions. In such collisions, the interacting systems

undergo a definite change in structure. The rearrangement of atomic structures requires a change in total system energy; hence, rearrangement processes are included in the general classification of inelastic processes--processes in which the total kinetic energy of the initial systems is not conserved.

One of the most interesting rearrangement processes is the collisional production of atomic hydrogen from the impact of simple ionic projectiles. This can occur in two ways--by dissociation and charge transfer. In dissociation, the projectile undergoes collisional fragmentation with the resultant production of hydrogen; in the case of charge transfer, an incident H^+ or H^- ion exchanges an electron with the target system to produce a neutral hydrogen atom. As a subset of these types of rearrangement processes, it is often possible to discuss only collisions which produce hydrogen in a particular state of excitation. In a field free region, such states can be characterized by the standard representation with quantum numbers n, ℓ, j and m_j. The collision process is then described in terms of the cross section for producing the particular quantum state. In the next chapter, we shall give an exact definition of this quantity.

In this study, the production of 3s, 3p, and 3d state hydrogen was investigated for the charge transfer neutralization of protons and the collisional dissociation of H_2^+ and H_3^+ ions:

$$H^+ + X \rightarrow H^* + [X^+] \qquad (1)$$

$$H_2^+ + X \rightarrow H^* + [H^+ + X] \qquad (2)$$

$$H_3^+ + X \rightarrow H^* + [H_2^+ + X] \qquad (3)$$

No information was available for the state of ionization, excitation, or molecular association for the reaction components in the square brackets.

Only the n and ℓ character of states was resolved; detailed information about j, m_j, or, alternatively, s, m_ℓ, and m_s could not be obtained. For charge transfer, targets of nitrogen, argon, hydrogen, and helium were used to produce 3s, 3p, and 3d hydrogen for incident proton energies from 75 to 350 keV. The production of 3s hydrogen was studied for energies up to 600 keV for targets of nitrogen and helium. Certain more complicated molecular targets have been employed to produce 3s hydrogen at 75, 150, and 250 keV with the objective of establishing rules for predicting the behavior of molecular targets in terms of their atomic constituents. The production of 3s, 3p, and 3d hydrogen by the collisional dissociation of H_2^+ and H_3^+ projectiles has also been investigated. For the sake of economy, the work concerning dissociation is discussed in an appendix; the experimental techniques involved are essentially the same as those for charge transfer. The main thrust of this thesis will be a discussion of the charge transfer process.

Unlike ionization and dissociation, charge transfer is, in general, a much more likely process at lower interaction energies. It is this generic feature which is, in large measure, responsible for the fact that most charge transfer studies have been conducted in the low energy region (less than 100 keV). Furthermore, high energy studies require more complex experimental facilities. In low energy work, for example, the

accelerator system providing the incident ions is typically a rather minor appendage to the experimental apparatus; for high energy experiments, however, the accelerator system is usually a large and expensive affair--which is often of complexity rivaling that of the actual experimental apparatus.

Studies of the formation of the 3s, 3p, and 3d states at low energies are fairly complete. Hughes[1,2] has acquired extensive data for such targets as He, Ne, A, H_2 and O_2 below 120 keV. Andreev[3,4] has studied He, Ne, A, and H_2 targets below 35 keV. The observation of Lyman beta radiation has given some separate information about the formation of the 3p state (Andreev,[3,5] DeHeer,[6] and Sheridan[7]).

Measurements of charge transfer into the 3ℓ states at energies beyond 120 keV have heretofore been limited to the work of Edwards and Thomas[8]. In this study the charge transfer formation and collisional destruction of 3ℓ hydrogen was investigated for targets of N_2 and He between 75 and 400 keV.

Despite the fact that the high energy region is relatively unexplored, it is an area from which a great deal can be learned. This is quite clear from the fact that at the present time no theory is capable of describing the charge transfer formation of hydrogen in the 3s, 3p, and 3d states of excitation--even the relatively simple case of protons onto helium.

From a theorist's point of view, the ideal experiment is the impact of protons with atomic hydrogen:

$$H^+ + H \rightarrow H^* + H^+ \qquad (4)$$

Here, exact wave functions are known and a very rigorous treatment is possible. This is, experimentally, a very difficult reaction to study; atomic hydrogen exists in a non-tenuous gas phase only at a very high temperature. It is possible to construct a moderately high temperature tungsten target cell which can catalytically dissociate molecular hydrogen. The walls of such a cell would have to be maintained at a temperature of over 2000°C. One could envision a multitude of problems: the copious production of electrons within the cell, a tremendous production of Balmer alpha radiation from incandescence which would have to be baffled from the observation region, the determination of target density within the cell, etc. The simplest atomic system most readily employed as a target is obviously helium. For this reason, a few theoretical treatments have been attempted for the reaction:

$$H^+ + He \rightarrow H^* + He^+ \qquad (5)$$

Mapleton[9] has made calculations using a Born approximation technique, which predicts an energy dependence for the production of 3s state hydrogen projectiles, the shape of which is in good agreement with our measurements; further, there appears to be only slight absolute disagreement. This simple Born approximation does not agree with our measurements of the 3p cross section. It has been suggested that calculations involving more coupling to more electron final states would yield lower p to s cross section ratios, and this would be in better agreement with our results. Sin Fai Lam[10] has attempted such calculations using an impact parameter formalism for the n = 2 state. Employing a general rule developed by Oppenheimer[11] which states that the charge exchange

cross section should show a n^{-3} dependence upon principle quantum number, Sin Fai Lam's calculations can be scaled to the n = 3 state. The ratio of the 3p and 3s cross section is then, indeed, in closer agreement with our measurements. Unfortunately, the form of the 3s cross section energy dependence is markedly different from that suggested by our measurements.

It should be pointed out that our data gives no information about the final state of the ionized target; our measurements are, therefore, representative of a sum over all final target states. This does not constitute a serious limitation in the comparison with theory. In fact, Mapleton includes several higher final target states in his calculations. While his treatment is not exact, it does give a reliable indication of the very rapid convergence of the sum over final target states. For example, he shows that nearly 90 percent of all charge transfer processes leave the target in the ground state.

Although measurements of charge transfer from helium targets at high proton energies have not succeeded in bestowing a particular preference upon any of the current theoretical treatments, they have, nevertheless, been extremely fruitful. It has become clear that the asymptotic region for the Born approximation lies within our energy range of 75 to 400 keV. Further, in pointing out the strength and weakness of any given theory, these measurements serve as a valuable guide in the formulation of a high energy theory. Such a theory is a necessity in the overall understanding of the charge transfer process--even in the low energy domain.

Finally, the study of helium targets may have a great potential for the development of three body theory. Faddeev[12,13] has, in recent

years, developed a powerful three body formalism. Faddeev theory generally entails a prohibitive amount of numerical computation (with the present generation of computer systems), but may well prove tractable in a number of specific cases. Thus far, it has been employed almost exclusively in the area of particle physics. It may be that its immediate application to this area is premature; the difficulty in solving problems in particle physics is compounded not only by a lack of experience with this formalism but also by the very obvious fact that the fundamental dynamics of the interactions involved are not understood. A more didactic approach may be to first attempt a solution of the atomic interaction of protons with helium where the fundamental dynamics (electromagnetic interactions) are known and a wide selection of empirical information is available. The experience gained in such an undertaking may then be of considerable use to particle physicists.

Thus far, we have considered only the interaction of this work with theory. Measurements of charge transfer are of considerable application in other areas of experimental physics. Practically all experiments dealing with the interaction of neutral beams with matter require some knowledge of how the incident neutrals are prepared. It should be pointed out that the study of lower states (n = 2,3,4) may well be the only way to predict the probable distributions of angular momentum states at higher n. Since these states become progressively more degenerate with increasing n, they are correspondingly more vulnerable to Stark mixing. (The critical field--the field that completely mixes the nearly degenerate ℓ states--decreases as n^{-5}.) It is not likely that one could guarantee sufficiently field free conditions to make any meaningful direct

measurement of the collisional population of angular momentum states at n greater than 4 or 5.

Charge transfer processes are of considerable interest in the study of auroral emissions in the upper atmosphere. Solar protons incident upon the earth are often quite energetic. They are slowed in their penetration of the atmosphere by a continuous process of neutralization, ionization, and reneutralization. Protons with energies greater than 100 keV are prevalent at altitudes beyond about 100 kilometers. Doppler shifted H alpha radiation has been observed in auroral displays in this region. The majority of this radiation may be due to the population of $n = 3$ state by collisional excitation. Doubtlessly, some emission is due to direct electron capture into this state. A knowledge of capture cross sections is also of further importance in assessing the overall production of neutrals and the probability for their subsequent excitation. Some polar aurora occur at altitudes of only 60 kilometers. In this region the atmosphere is sufficiently dense to collisionally quench 3ℓ hydrogen atoms. The understanding of these aurora requires a knowledge of the processes of the collisional destruction of excited states.[14]

It might be appropriate to mention here that the study of upper atmospheric atomic collisions has expanded rapidly over the last decade. A great deal of this work has found application in communications, pollution, and space exploration. Much of the stimulation for the research has come about from relatively recent discoveries of the enormous complexity of the structure of the upper atmosphere. A great deal of research into atmospheric excitation, ionization, and blackout phenomena has been prompted by the study of the effect of nuclear detonations on suborbital

weapons systems. With the continual increase in the capability to explore the upper atmosphere, there is every reason to expect a corresponding increase in the effort to understand the physics of atomic collision processes.

The primary impetus for this research has always been derived from the controlled thermonuclear fusion division of the U. S. Atomic Energy Commission. There are few scientific endeavors which can claim a comparable prospect for the acceleration of human development than that held by the harnessing of thermonuclear power. Indeed, our major concern for the future may be the survival of our present level of civilization. There is every reason to believe that the beginning of the twenty-first century will represent the most critical period in the history of the development of mankind; it is in this period the full weight of the problems of population, pollution, and the depletion of natural resources will come to bear simultaneously. It is a well established fact that all of these problems often develop at an exponential rate; their onslaught can be expected to be frighteningly swift. The resulting upheavals in the social order brought on by insufficient food and resources are likely to be catastrophic. It is absolutely essential that new sources of energy be developed.

Vast amounts of energy will be required to expand food production and conserve our material resources. In contrast to the future, present power shortages are relatively minor and can be easily handled by the expansion of existing fission and fossil fuel power systems; the realization of this fact must not, howerver, result in a myopic approach to the planning of new power system technologies. The very magnitude of

projected power requirements suggests the long lead time which will be required for their development. By the year 2000 A.D., the world's power requirements are projected to be 30 million megawatts.[15] Only a small fraction, about 10 percent, can be obtained from the expected revolutions in hydroelectric, tidal, and geothermal power.[15] The remainder will have to be produced by a continuing depletion of our reserves of chemical and fissionable fuels. While recent developments in breeder reactors will slow the consumption of fission fuels, they do not represent a long term solution. Furthermore, there is much objection to their development on the basis of their inherent danger due to contamination and the proliferation of nuclear explosives among the underdeveloped countries. The continued use of combustible fuels, on the other hand, may pose the most immediate danger due to pollution.

The development of thermonuclear fusion will provide a virtually limitless source of energy; marine reserves of DHO alone constitute 8 billion times the estimated energy requirement of the year 2000.[15] The only by-product from the fusion of this deuterium is helium; this poses no pollution threat--in fact, natural helium reserves are rapidly becoming extinct. Thermal pollution may be virtually eliminated by fusion reactors. Present-day thermal power systems are inherently thermodynamically inefficient because they draw energy from relatively low temperature heat sources. Fission or chemically fired systems are limited in their ultimate operating temperature by the materials used in their heat source confinement or heat exchange systems. This is not necessarily the case with fusion machines. It may be possible to draw power directly from the fusion plasma. There are a number of direct conversion systems

currently under investigation: inductive mangetoplasma-dynamic, electro gas dynamic, and plasma expansion converters. Certainly, it would be a great waste to employ a 50-million °C plasma to drive a steam turbine operating a mere 2000°C.

The enormous amounts of energy available from a fusion system would, in addition to stimulating new industries, make a number of conservation and reclamation projects possible. For example, fusion plasma systems have a unique capability for the bulk heating of matter. The regulated injection of high Z atoms into the plasma can produce intense UV or X radiation (perhaps megawatts/m^2). Since the plasma is very transparent to such wavelengths, most of the radiation escapes and can be used for heating. This heating method is ideally suited to desalination. In fact, these intense sources of UV have been suggested for use in the treatment of raw sewage. Solids injected into fusion plasmas undergo shock vaporization rather than the more familiar ablatively cooled deflagration due to the tremendous energy content and thermal conductivity of the plasma. For this reason, the concept of a fusion torch has been suggested as a method for reconstituting waste materials.[15] Waste compounds injected into a fusion disintegrator would be reduced to their elemental constituents. These elements could be separated and recondensed providing a cheap source of purified materials. This would be a great step toward attaining a closed cycle economy.

The study of charge transfer processes is important in a number of areas of research concerned with the design of a thermonuclear power system. The injection of high velocity neutrals is considered to be an important scheme for heating confined plasmas. Neutrals can penetrate

the plasma containment field; upon entry they can undergo either Lorentz or collisional ionization and thus become trapped. Their incident kinetic energy is then collisionally distributed with a resultant increase in plasma temperature. Neutrals prepared in highly excited states are more subject to Lorentz ionization; for typical containment fields, hydrogenic neutrals would undergo Lorentz ionization in states with principal quantum number 8 or greater. Collisional ionization would, however, be appreciable for states as low as n = 3. It appears that highly excited neutrals are not readily produced regardless of the neutralization process. It therefore appears that collisional ionization is the principal mechanism for the trapping of neutrals. Measurements of collisional destruction (see Appendix I) suggest that collisional ionization is about a factor of two more likely for the n = 3 state than for the ground state. Consequently, the neutralization of the n = 3 state is a very important process in the trapping of particles in a plasma.

Energy can be transferred to plasmas by the technique of ohmic heating (an example of which is microwave absorption). This method has not found as wide an application as neutral injection. Much emphasis has, therefore, continued to be placed upon the study of the charge transfer neutralization process. Originally, very high energy injector systems were proposed (in the 500 keV range). Now, injection at energies below 50 keV is considered more practical--at least for the present generation of prototype machines. High energy studies can still, however, be considered a vital part of the overall effort in this area.

It is expected that the Ormak II (an American version of the

Russian Tokomak machine) will be equipped with neutral injectors to provide a great flexibility of operation. It would seem that some investigation of the methods for producing the optimum excited content in beams neutrailized by gases would now be most appropriate. A practical neutralizer would certainly not be limited to the use of such simple gases as N_2, Ar, He and H_2. Hopefully, the investigations of complicated targets will be of some use in selecting optimum neutralizer systems.

In addition to plasma heating, charge transfer processes are responsible for energy loss. Neutrals formed in a confined plasma can escape the containment field. In doing so, they transport kinetic energy out and hence lower the plasma temperature.

Finally, it is conceivable that charge transfer processes can be used in plasma diagnostics through the use of probe beams to delineate plasma density profiles.

CHAPTER II

EXPERIMENTAL TECHNIQUE

The basic objective of this work was the measurement of the production of hydrogen in the n = 3 state of excitation by the processes mentioned in the previous chapter. Further, the relative distribution among the fine structure (ℓ angular momentum) substates was desired.

Experimental Methods For Measuring The Formation Of Excited Hydrogen

Before proceeding with the discussion of methods for measuring the formation of excited hydrogen, we need to introduce the concept of cross section. From the definition of this quantity, the mathematical formalism required to interpret the production of the nℓ quantum states in terms of the radiation resulting from their subsequent decay can be developed.

Definition of Cross Section

Quantitatively, the production of these states can be characterized by the cross section for formation of the particular state in question. In a quantum mechanical sense, this quantity describes the probability for the transition between the initial state of a projectile and target to a final state containing an excited nℓ hydrogen atom. If the cross section specifies a particular momentum, energy, etc., for the final hydrogen atom, it can be regarded as a differential cross section. Within this context, the cross sections discussed here are total cross sections

summed over all possible translational states for the final particles. Furthermore, these cross sections will include, implicitly, all possible final states for the target.

An exact mathematical definition for the cross section for producing an $n\ell$ state hydrogen atom can be formulated in terms of a uniform beam of ionic projectile particles of current density, J^+, traversing a target gas with number density ρ. The cross section, $Q_{n\ell}$, can be defined in terms of the number of collisional events per second producing an $n\ell$ hydrogen atom within a volume element, dV, about the point X on the beam axis. This quantity will be noted by the symbol, $d^3N'_{n\ell}(X)$:

$$d^3N'_{n\ell}(X) = Q_{n\ell}\, J^+(XYZ)\rho(XYZ)\, dX\, dY\, dZ \tag{6}$$

Physically, this equation describes the conversion of ion current to an excited neutral current, $J^{n\ell}$. The cross section $Q_{n\ell}$, is an invariant fundamental quantity which, hypothetically, could be calculated if the dynamics of the collision process were known.

It is convenient to integrate Equation 6 over the cross sectional beam area to obtain the quantity, $d'N_{n\ell}(X)$--the number of $n\ell$ atoms formed in the interval dX about X; the current density is now replaced by the total projectile flux, $F^+(X)$.

$$dN'_{n\ell}(X) = Q_{n\ell}\, F^+(X)\rho(X)\, dX \tag{7}$$

Dividing by dX, we obtain $N'_{n\ell}(X)$--the rate at which $n\ell$ atoms are produced at X per unit length of beam.

$$N'_{n\ell}(X) = Q_{n\ell}\, F^+(X)\rho(X) \tag{8}$$

$N'_{n\ell}(X)$ is the time derivative of the population per unit length of $n\ell$ atoms in the beam; the population of excited states is related to the excited state current, $F^{n\ell}(X)$, by the relation:

$$F^{n\ell}(X) = N_{n\ell}(X)\ V \tag{9}$$

Here, V is the mean velocity of the $n\ell$ atoms.

Ultimately, $Q_{n\ell}$ will be inferred from the emission of radiation from the beam which results from the decay of the 3ℓ states. The assumption which must be made is that the population of the 3ℓ state is completely described by Equation 8. Actually, there may be other processes for populating the $n\ell$ states; hence, terms containing additional cross sections may need to be included in Equation 8. If we ignore this possibility, $Q_{n\ell}$ represents only an atomic line cross section describing all collisional events which result in radiation characteristic of the decay of $n\ell$ states.

Measurement of Cross Section

If a high velocity monoenergetic projectile beam is allowed to traverse a gaseous target, the excited hydrogen produced by collisions with the target particles will remain in a well defined beam by virtue of only slight angular scattering. These hydrogen atoms will continue down the beamline with approximately the same velocity as the incident projectiles; and, under single collision condition, they will eventually undergo natural spontaneous decay with the resultant emission of radiation. From the intensity and spatial profile of this radiation, one can determine $Q_{n\ell}$.

Unfortunately, the Balmer alpha radiation from the fine structure

levels cannot be separated spectroscopically. Special techniques are required to distinguish between light from the decay of the 3s and 3d states.

In general, excited projectiles can be detected by measuring the radiation resulting from their decay. It is often necessary to induce transitions by subjecting the projectiles to perturbing fields. Sufficiently large fields will produce Lorentz ionization; this constitutes still another detection method.

The formation of the 3ℓ states by charge transfer has been studied by observing the emission resulting from their decay. Both field free and perturbing field methods have found application; we shall now discuss these techniques. In this study, a field-free time-of-flight method was employed.

Stark Effect Method. Andreev, Ankudinov, and Bobashev[3,4] developed a technique for resolving the three $Q_{n\ell}$ cross sections by observing the effect of electric fields on the decay of the n = 3 state. This technique evolved from studies of Lyman alpha radiation produced by charge transfer. Since the 2s state of hydrogen is metastable, the production of this state cannot be studied without applying fields to induce transitions to the ground state.

Their method can be described as follows. A proton beam is allowed to impinge upon a gaseous target. Radiation is sampled from a region about a fixed point on the beam axis. Since a large percentage of 3p decays directly to the ground state, the 3p cross section can be determined by observing the intensity of Lyman beta radiation. This further determines the 3p contribution to the Balmer alpha radiation. The remaining Hα (Balmer alpha) radiation, due to 3s + 3d, is determined by

direct measurement with a photomultiplier detector. By imposing a strong electric field (600 volts/cm.) in the collision region, the n = 3 levels $(n\ell,j,m_j)$ are transformed into Stark perturbed levels characterized by n and m_j and the parabolic quantum numbers, n_1 and n_2. The parabolic quantized states can be written in terms of the initial unperturbed $n\ell$ states; further, their decay results in radiation very near the H_α and L_β wavelengths. Experimentally, four line cross sections can be measured: $Q(H_\alpha)$ and $Q(L_\beta)$ with and without a perturbing field. They determine explicitly the three $Q_{n\ell}$ cross sections.

This method assumes that the application of the perturbing fields does not affect the collision process. The nascent hydrogen is in a free field state which then continuously evolves into the parabolic state via the Stark perturbation before the state undergoes natural decay. As a justification for this assumption, Andreev[17] points out that the time required for the collisional formation of the state is on the order of 10^{-16} seconds. The time required to evolve into a parabolic state is approximately equal to the inverse of the frequency shift produced by the perturbing field; this is of order 10^{-10} seconds. The lifetime for the n = 3 state, by contrast, is of order 10^{-8} seconds.

Time-of-flight Method. The method just described is particularly appropriate to low energy processes yielding excited atoms which decay in a very short distance. At higher energies, the increased velocity of the excited atoms permits a time-of-flight analysis. This method was pioneered by Hughes[1,2] at energies below 130 keV. It requires the quantitative measurement of the Balmer alpha radiation from the beam. This radiation is described by an intensity function, I(X), where X is

the distance from the termination of the target cell; this function is defined as the total number of Balmer alpha photons radiated per second from a differential segment of beam dX about the point X. Since each state of excitation (3s, 3p, and 3d) has a distinctly different lifetime, the total intensity function, I(X), will be the sum of three spatially distinct and separable intensity functions--$I_{3s}(X)$, $I_{3p}(X)$, and $I_{3d}(X)$.

From each function, $I_{3\ell}(X)$, the corresponding cross section, $Q_{3\ell}$, can be determined. $I_{3\ell}(X)$ can be calculated from the population of 3ℓ atoms in the beam at point X:

$$I_{3\ell}(X) = A(3\ell \rightarrow n = 2)\ N_{3\ell}(X) \tag{10}$$

$A(3\ell \rightarrow n = 2)$ is the probability for spontaneous transition from the 3ℓ state to the n = 2 level.

There are two simple experimental configurations which can be employed to make such measurements of the intensity functions. One may observe the radiation from the excited hydrogen atoms as a function of the distance through the target region[8] or, as in the present configuration, one may observe the radiating atoms beyond the target region. In the latter case, the gaseous target is confined in a differentially pumped gas cell of known length; the observations are made beyond the cell in a highly evacuated chamber. The radiation intensity one observes as a function of distance down the beam is quite different in the two configurations.

In the "first configuration", the population of 3ℓ state is always governed by the equation:

$$N'_{3\ell}(X) = Q_{3\ell}F^{+}\rho - N_{3\ell}(X)A(3\ell) \tag{11}$$

The term, $- N_{3\ell}(X)A(3\ell)$, represents the loss of 3ℓ state population by natural decay; thus, $A(3\ell)$ is total probability for decay. Ideally, F^{+} and ρ can be treated as independent of X. By introducing the beam velocity, this equation can be written in terms of position only:

$$\frac{dN_{3\ell}(X)}{dX} = \frac{Q_{3\ell}F^{+}\rho}{V} - \frac{N_{3\ell}(X)A(3\ell)}{V} \tag{12}$$

Equation 12 has the following solution:

$$N_{3\ell}(X) = F^{+}\rho\, Q_{3\ell}\, {}_{3\ell}(1 - e^{-\frac{X}{v\tau_{3\ell}}}) \tag{13}$$

Here, $\tau_{3\ell}$ is the lifetime of the 3ℓ state which is simply the reciprocal of $A(3\ell)$.. Substituting $N_{3\ell}(X)$ into Equation 10, we obtain the intensity function for the 3ℓ state.

$$I_{3\ell}(X) = \frac{A(3\ell \rightarrow n = 2)}{A(3\ell)} F^{+} \rho\, Q_{3\ell} 1 - (e^{-\frac{X}{v\tau_{3\ell}}}) \tag{14}$$

The factor, $A(3\ell \rightarrow n = 2)/A(3\ell)$ is the branching ratio for the decay of the 3ℓ state. For 3s and 3d, this ratio is unity since they decay exclusively to the 2p level. For the 3p state, however, the ratio is 0.118 since 88.2 percent of the 3p decays directly to the ground state emitting unobserved ultraviolet (Lyman beta) radiation.

The total intensity is the sum over the three angular momentum states. Each intensity approaches an asymptotic maximum depending upon the cross section, target density, and projectile flux. The rate of increase of the intensity ($dI(X)/dX$) depends upon the product of the atom

velocity and lifetime of the 3ℓ state. This product is defined as the decay length, $X_{3\ell}$.

In the "second experimental configuration," I(X) is observed beyond the target region; here, the X dependence of the population of the 3ℓ state in the beam is governed solely by natural radiative decay:

$$\frac{dN_{n\ell}(X)}{dX} = \frac{- N_{n\ell}(X)A(3\ell)}{V} \tag{15}$$

The solution to this equation is a simple exponential:

$$N_{3\ell}(X) = N_{3\ell}(X = 0)e^{-X/X_{3\ell}} \tag{16}$$

Again, $I_{3\ell}(X)$ is determined by Equation 10. The total intensity is the sum over the three ℓ states:

$$I(X) = C_{3s}\, e^{-\frac{X}{X_{3s}}} + C_{3p}\, e^{-\frac{X}{X_{3p}}} + C_{3d}\, e^{-\frac{X}{X_{3d}}} \tag{17}$$

The population factors, C_{3s}, C_{3p}, and C_{3d}, can be obtained directly from Equation 13 by substituting the cell length, L, for X.

$$C_{3\ell} = \frac{A(3\ell \rightarrow n = 2)}{A(3\ell)}\, F^{+}\, \rho\, Q_{3\ell}\left(1 - e^{-\frac{X}{X_{3\ell}}}\right) \tag{18}$$

Hence, in the target cell experiment which employs the second experimental configuration one simply observes three separate exponentially decaying intensities. Again, the rate of change of the intensity is dependent upon decay length. In this case, however, the maximum value of the intensity (occurring at the termination of the target cell) is dependent not only upon the various cross sections but also the decay

lengths and extent of the target cell.

This feature introduces an additional source of error since one must know the length of the cell and distance from the termination of the cell to the point of observation. The determination of these quantities is complicated by the flow of target gas out of the cell. This not only changes the "effective" length of the cell but also obscures its termination. As explained later, in the range of cell geometries available in the present experiment, this problem is not too serious.

The most important aspect of this feature of the second experimental configuration is that it provides an experimental method for contrasting the three different intensities. For example, in a very long cell, each initial intensity would reach its maximum value and then depend solely upon cross section for a given target density and projectile flux. As it turns out, in the case of charge transfer, the 3p and 3d cross sections are somewhat smaller than that for the 3s. In addition, the intensity of radiation from the 3p state is further reduced by the branching ratio. Hence, for a very long cell, it is most likely that the p and d contributions would be obscured by that of the s state. For short cells, the states with shorter lifetimes (p and d) are able to more nearly attain their asymptotic maximums. Their contributions to the total intensity are, therefore, enhanced and made more identifiable. Furthermore, the ability to weight the various contributions to the total intensity by a known amount does, in itself, constitute a partial experimental test of the overall measurement.

While observations in the target region, using the first experimental configuration, yield generally larger photon intensities, the

structure in the intensity function due to the p and d contributions exists only at the small distances of penetration into the target where the intensity is at a minimum. This is not quite as serious as it may seem since the s state contribution is well determined from data extrapolated from larger distances. At any rate, the situation is reversed in the gas cell configuration and clearly this configuration has an additional measure of resolving power.

In addition to the problems discussed thus far, observations in the target region compound all the non-linear effects associated with multiple collisions and beam neutralization. Basically, there are two distinct aspects to this complication. Since effects such as beam neutralization and the collisional destruction of excited atoms are dependent upon the product of target density and penetration distance and because a large number of the observations must be made at distances larger than the gas cell length (to accurately determine $I_{3s}(X)$) these effects are naturally larger in magnitude. Worse still, these effects are a function of distance and tend to complicate the intensity function.

The process of resolving cross sections requires essentially a Fourier decomposition of the intensity function into simple exponential terms. Complications in the intensity function make such a deconvolution more ambiguous and lessen the statistical significance of any one term despite the fact that the theoretical form of complication may be well known. To summarize, in the gas cell configuration, these effects are smaller and--more importantly--not a function of the point of observation.

The target cell configuration provides the only practical method for the investigation of charge transfer cross section of molecular

hydrogen. Highly energetic protons readily dissociate molecular hydrogen resulting in the production of a considerable number of stationary hydrogen atoms in the n = 3 state. The Balmer alpha emission from these atoms is considerably more intense than that from the high velocity atoms in the beam produced by charge transfer. Observations of charge transfer processes are, therefore, seriously obscured by target excitation when made in the target region. It is conceivable that one could distinguish the beam emission from that of the target by the beam's inherent Doppler shift. This would, however, require the use of very narrow band optical filters (or possibly monochromators); it is certainly not likely that one could obtain a sufficient overall transmission for the photon detection system.

Finally, observations of the decay in a high vacuum are more amenable to experimental test for Stark mixing of the p and d states. The intensity function for observation in the target region must contain a constant term resulting from target excitation. It appears that the introduction of test fields in the target region appreciably alters this term probably through the removal of excited charged targets from the observation region.

Experimental Apparatus

As was pointed out in the last section, the formation of the 3ℓ states (by charge transfer and dissocation) was studied by observing the emission due to their decay by the time-of-flight method. In this experiment, these observations were made in a high vacuum beyond the neutralization cell.

At this point, it is most appropriate to describe in some detail the apparatus which was used to make the measurements of the charge transfer (and dissociation) cross sections. Figures 1 and 2 show the main

body of the experimental apparatus.

Preparation of the Beam

The positive ions were provided by a vertically mounted Van de Graaff accelerator (High Voltage Engineering Model JN). The projectile ions were produced in an RF discharge source. The ion beam was rotated into the horizontal plane by the analyzer magnet. The analyzer Field (which determines the beam energy) was measured with a Harvey Wells nuclear magnetic resonance gaussmeter. From the magnet, the beam passed through two beam sensing slits used in the accelerator's energy stabilization system.

Beyond this point, the beam passed through an electromechanical beam shutter into a highly evacuated collimation chamber. The collimators consisted of two orifices mounted on three precision alignment rods. The position of the collimators and diameter of the orifices were so adjusted that no projectiles traversing the collimation system could strike either the entrance or exit orifice of the target cell (when the cell was evacuated).

The target cell was so constructed that its length could be varied if desired; however, once the optimum length was found (by compromising the photon signal strength, enhancement of the 3p and 3d emission, beam collimation, end effects of the cell on the target density profile etc.) it remained constant for all the following measurements. The exit orifice was equipped with an annular electrode to test the effectiveness of the beam collimation during the operation of the experiment when there was danger of scattering projectiles onto the exit orifice. From the target cell, the beam traversed a highly evacuated observation chamber and entered a standard Faraday cup provided with plates for the suppression of secondary electrons.

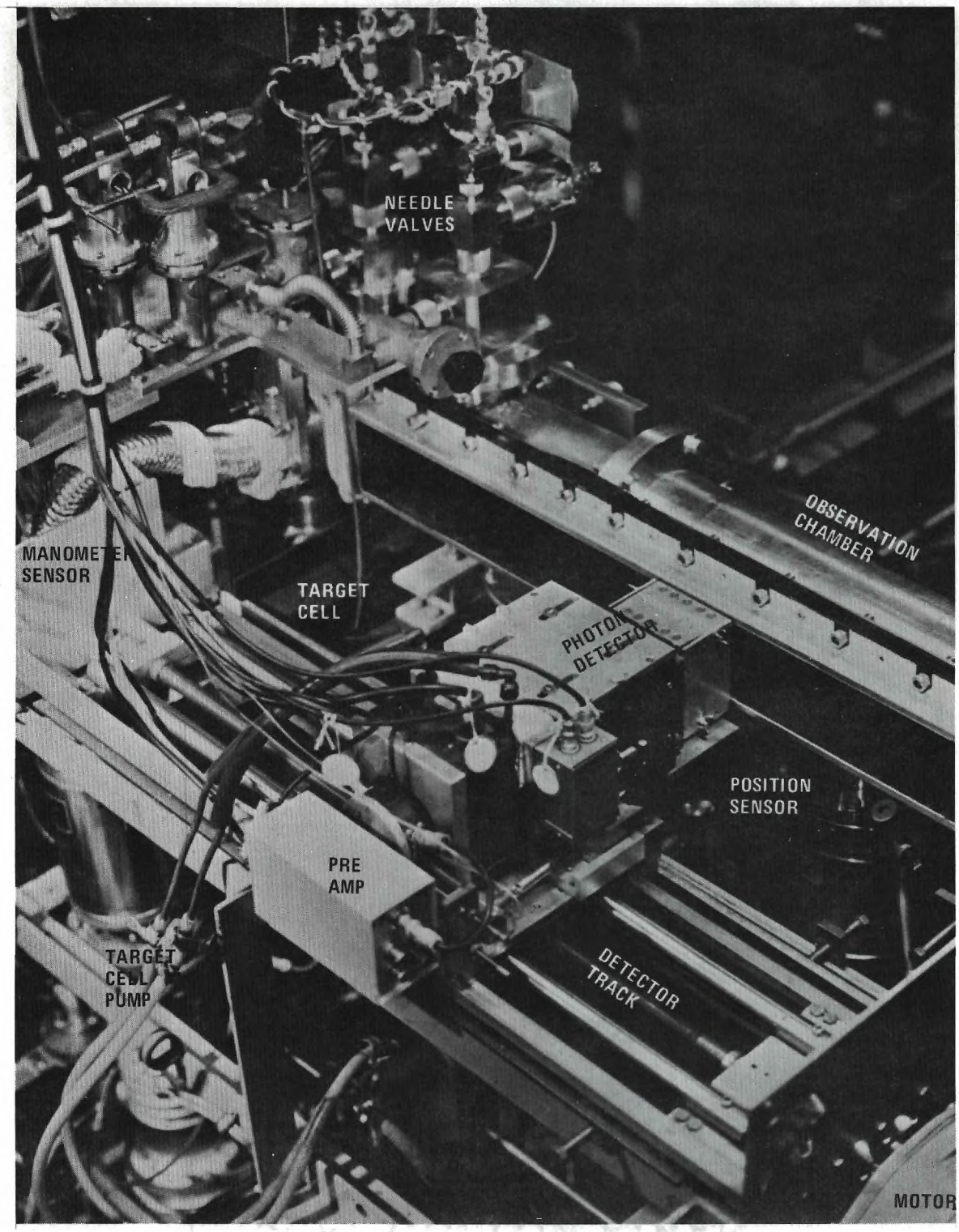

Figure 1. Photograph of the Apparatus.

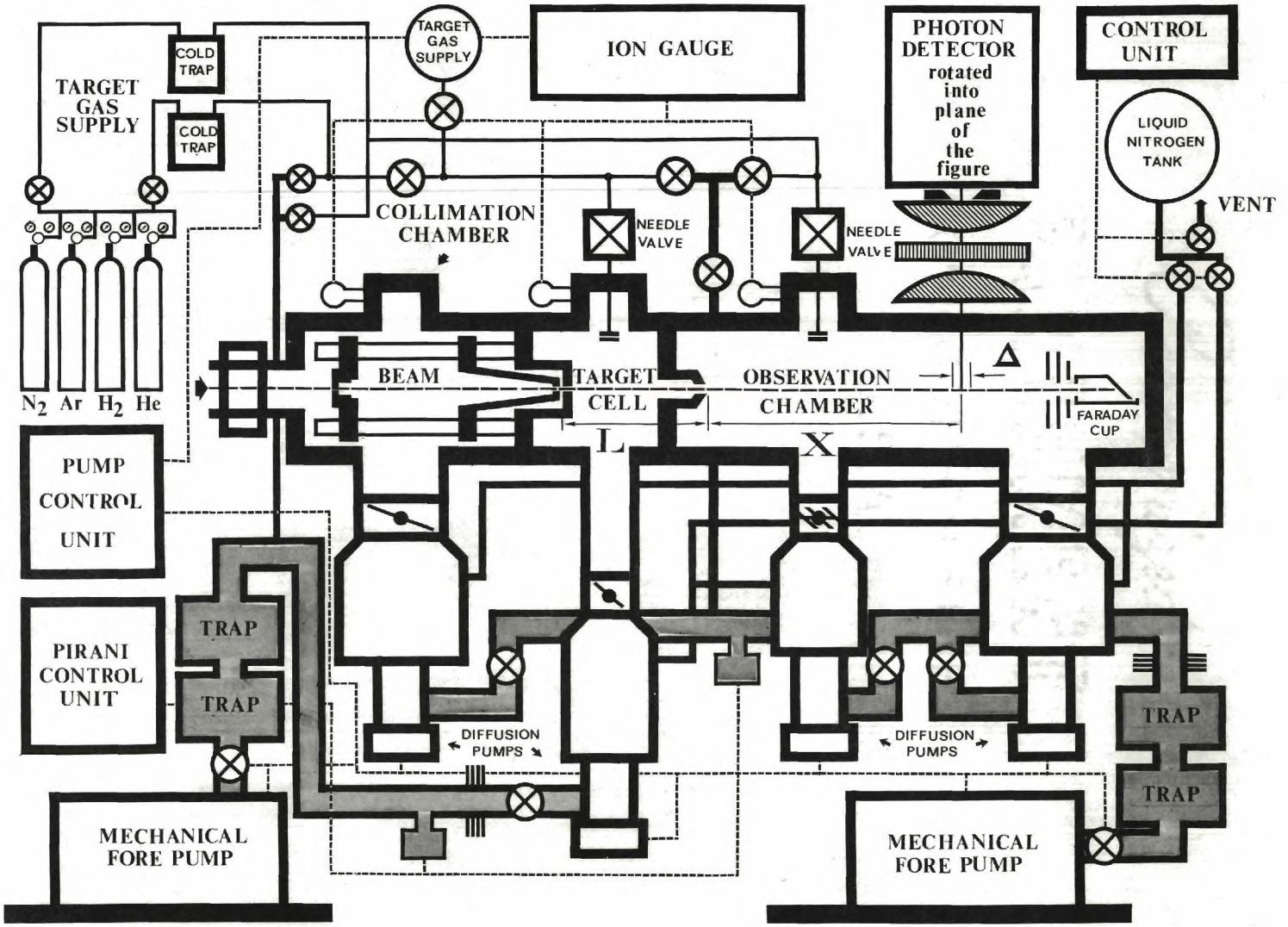

Figure 2. Diagram of Experimental Apparatus.

Vacuum System

In order to prevent the build-up of contamination gases, the target cell was continuously pumped by a liquid nitrogen trapped four-inch diffusion pump. The speed of this pump was reduced somewhat by its connecting manifold which was designed to reduce the possibility of a pumping gradient in the region of the beam line and to insure that the target gas was not cooled by the liquid nitrogen trap. The observation chamber was evacuated by one four-inch and one two-inch liquid nitrogen trapped diffusion pump. This pumping was necessary to provide a large differential pumping ratio between the target cell and the observation chamber.

The exit orifice of the target cell was also designed to enhance the pumping ratio; it consisted of a channel 0.125 inch in diameter by 0.250 inch in length. The pumping ratio depended upon the particular molecular weight of the target gas, but generally fell between 300 and 500 to 1. A large pumping ratio was necessary to minimize photon emission produced by the interaction of the beam with background gas (a mixture of residual gas and target gas from the gas cell).

The collimation chamber was also evacuated with a large four-inch pump to prevent any preneutralization of the beam. Pumping ratios between this chamber and the target cell were even higher since the target cell entrance orifice was smaller than the exit orifice. (Such an arrangement is possible because there is less beam divergence near the collimators.)

The diffusion pumps were coupled to their respective fore-pumping systems through both a low temperature and an alumina absorption trap. This precaution is taken to reduce the backstreaming of hydrocarbonous

oils from the mechanical forepumps. Such oils could conceivably crack in the diffusion pump boilers producing hydrogen contamination. Each diffusion pump was charged with Dow 705 silicone oil.

With no target gas present, the vacuum in the three chambers could generally be maintained below 2×10^{-7} torr. During operation with gas in the target cell, the observation chamber pressure generally feel in the 10^{-6} torr range.

As we shall point out shortly, the target pressure was measured using a capacitance manometer. The pressure transducer for the manometer, mounted on the outside of target cell, is itself extremely sensitive to mechanical vibration; hence, special care was taken in coupling the forepumps (oil filled rotatary vane type) to the rest of the apparatus. Each forepump was shock mounted on its own individual platform mechanically separate from the supporting frame for the apparatus. The forelines were coupled to the diffusion pumps via vibration absorbing metal bellows. Each forepump was equipped with a A.C. current operated isolation valve. Such valves often produce vibration themselves; therefore, they too were located on the independent platforms.

Injection of Target Gas

Target gas could be injected through two precision Edwards needle valves into either the target cell or observation chamber. A special gas feed manifold was constructed which allowed a rapid change over from one target gas to another. The manifold was equipped with low temperature traps and could be pumped down to a background pressure of only a few microns. Since the gas feed manifold was pressured to slightly over one atmosphere during operation, the purity of our gas samples was insured. (For this

experiment, only high purity - better than 99.9 percent - gases were purchased. The one exception, nitric oxide, was repurified by vacuum distillation.)

After being throttled through the needle valves the target gas entered the cell (or observation chamber) via a specially constructed injector. This injector was designed to disperse the gas in order to prevent the occurrance of a local pressure increase at a point anywhere along the beam axis. Further, the injector insured that the target gas was throughly accommodated to the target cell wall temperature before entering the collision region.

Photon Detection System

The observation chamber consisted of two smaller chambers, each fitted with a glass plate window through which the beam line could be viewed. The glass plate windows were made from a special glass with a very low absorption in the red end of the optical spectrum. They were located as far as possible from the beam to help avoid the possibility of accumulating a static electric charge.

The photon detector, consisting of a lens assembly, interference filter, aperture, and EMI 9558 photomultiplier, was mounted on a specially constructed traveling platform. The platform could be positioned automatically, and, once aligned with the beam, it would accurately maintain its orientation.

Figure 2 also shows the construction of the photon detection system. The lens assembly consisted of two plano convex lens which focused an image of the beam onto the aperture in front of the photomultiplier. An interference filter was placed between the lens so that all light rays from the

beam were normally incident on the surface of the filter; the filter was supported firmly to insure that this condition always prevailed.

The photomultiplier was operated in the pulse counting mode. The signals were analyzed by an RIDL amplifier discrimination system, which was adjusted to optimize the signal to noise ratio. The inter-dynode potential was maintained by a well stabilized high voltage power supply. The photomultiplier tube itself was mounted in a refrigerated box to reduce inherent noise and background signals. A small temperature probe was placed in contact with the tube to verify that it remained at a constant temperature during the course of an experiment. Measurements of the dependence of the photomultiplier background signal upon tube temperature were made for the particular pulse height discrimination used to analyze the photomultiplier output. Below -10° C, the background varied only slightly with tube temperature.

Measurement of Pressure

The target pressure was measured with an MKS capacitance manometer. The sensor of the manometer (pressure transducer) could be connected to either the target cell or observation chamber by the manipulation of two valves. The measured pressure and the zero reference pressure (provided by the collimation chamber) were connected to the sensor through two electropneumatic valves that could automatically return the sensor to a zero differential pressure mode. In this way, the zero drift of the electronics of the manometer was recorded as well as its overall sensitivity.

The manometer was calibrated against a standard liquid nitrogen trapped refrigerated McLeod gauge. The error introduced by the cold trap pumping effect was minimized by using hydrogen as a calibrator gas. In

addition, thermal transpiration was taken into account. The MKS manometer was found to be close in agreement with the McLoed gauge and very linear over the range of pressures used in this experiment.

The residual and background pressures in the various chambers of the apparatus were measured using standard Veeco ionization gauges. Foreline pressures were measured with Edwards Pirani Gauges.

Measurement of Beam Flux

The mean projectile flux entering the target cell was inferred from the charge accumulated in the Faraday cup during a measurement period. The Faraday cup was carefully constructed to minimize leakage currents. With no beam present, no leakage currents greater than 10^{-10} amperes were detected. Since typical beam currents were greater than 10^{-7} amperes, leakage currents introduced no error. Beam particles too divergent to enter the Faraday cup (the scattered current) were intercepted by an annular metal electrode.

The main beam current was measured with a Keithley Model 415 precision electrometer. This electrometer was calibrated against a Gyra mercury cell current source; it was found to be accurate to within two percent. The scattered current was continuously monitored with a Keithley 410 electrometer.

Data Acquisition

In this section, we shall discuss the procedure of acquiring and recording data from which the intensity function, I(X), is calculated. In addition, a brief discussion of the more significant systematic experimental errors encountered in the measurement of this data is given.

Data Recording System

In order to make measurements of high accuracy and to cope with the problem of small signal strengths, the basic procedure for acquiring data was automated. This automation greatly accelerated the rate at which data was taken while reducing human error. The speed at which the data is acquired was an important factor in this experiment. The basic measurement of all three charge transfer cross sections typically required an experimental running time of from 12 to 16 hours--even with an automated system. Over such a relatively long measurement time, drifts in the sensitivities of the various electronic instruments could become a significant problem. In addition, the automated data system allowed the operator to pay more attention to the running of the accelerator (which at times required a great deal of devotion) and also allowed him to oversee the overall performance of the experiment with greater comprehension.

The data was entered on four Ortec scalers which were periodically purged and recorded by an Ortec 432 controller and teletype system. The teletype output consisted of both a printed page and punched tape. The tape was converted into cards which were edited and then entered into the Burroughs 5500 computer for analysis.

The Ortec controller-teletype system was coupled to a master programmer that controlled the sequence of functions necessary to operate the experiment. This programmer generated the various data routines and operated a multiplexing system which provided the correct routing of signals that in turn interfaced the appropriate subcomponents (transducers, digitizers, counters, etc.) for each cyclic mode.

The master programmer also commanded a scanner programmer that

controlled the positioning of the photomultiplier. In addition, the master programmer was connected to the perturbation field programming system which could automatically vary the electric or magnetic field conditions in the observation region.

An account of the function of the perturbation field programmer unit is given in the section dealing with the Stark effect in the next chapter. Figure 3 is a block diagram of the basic data acquisition system; it gives some idea of relationship between the various subsystems and programmers.

In order to determine relative values for the 3ℓ charge transfer cross sections, we must determine I(X) as a function of X. This is done, experimentally, by making a set of measurements, $\{S_I(X), X_I\}$. Here, $S_I(X)$ is the number of photons detected at position X normalized to the mean prevailing target density and to the projectile current integrated over the time interval required to measure $S_I(X)$. The projectile current was inferred directly from the current entering the Faraday cup beyond the target cell; the target density was calculated from the measured target cell pressure and temperature, P_I and T_I. These measurements were made in the following manner:

1. The photon detector was moved automatically to a position X_I. All subsequent measurements at this position were indexed by the symbol, I, and constituted the I^{th} data point.

2. At this I^{th} position, a programmed sequence of measurements was then made. This sequence of measurement was composed of several "data acquisition cycles" each of which was indexed by the symbol, J.

There were four "modes" or measurement routines for each data

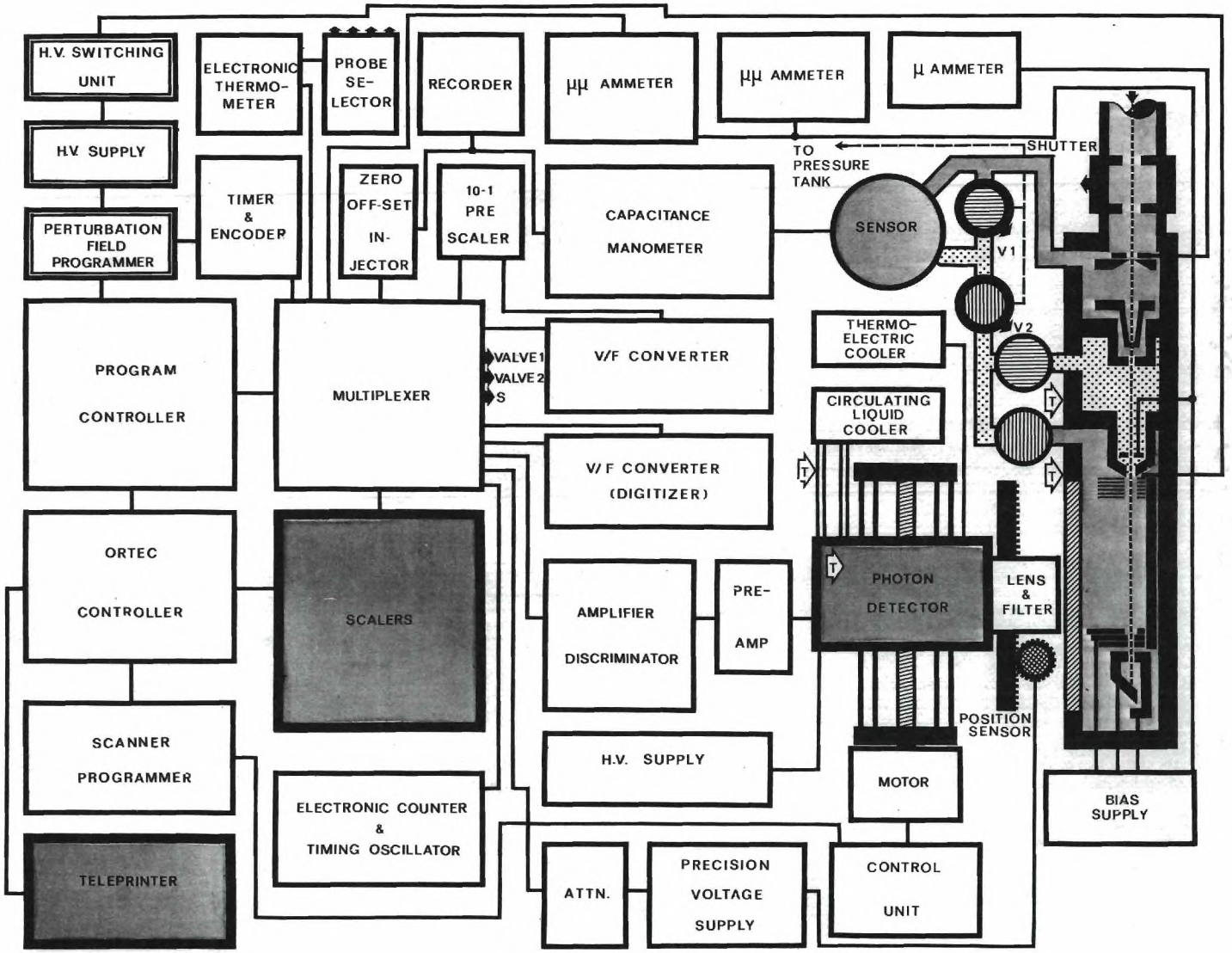

Figure 3. Schematic of Basic Electronic Systems.

acquisition cycle. Each data cycle was divided into two component "sub cycles".

Thus, we consider the basic data acquisition cycle as a two-step process. First, there was a ten second counting sub cycle followed by a sub cycle whose time duration depends upon the amount of integrated beam charge desired. The four modes for the data acquisition cycle were characterized by four modes for the first sub cycle: Mode 1 recorded the position of the photomultiplier, X, and a ten second count of the photomultiplier background, DC. Mode 2 recorded the zero drift of the electrometer, KZ, the background, DC, and the temperature of the target cell, T. Mode 3 recorded the current running time for the experiment, ENC, and the background, DC. The last mode, Mode 4, recorded KZ, DC, and the zero drift of the pressure measuring system, BZ. There was only one mode for the second subcycle: photon number, S, integrated pressure, P, integrated charge, I, and the counting time to acquire these parameters, CT. The format of the printed output of the teletype illustrates the sequence of measurements. This also represented roughly the format of the data input to the computer.

Data Point I:

DATA CYCLE

Mode	Subcycle 1				Subcycle 2			
1	X_{I1}	DC_{I1}	00	00	S_{I1}	P_{I1}	I_{I1}	CT_{I1}
2	KZ_{I1}	DC_{I2}	00	T_{I1}	S_{I2}	P_{I2}	I_{I2}	CT_{I2}
3	ENC_{I1}	DC_{I3}	00	00	S_{I3}	P_{I3}	I_{I3}	CT_{I3}
4	KZ_{I2}	DC_{I4}	00	BZ_{I1}	S_{I4}	P_{I4}	I_{I4}	CT_{I4}

Figure 4. Format and Sequence of Measurements Determining the Intensity, $I(X_I)$, at a Given Position, X_I.

Here again, I indexes the I^{th} measurement made at position X_{IJ}, for all values of J. 00 represents data relevant to the data control system and not used by the computer. Obviously, a complete set of J data acquisition cycles at any location X_{IJ} must contain some integral multiple, N(I), of four data cycles. After 4N(I) data cycles, therefore, the system was programmed to automatically move to a new position and take 4N(I+1) data cycles for the I + 1 data point. The distance moved between I data points could also be programmed; one could arrange, therefore, to take more data in regions where the intensity function displayed more structure.

Systematic Experimental Errors

Questions arising as to the validity of the measured cross sections can be separated into two categories. First, we must consider the accuracy with which one can determine the experimental parameters needed to evaluate the cross section; we shall discuss this problem in the present section. Secondly, we must decide how closely our models from which we infer the cross section represent reality. This consideration is discussed in detail in the next chapter.

Measurement of Radiation from the Beam. The photon measurement is subject to a number of errors and corrections. Since we were interested in Balmer alpha radiation, it was desirable to use a red sensitive photomultiplier. Such tubes are, in general, rather noisy even when cooled to -30°C. Typically, background signals of between 10 and 25 counts per second were encountered. Since the contribution of the background to the total signal must be subtracted, it was essential that the current background count rate be known.

As explained earlier, the background signal was periodically sampled.

The mean of all these samples is used to predict the background content of any one photon measurement. In a typical experiment, about 275 background samples were taken. The statistical variation in these measurements was generally about 12 percent. It was this variation that was responsible for the error introduced by background counts. Because the photon signal decreases with increasing energy, this error became a major experimental limitation at energies beyond 300 keV.

Photons generated by the interaction of the beam with the background gas also constituted a serious problem. This additional background signal is proportional to the beam current and background gas density which was a function of X due to pumping gradients. This background gas is primarily due to gas flow out of the target cell through the cell exit orifice. A small percentage is due to residual gas which results from out gassing. The background gas signal contribution was determined before each experiment by the following procedure. The pressure in the observation chamber is measured by an ionization gauge with the nominal target pressure in the cell. Gas to the target cell is then shut off and the ion gauge reading is reproduced by injecting target gas directly into the observation chamber. A scan of background signal against position was then made.

Errors in the photon signal could result from both short and long term changes in the overall sensitivity of the photon detection system due to changes in the counting electronics, aging of the interference filter, etc. To guard against this type of error, a standard light signal was measured before and after each experiment. The standard was constructed from a tritium decay light source; the nature of this source is discussed in detail in the section dealing with the absolute calibration of the system.

In addition to checking the stability of sensitivity during an experiment, the standard provides a means to normalize all the data to a particular source strength.

Position dependent variations in the sensitivity such as those due to misalignment of the photomultiplier track and changes in the transmission of the windows were checked and eliminated. No effects from the X-ray field produced by the accelerator were observed below 400 keV. Above this energy some effects were observed; however, the X-ray field appeared to be fairly uniform in X (photon detector position) and therefore had only the effect of introducing an increased effective photomultiplier background signal.

Finally, it should be mentioned that the natural statistical spread in the detected photon counts constituted a significant error--particularly at high energy where small photon signals were observed.

Measurement of Photon Detector Position. The position of the photomultiplier was measured by a traveling potentiometer whose output was digitized by a voltage to frequency converter. The accuracy of this electronic system was assessed to be better than 0.1 percent for most positions. One additional source of error in determining position of photomultiplier is in the location of point of actual termination of the target cell. Several independent measurements of this point were made; all agreed to within about 0.6 percent of each other. However, the maximum resultant error in the parameter, X--occurring at the initial value (X = 0)--may have been as large as 6 percent.

The dimensions of the target cell and accompanying apparatus were well known; thus, the zero position of the photomultiplier could be determined

by direct measurement. As additional insurance, two supplementary methods were used to determine the location of the zero position, X = 0:

Method 1. In one experiment, the observation chamber was filled to several microns of pressure with helium. A target excitation line, near 4437 Å , was observed as a function of position. From the loss of signal near the end of the scan of position, the zero was inferred.

This method is not particularly accurate because of a pressure depression near the target cell exit orifice and optical aberration. It was, however, in reasonable agreement with the direct measurement.

Method 2. A more accurate method consisted of mounting a precision light source on the exit orifice of the target cell. This source was made from an accurately machined metal cylinder containing a tritium decay lamp. At five precisely known locations, small pin holes were bored into the cylinder to serve as point sources. The end of the cylinder was placed in contact with the end of the exit orifice, and a scan across the five sources was made with the photomultiplier. Five determinations of the zero position were thus obtained.

Measurement of Target Density. The determination of target density is fraught with several sources of error. During the course of the experiment, the temperature of the target cell generally increased from 3 to 6 degrees above ambient room temperature. (This was most likely due to heat dissipated by the beam in the collimators.) This would ordinarily introduce a 1 to 2 percent error in the calculation of target density; but this effect was taken into account by periodically measuring the temperature of the walls of the target cell. Because the pressure sensor operated at a regulated temperature several degrees above that of the target

cell, a small correction due to thermal transpiration[18] also included. The two automatically operated electropneumatic valves connecting the pressure sensor to the target cell and collimation chamber (zero pressure reservoir) were found to dissipate a significant amount of heat during operation. In order to eliminate additional transpiration effects, these valves were provided with water cooled jackets.

The most important source of error is in the direct measurement of pressure where zero drift in the electronics of the capacitance manometer presents a problem. This drift introduced a larger percentage error at lower energies where smaller target pressures must be used to avoid multiple collision effects. As an example, at 75 keV zero drift is responsible for an error of about 1 to 2 percent for targets of nitrogen and argon and 0.3 percent for hydrogen and helium. At 250 keV, these errors are only 0.2 and 0.1 percent, respectively. Since photon signals increase at lower energies (because of larger cross sections), errors in pressure were partially compensated by greater statistical accuracy. However, because a relatively high degree of accuracy is required to resolve the p and d state contributions, special care was taken to minimize the effect of zero drift. With the pressure sensor in the zero mode every fourth cycle, it was possible to constantly rezero the manometer. Further, it was possible to rezero after the magnitude and polarity of the drift had been recorded. Hence, these short term drifts could be accounted for in the computer analysis. Some slower drift in the electronic sensitivity of the manometer could also be observed. It, too, was periodically corrected but typically amounted to less than 0.5 percent.

Errors and drifts associated with the calibration of the manometer

were small and affected only the absolute cross section and not the determination of the cross section ratios.

Measurement of Beam Flux. Electronic errors, such as zero drift, changes in sensitivity, and leakage currents, appeared to be negligible in the measurement of beam charge. The most important problem was the divergence of the beam. Projectiles too divergent to enter the Faraday cut were intercepted by a metal electrode. Since the emission of secondary electrons was not taken into account, the measured positive current from this electrode was surely an overestimate of the actual divergent current (including both ions and neutrals); generally, the divergent current could be maintained at less than a percent of the main beam.

Some error results in assuming that proton flux entering the target cell is equal to the partially neutralized beam detected at the Faraday cup. This problem is discussed in detail in the next chapter.

Mathematical Analysis

Because of the enormous number of calculations required to calculate the capture cross section from the array of measurements determining I(X), the mathematical analysis was computerized. In order to gain some insight into the nature of the least squares analysis employed, a number of computer model studies were made.

Data Analysis

As mentioned previously, the end product of the experiment was a punched tape which was converted to cards and then fed into the Burroughs computer along with the appropriate computer program. For this experiment, several Algol programs were developed for the various types of analysis required.

The most important program for the separation of the 3s, 3p, and 3d cross sections can be described briefly as follows: A number of initial experimental parameters were read in via a free field format. This was followed by several data arrays (perhaps 30 to 40) similar to those mentioned earlier. Each was preceded by a card describing the photon signal due to the interaction of the beam with the background gas at the corresponding photomultiplier position. From this data, a corrected projectile number-target number density normalized signal, NSI[I], was determined for each position, XI [I], along with an analysis of the errors inherent in the calculation of NSI[I]. (Here again, I indexes all the parameters pertaining to the measurement of the intensity, I(X), at a particular position (X_I)- that is, for a particular I^{th} data point.) These errors included the measured errors (due to drift) in the determination of pressure and charge, other various predicted systematic errors, and the intrinsic errors due to the measured statistical variations in the actual photon and dark current noise counts. Via a Gauss-Jordan reduction prodcedure, a least squares fit was than made for the functional dependence of the signal, NSI[I], on the position, XI[I], to an equation representing an ideal decay of the form:

$$\begin{aligned} NSI[I] &= C_{3s} \exp\,(XI[I]/X_{3s}) \\ &+ C_{3p} \exp\,(XI[I]/X_{3p}) \\ &+ C_{3d} \exp\,(XI[I]/X_{3d}) \end{aligned} \tag{19}$$

Here, X_{3s}, X_{3p}, and X_{3d} are the known decay lengths appropriate to the corresponding state of excitation. From the coefficients--C_{3s}, C_{3p}, and C_{3d}-- the appropriate cross sections were calculated. Following these

calculations, the predicted ideal decay curve was generated. From the deviation between the ideal and actual curve, calculations were made which assessed the overall quality of the deconvolution procedure.

Range of Validity

In order to assess the validity of the data analysis, a computer model of the deconvolution procedure was developed. An initial ideal set of measurements, $\{X_i, I_i(X_i)\}$, was generated from the relation described by Equation 17. Realistic values were chosen for the coefficients, C_{3s}, C_{3p}, and C_{3d}. A second perturbed set, $\{X_i, I(X_i, {}_i)\}$, was generated by altering one or more of the parameters defining I(X) by the addition of an error, ϵ_i. The second set was deconvolved to yield the perturbed coefficients, C''_{3s}, C''_{3p}, and C''_{3d}. These coefficients define a best fit intensity, I''(X), which can then be compared to the ideal function.

For all the model calculations presented here, the data set, $\{X_i\}$, was selected from a typical experiment. Since the photon detector was scanned in a systematic manner, this set was fairly representative of all the experiments. Variation of the data set, $\{X_i\}$, will change the differences, $C_{3\ell}-C''_{3\ell}$; however, the magnitude of these changes is slight unless the distribution of points along the X axis is altered drastically. The qualitative behavior of $C_{3\ell}-C''_{3\ell}$ is generally preserved under a change of the data set, $\{X_i\}$.

Errors in the Photon Measurement. The effect of errors in the measurement of the photon count at the various X positions was determined by generating the perturbed intensity in the following manner:

$$I'(X) = I(X) + \epsilon(I(X)) \tag{20}$$

Here, ϵ represents the error due to the natural statistical spread in the photon count and manifests an implicit X dependence since the photon count becomes smaller with increasing X. $\langle\epsilon\rangle$ was assumed to be proportional to $\sqrt{I(X)}$.

The set, $\{\epsilon_i\}$ was normally distributed. It was generated by first generating an initial set of random numbers, $\{n_i\}$, in the interval, [-1, 1]. This set was transformed to a normal set by the inverse error function:

$$\{n_i\} \rightarrow \{\mathrm{erf}^{-1}(n_i)\} \tag{21}$$

Figure 4 gives an example of the effect of statistical variations in the photon measurement for three energies, 75, 150 and 300 keV. The ideal case is characterized by the point, [0.3, 0.3], in the $\{C_{3p}/C_{3s}, C_{3d}/C_{3s}\}$ plane. The additional points result from ten deconvolutions for ten arbitrary error sets, $\{\epsilon_i\}_j$. The solid points represent the model calculations for an initial measurement of 500 photon counts at the first position, X = 0.92 cm; the circles are for data with 10,000 initial counts. In the first case, the errors are initially 4.47 percent (at X = 0.92 cm); at large X (44.92 cm), the errors have increased to 7.36 percent at 150 keV energy. For 10,000 initial counts, the same errors are 0.10 and 1.65 percent respectively.

The scatter of the points, $\{C_{3p}/C_{3s}, C_{3d}/C_{3s}\}$, about the ideal point, [0.3, 0.3], reveals the effect of statistical variations in I(X) on the deconvolution procedure. Note that the points tend to scatter along the $\frac{C_{sp}}{C_{3s}} + \frac{C_{3d}}{C_{3s}} = .6$ line; that is, the $C_{3p} + C_{3d}$ to C_{3s} ratio is preserved. In

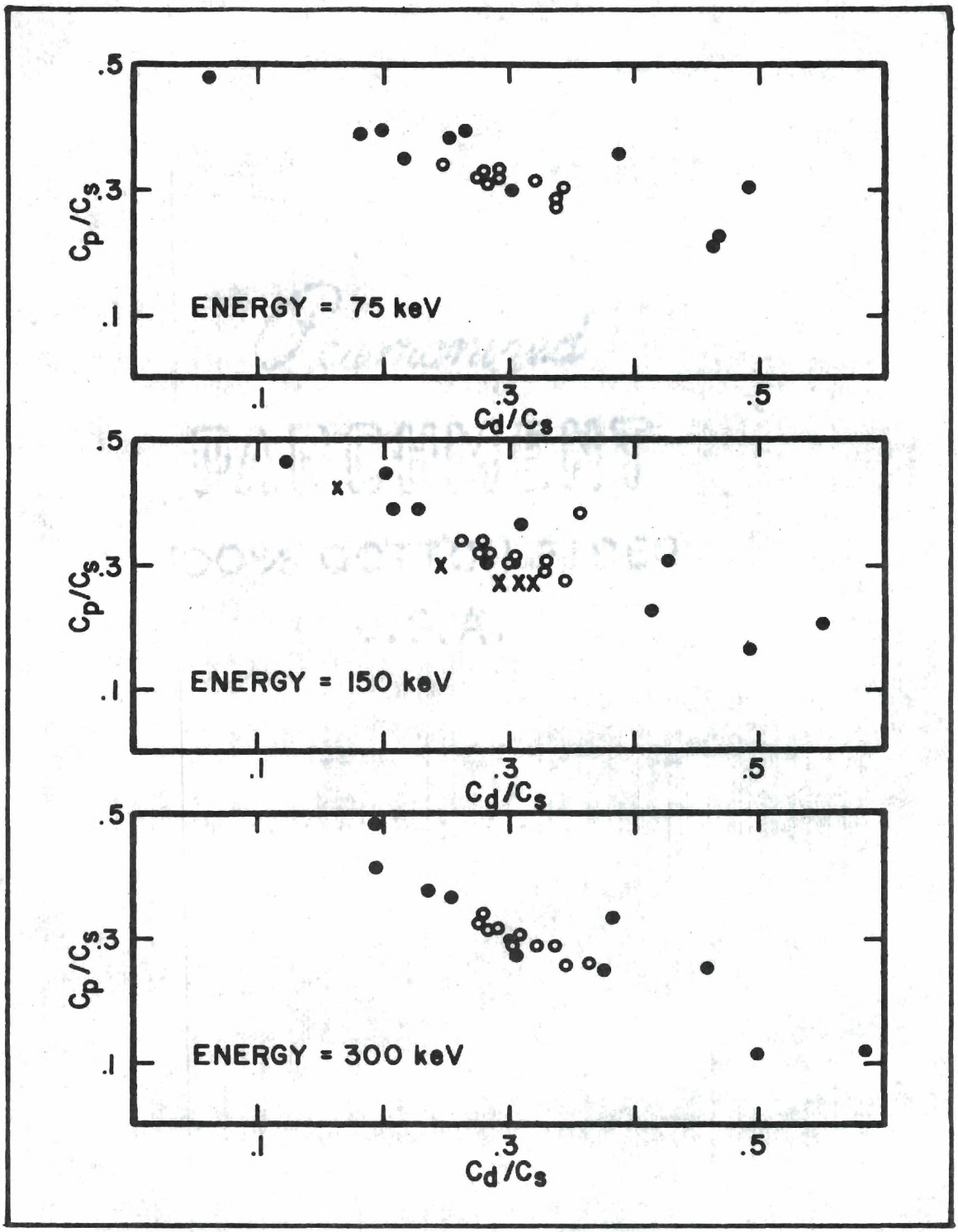

Figure 5. Effects of Statistical Errors Upon the Deconvolution of a Model Intensity Function, I(X).

addition there appears to be some tendency to detract from the s state. As a result, in cases where the count rates are low, one expects the errors to favor the p and d states.

For real experiments there are likely to be additional random errors in I(X); hence, these model calculations may slightly underestimate the scatter in the real data. Included with the 150 keV calculations (Figure 5) are some actual data for nitrogen. The scatter in these data (represented by X's on the graph) is very similar to that predicted by the model calculations.

Changes in the Lifetime. Tables 1, 2, and 3 give the effects of changes in the 3s, 3p, and 3d lifetimes at 150 keV. The ideal intensity is characterized by $\frac{C_{sp}}{C_{3s}} = .3$ and $\frac{C_{3d}}{C_{3s}} = .3$, which is most representative of a nitrogen target. Here, the percent variation in $\tau_{3\ell}$ is tabulated against the percent deviations between the real and deconvolved coefficients, $C_{3\ell}$ and $C'''_{3\ell}$. In addition, the percent changes in the ratios, C_{3p}/C_{3s} and C_{3d}/C_{3s}, are given; these quantities are designated ΔR_{3p} and ΔR_{3d}. The quantities $\Delta C_{3\ell}$ and $\Delta R_{3\ell}$ are given by the equations:

$$\Delta C_{3\ell} = \frac{C_{3\ell} - C'''_{3\ell}}{C_{3_\ell}} 100 \tag{22}$$

$$\Delta R_{3\ell} = \left[\frac{C_{3\ell}}{C_s} - \frac{C_{3\ell}'''}{C_s}\right]\frac{C_s}{C_{3\ell}} 100 \tag{23}$$

Figures 6, 7, and 8 give the energy dependence of ΔR_{3p} and ΔR_{3d} for $\pm$ 30 percent changes in τ_{3s}, τ_{3p}, and τ_{3d}. The dependence of $\Delta R_{3\ell}$ upon E is qualitatively the same for other positive or negative variations in $\tau_{3\ell}$.

Table 1. Variation in the 3s Lifetime at 150 keV Energy

Percent Change In τ_{3s}	ΔC_{3s}	ΔC_{3p}	ΔC_{3d}	ΔR_{3p}	ΔR_{3d}
-40	-26.1	-104.1	+169.2	-105.5	+264.1
-20	-10.8	+45.3	+71.7	-38.8	+92.4
-10	-4.9	+21.2	+33.2	-17.1	+40.1
+10	+4.3	+18.7	-28.9	+13.8	-31.8
+20	+7.9	+35.2	-54.2	+25.2	-57.5
+40	+14.0	+62.9	-96.3	+42.9	-96.7

Table 2. Variation in the 3p Lifetime at 150 keV Energy

Percent Change In τ_{3p}	ΔC_{3s}	ΔC_{3p}	ΔC_{3d}	ΔR_{3s}	ΔR_{3p}
-40	-0.7	+4.6	-27.5	+3.7	-28.1
-20	+0.4	+6.6	-15.1	+6.1	-15.5
-10	+0.2	+4.0	-7.7	+3.8	-7.9
+10	-0.2	-4.9	+7.7	-4.7	+7.9
+20	-0.3	-10.4	+15.3	-10.1	+15.7
+40	-0.6	-22.3	+29.7	21.8	+30.4

Table 3. Variation in the 3d Lifetime at 150 keV Energy

Percent Change In τ_{3d}	ΔC_{3s}	ΔC_{3p}	ΔC_{3d}	ΔR_{sp}	ΔR_{3d}
-40	-0.7	+56.0	-47.7	+57.2	-47.3
-20	-0.6	+24.7	-19.5	+25.4	-19.0
-10	-0.3	+11.5	-8.8	+11.9	-8.5
+10	+0.4	-10.0	+7.2	-10.4	+6.8
+20	+0.8	-18.7	+13.0	-19.4	+12.1
+40	+1.7	-32.6	+21.2	-33.8	+19.2

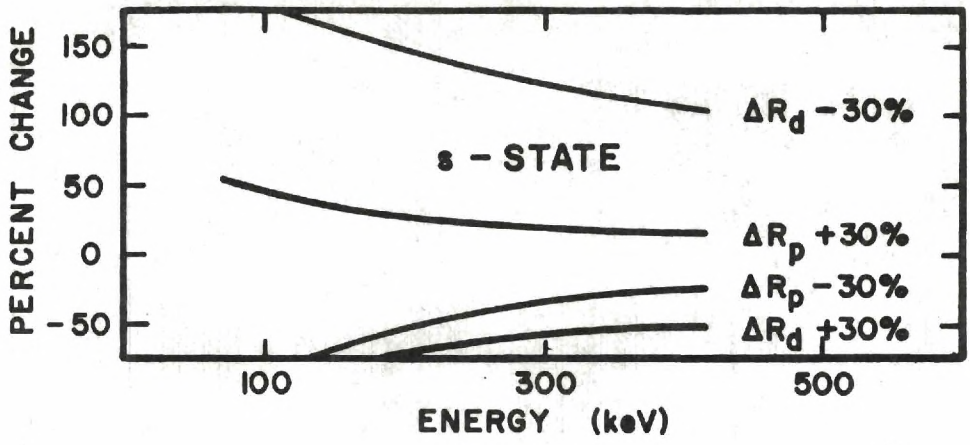

Figure 6. Effect of Errors in the 3s Lifetime.

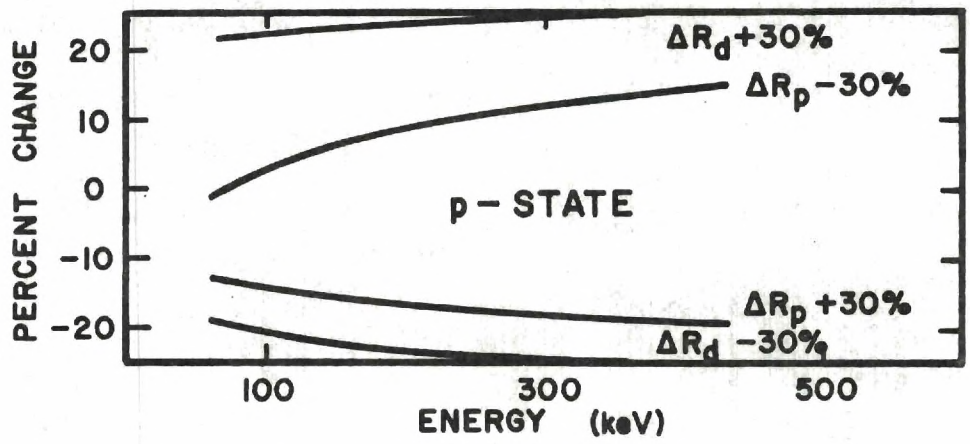

Figure 7. Effect of Errors in the 3p Lifetime.

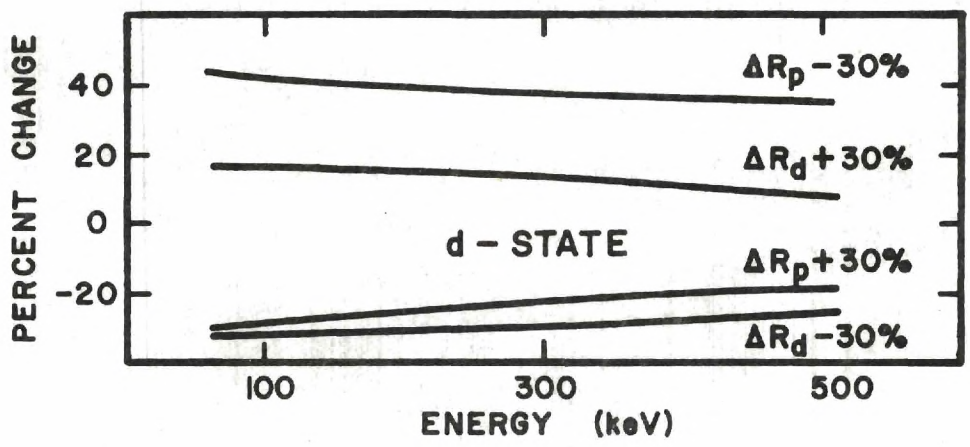

Figure 8. Effect of Errors in the 3d Lifetime.

Changes in the Beam Velocities. Table 4 summarizes the calculation for the effect of variations in the beam velocity. The percent change in the velocity is tabulated against $\Delta C_{3\ell}$ and $\Delta R_{3\ell}$. The normal velocity, 5.36×10^{-8} cm. per sec., corresponds to a proton energy of 150 keV. Again, the ideal intensity is characterized by .3 and .3 for C_{3p}/C_{3s} and C_{3d}/C_{3s}.

Table 4. Variation in the Beam Velocity about V for 150 keV Energy

Percent Change in Beam Velocity	ΔC_{3s}	ΔC_{3p}	ΔC_{3d}	ΔR_{3p}	ΔR_{3d}
-40	-25.9	-43.5	+94.1	-23.7	+162.0
-20	-10.9	-14.1	+37.1	-3.6	+53.9
-10	-5.1	-5.7	+16.7	-0.7	+22.9
+10	+4.4	+3.7	-14.0	-0.7	-17.6
+20	+8.4	+6.0	-25.9	-2.2	-31.6
+40	+15.2	+8.0	-45.4	-6.2	-52.6

Figure 9 displays the energy dependences of ΔR_{3p} and ΔR_{3d} for velocity variations of $\pm$ 30 percent.

Conclusion. Statistical variations in I(X) manifest an implicit dependence upon X; their effects upon the coefficients $C_{3\ell}$ are predictable by model calculations. It is very important to recognize the nature of these effects. At high energy (>250 keV) the statistical accuracy is low. In this region, statistical errors tend to systematically enhance the results for the p and d cross sections.

The effects of variations in the lifetimes are significant for changes as small as ten percent. The effects of changes in $\tau_{3\ell}$ are summarized in Tables 1, 2 and 3 and Figures 6, 7 and 8. It should be pointed out that errors in the lifetimes will not be evident from deviation between the experimental intensity, I'(X) and the deconvolved intensity,

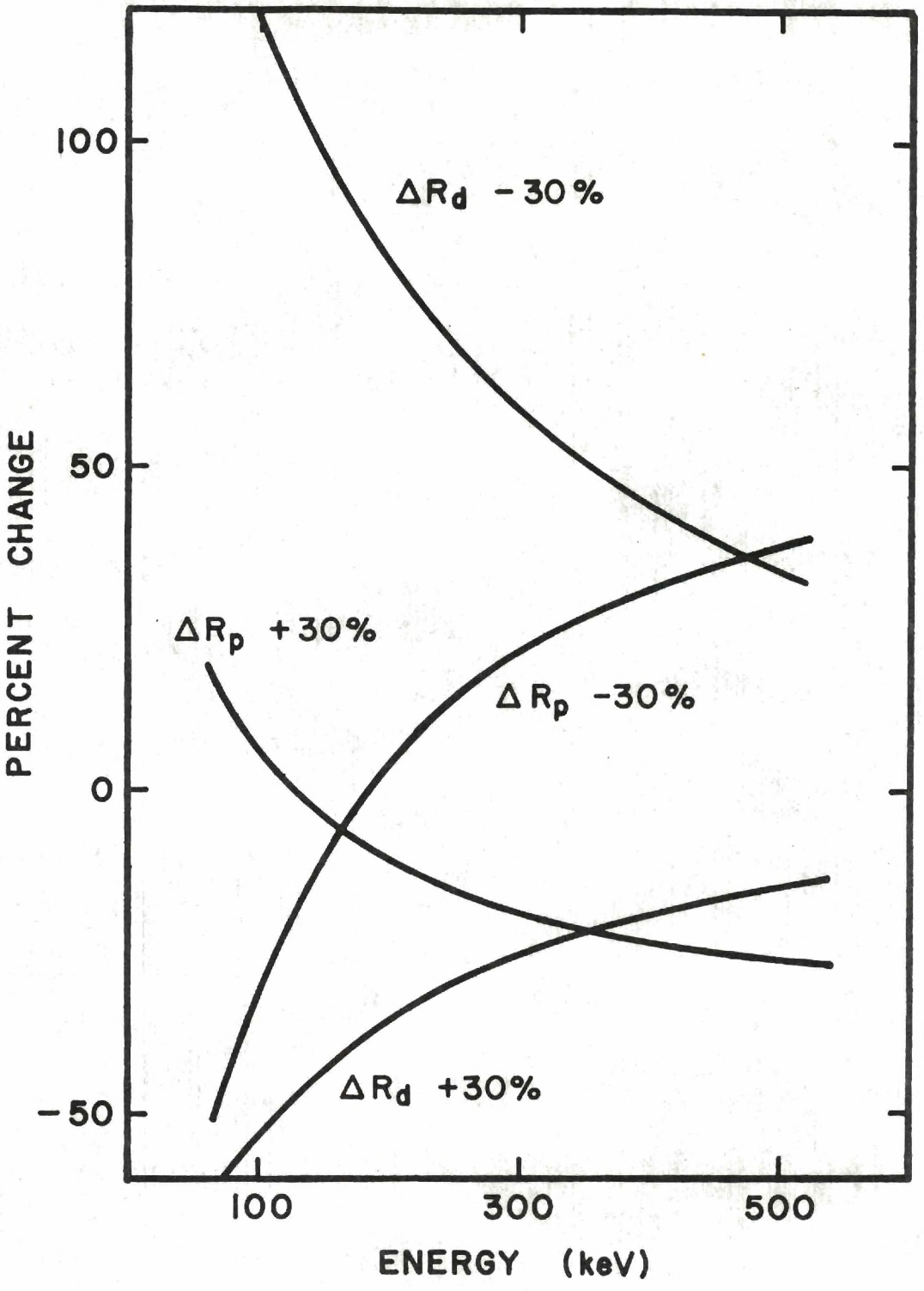

Figure 9. Effect of Errors in the Beam Velocity upon the Ratios of the p and d to s State.

I''(X). For example, the mean deviations between I'(X) and I''(X) (averaged over the set, $\{X_i\}$) for a variation of -50 percent in τ_{3s} at 75, 150 and 300 keV energy are only -2.3, -0.7 and -0.2 percent respectively. For a variation of +50 percent in τ_{3s}, the corresponding mean deviations are 1.5, 0.4 and +3.4. Hence, the quality of the deconvolution will appear to be high for any real situation where statistical variations are also present. The lifetimes, therefore, must be well known input parameters. For this work, the following theoretically determined values were used.

$$\tau_{3s} = 15.84 \times 10^{-8} \text{ sec.} \tag{24}$$

$$\tau_{3p} = 0.5273 \times 10^{-8} \text{ sec.} \tag{25}$$

$$\tau_{3d} = 1.547 \times 10^{-8} \text{ sec.} \tag{26}$$

These values are believed to be accurate to within one percent.[19] Recently, Chupp et al,[20] have confirmed these values using a beam-foil excitation technique. Their experimental lifetimes are very slightly higher than our theoretical values--1, 4.3 and .8 percent for τ_{3s}, τ_{3p} and τ_{3d} respectively.

The effects of errors in the beam velocity are summarized in Table 4 and Figure 8. Here again, the mean deviations between I'(X) and I''(X) are small even for +50 percent changes in velocity. Hence, as with the lifetimes, the beam velocity must be well known. The error in the beam energy is estimated to be less than two percent over the entire energy range. Such an error results in about a one percent error in velocity; this does not significantly effect the deconvolved coefficients.

Finally, it should be noted that the results presented in this section are for an ideal intensity characterized by $C_{3p}/C_{3s} = C_{3d}/C_{3s} = 0.3$. This intensity is most representative of a nitrogen or argon target. Helium and hydrogen appear to be better represented by the ratios, $C_{3p}/C_{3s} = 0.1$, $C_{3d}/C_{3s} = 0.05$ and $C_{3p}/C_{3s} = 0.3$, $C_{3d}/C_{3s} = 0.1$, respectively. These ratios give slightly different results than those suggested by Figure 4. We shall summarize the results for H_e and H_2 targets in Chapter IV.

CHAPTER III

INTERPRETATION OF BEAM EMISSION

In the last chapter, we discussed the accuracy with which the experimental parameters required to determine $Q_{n\ell}$ could be measured; we shall now consider the interpretation of the emission intensity, I(X), as defined by Equation 17.

There are a number of effects which could conceivably alter the simple model determining Equations 17 and 18. In this chapter, we shall consider the actual density profile of targets in the cell, beam neutralization, multiple collision effects, cascade, and the Stark mixing of the $3p_{3/2}$ and $3d_{3/2}$ levels. Finally, we shall discuss the quantitative measurement of beam emission with the objective to clearly define the relationship between the measured intensity and the ideal function, I(X), of Equation 17.

Target Density Profile

In the solution to Equation 12, we assumed that the target density, ρ, was constant; thus, the beam was assumed to encounter a step function target density profile. There are three major departures from this idealization. First, approaching either the entrance or exit orifice, one should encounter a target density depression. Since the solid angle defining the entrance to the exit or entrance canal represents a region from which the flow of target particles is reduced. As one enters the canal, a further continuous loss of density is apparent. Emerging from the canal,

one expects a density profile rapidly attenuated by the spherical expansion of the gas into the vacuum. Using even the simplest assumptions of molecular flow, one derives rather complicated corrections which are quite difficult to evaluate exactly.

It is most convenient to directly numerically integrate Equation 18 for a realistically chosen density profile. Such a profile, based on molecular flow calculations, is shown in Figure 10. The shape of the profile beyond the cell appeared to be consistent with the observation of light from proton impact excitation of helium gas flowing out of the target cell. The corrections to the solution of Equation 13 are determined by the functions, $G_{3\ell}(E)$. These functions yield the corrected intensities via the relation:

$$I_{3\ell}(X) = A(3\ell \rightarrow n=2)\ F^{+}\ \rho\ G_{3\ell}(E)\left(1 - e^{-\frac{L}{X_{3\ell}}}\right)e^{-\frac{X}{X_{3\ell}}} \qquad (27)$$

ρ is the maximum density determined many orifice diameters from either the entrance or exit aperture.

Figure 11 gives $G_{3s}(E)$, $G_{3p}(E)$, and $G_{3d}(E)$ as a function of proton energy. The largest correction is required for the 3p state; this is primarily due to the loss of 3p atoms, due to spontaneous decay, in the exit channel of the cell.

Beam Neutralization

The quantity, F^{+}, in Equation 12 and 13 is calculated directly from the amount of charge entering the Faraday cup. Since neutral beam particles make no contribution to this charge, the neutralized component of the total beam flux makes the incident projectile flux appear too small and, hence,

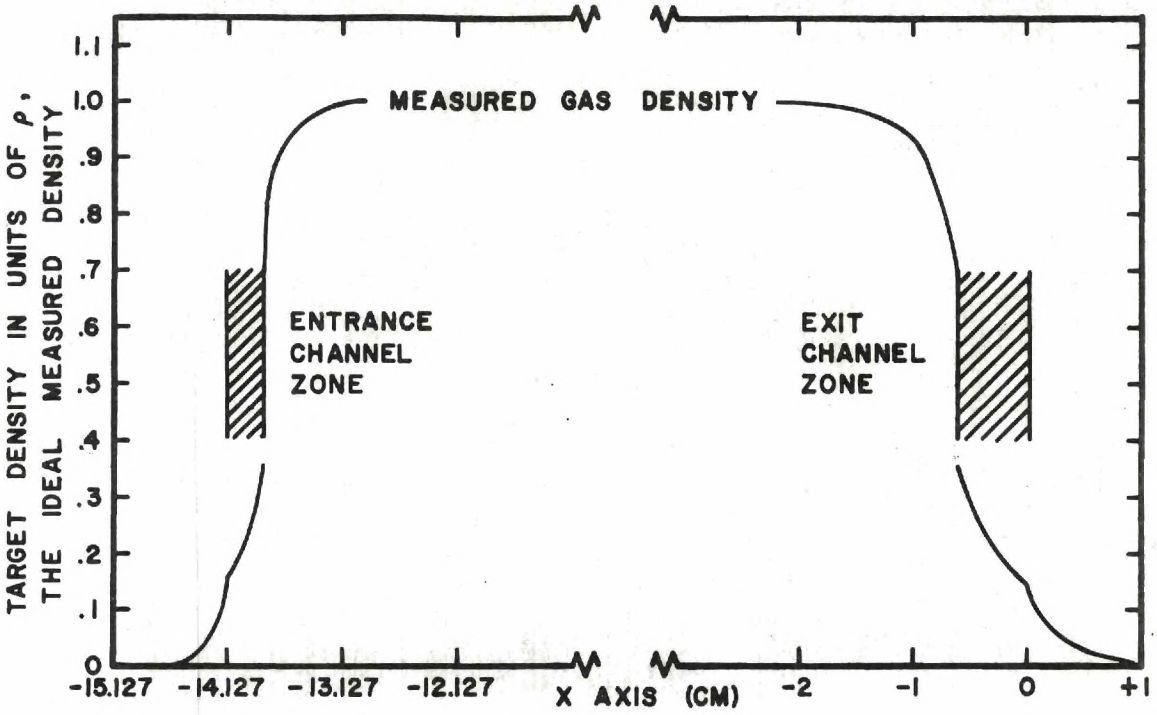

Figure 10. The Gas Density Profile in the Target Cell.

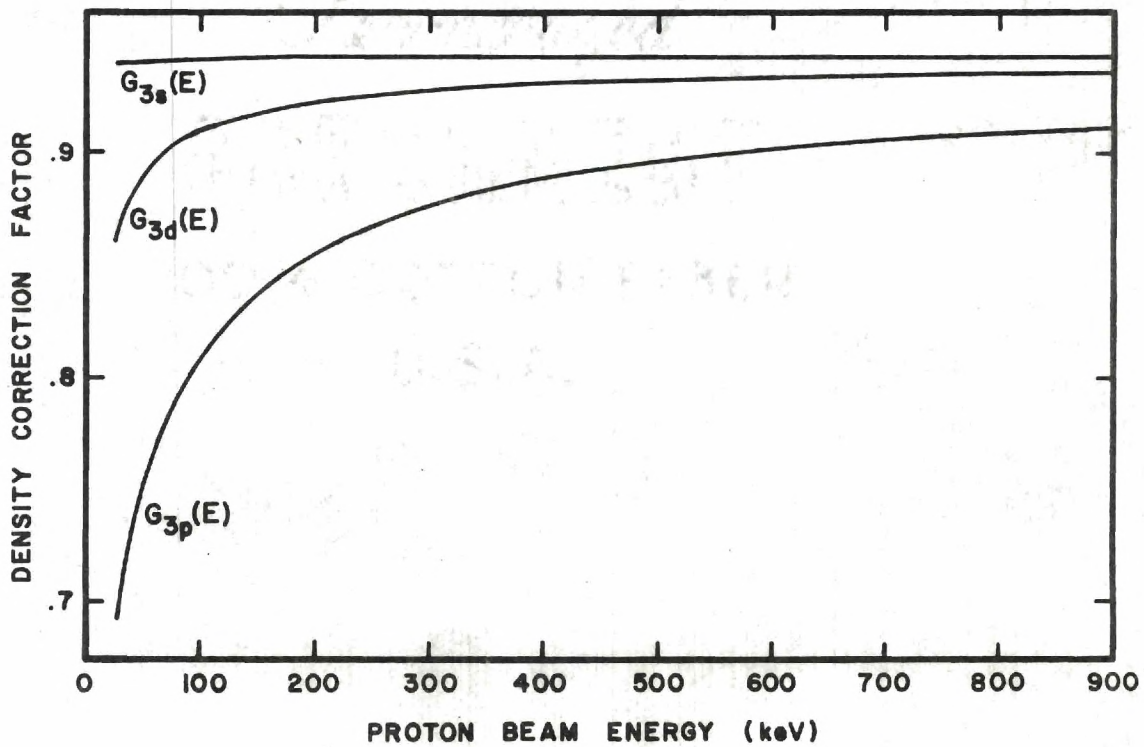

Figure 11. Density Profile Correction Factors, $G_{3\ell}(E)$ vs Proton Beam Energy.

the cross section too large. Moreover, F^+ is a function of X since there is a continuous depletion of charged projectiles along the trajectory through the cell.

The functional dependence of F^+ can be obtained directly from the total cross sections for neutralization, Q_{+o}, and for subsequent reionization, Q_{o+}. It should be remembered that these cross sections are dependent upon energy and will give rise to corrections which are implicit functions of beam energy. The populations of neutrals and ions in the beam are governed by two simultaneous first order equations:

$$\frac{dN_+}{dX} = - N_+ Q_{+o} \rho + N_o Q_{o+} \rho \tag{28}$$

$$\frac{dN_o}{dX} = - N_o Q_{o+} \rho + N_+ Q_{+o} \rho \tag{29}$$

In addition, we have conservation condition:

$$N_+(X) + N_o(X) = N_+(X = 0) \tag{30}$$

From the solution of Equations 28, 29, and 30 and the general form of Equation 9, we can express the total charged flux, $F^+(X)$:

$$F^+(X) = \frac{F^+(0)}{Q_{+o} + Q_{o+}} (Q_{o+} + Q_{+o}) \, e^{- (Q_{+o} + Q_{o+}) \rho X} \tag{31}$$

Experimentally, we measure $F^+(L)$; hence, Equations 17 and 18 must contain a correction factor for beam neutralization:

$$W(E,L) = \frac{Q_{+o} + Q_{o+}}{Q_{+o} + Q_{o+} e^{-(Q_{+o} + Q_{o+}) \rho L}} \tag{32}$$

Barnett et al.,[21,22] have measured the total cross sections, Q_{+o} and Q_{o+} for high energy protons onto targets of N_2, Ar, H_2, and He. From this data, the correction factors, W(e,L), for charge transfer can be calculated. The largest correction in this experiment is for N_2 and Ar targets at 0.25 microns pressure and 75 keV proton energy and amounts to only two percent.

The population factors, $N_{3\ell}(X)$ and $C_{3\ell}$, can be redetermined by substitution $F^+(X)$ in Equation 12. The solution to this more complicated equation yields the corrected population, $C'_{3\ell}$:

$$C'_{3\ell} = \rho\, Q_{3\ell}\, (W(E,L)\, F^+(L)\, \frac{1}{(Q_{+o} + Q_{o+})X_{3\ell}} \quad \frac{Q_{o+}}{\frac{1}{X_{3\ell}}}$$

$$+ \frac{Q_{+o}}{\frac{1}{X_{3\ell}} - \rho(Q_{+o} + Q_{o+})} \quad (1 - e^{-\frac{L}{X_{3\ell}}}) \qquad (33)$$

$$- \frac{Q_{+o}}{\frac{1}{X_{3\ell}} - \rho(Q_{+o} + Q_{o+})} \quad (1 - e^{-\rho(Q_{+o} + Q_{o+})L})$$

From this equation, we can define the collisional attentuation function, $U(\rho;\, Q_{+o},\, Q_{o+})$, which gives corrected populations in terms of idealized populations.

$$C'_{3\ell} = C_{3\ell}\, U(\rho;\, Q_{+o},\, Q_{o+}) \qquad (34)$$

The behavior of $U(\rho;\, Q_{+o},\, Q_{o+})$ has been studied extensively; this is discussed in detail in the next section where additional collisional effects are included.

Multiple Collisions

Multiple collisions can play an important role in populating the n = 3 states. For example, neutrals in the beam formed by charge transfer with the target may make transitions into the n = 3 states as a result of secondary collisions. This effect is almost completely dominated by the collisional excitation of ground state neutrals since they constitute most of the neutral current in the beam. In addition, n = 3 state atoms may be destroyed by secondary collisions--primarily by reionization according to the theoretical predictions of Bates and Walker[15].

The cross sections for collisional excitation and destruction are likely to be larger than those for direct charge transfer into the n = 3 level; however, it should be remembered that they do not have a dominant influence on the structure of the intensity function since they are manifest only through secondary and hence less probable collisions. Obviously, multiple collision effects do not effect the form of the intensity, I(X), beyond the target cell; they may, however, force us to reinterpret the initial coefficients, $C_{3\ell}$, of Equation 17.

Mathematical Formulation

Equation 12 can be modified to describe the multiple collision effects by the addition of terms describing the loss of n = 3 atoms by destruction and the population of n = 3 level by neutral excitation:

$$N'_{3\ell}(X) = \frac{Q_{3\ell}F^{+}\rho}{V} - \frac{N_{3\ell}(X)A(3\ell)}{V} - \frac{N_{3\ell}\rho Q_i}{V} + \frac{Q_X F^{o}\rho}{V} \qquad (35)$$

Q_i represents the cross section for the collisional destruction of the 3ℓ state. Q_X is the cross section for producing a 3ℓ state by the

collision of any neutral not in 3ℓ state. The solution to this equation leads to a new population factor, $C'_{3\ell}$.

$$C'_{3\ell} = \rho Q_{3\ell} W(E,L)F^{+}(L) \frac{1}{(Q_{+o} + Q_{o+})X_{3\ell}}$$

$$\frac{Q_{o+}}{\frac{1}{X_{3\ell}} + \rho Q_i} + \frac{Q_{+o}}{\frac{1}{X_{3\ell}} + \rho Q_i - \rho(Q_{+o} + Q_{o+})} \left(1 - e^{-(\frac{1}{X_{3\ell}} + \rho Q_i)L}\right)$$

$$- \frac{1}{\frac{1}{X_{3\ell}} + \rho Q_i - \rho(Q_{+o} + Q_{o+})} \left(1 - e^{-\rho(Q_{+o} + Q_{o+})L}\right)$$

$$+ \frac{Q_X}{Q_{3\ell}} \left[\frac{Q_{o+}}{\frac{1}{X_{3\ell}} + \rho Q_i} - \frac{Q_{+o}}{\frac{1}{X_{3\ell}} + \rho Q_i - \rho(Q_{+o} + Q_{o+})}\right] \left(1 - e^{-(\frac{1}{X_3} + \rho Q_3)L}\right)$$

$$+ \frac{Q_X}{Q_{3\ell}} \frac{Q_{+o}}{\frac{1}{X_{3\ell}} + \rho Q_i - \rho(Q_{+o} + Q_{o+})} \left(1 - e^{-\rho(Q_{+o} + Q_{o+})L}\right) \qquad (36)$$

Now, it is possible to derive a more complete collisional attenuation function, $U_{3\ell}(\rho; Q_{+o}, Q_{o+}, Q_i, Q_X/Q_{3\ell})$, such that

$$C'_{3\ell} = C_{3\ell} U_{3\ell}(\rho; Q_{+o}, Q_{o+}, Q_i, Q_X/Q_{3\ell}) \qquad (37)$$

In order to gain an understanding of the effects of multiple collisions, extensive calculations were made of $U_{3\ell}$ for many different combinations of Q_i and Q_i/Q_X.

From Equation 36 it is apparent that one major effect of collisional destruction is to alter the decay length. Hence, it is often convenient to define an effective decay length:

$$X'_{3\ell} = \frac{X_{3\ell}}{1 + \rho\, Q_i\, X_{3\ell}} \qquad (38)$$

The effect of collisional excitation is, of course, to increase the initial population of the 3ℓ state emerging from the cell. The change in the population due to collisional excitation is dependent only upon the ratio of Q_X to $Q_{3\ell}$. In general, the effects of Q_i and Q_X partially cancel.

The dependence of the $U_{3\ell}$ functions upon decay length is particularly interesting. The behavior of each attenuation function, U_{3s}, U_{3p}, and U_{3d}, is distinctly different--even if we assume that the cross sections, Q_X and Q_i, are ℓ invariant. For example, for $Q_X = 0$, one finds that $U_{3\ell}$ generally minimizes for a decay length between X_{3d} and X_{3s}. For small values of Q_i, we have $1>U_{3p}>U_{3s}>U_{3d}$; at larger ρQ_i values, the 3s state population is the most severely affected--$1>U_{3p}>U_{3d}>U_{3s}$.

Experimental Assessment of Multiple Collision Effects

Unfortunately, there is virtually no reliable experimental data for Q_X and Q_i. However, it is possible to assess the magnitude of effects of multiple collisions experimentally. Generally, the effects of multiple collisions are manifest by a non-linear dependence of the intensity I(X) upon target pressure. Unless Q_X is much larger than $Q_{3\ell}$, a given intensity function, $I_{3\ell}(X)$, will exhibit an attenuation with increasing pressure always falling below the ideally linear intensity; this is, in fact, what is observed. In positions where all three states contribute to the intensity, the attenuation inherent in any given state may be masked by the less affected states. For large X, the situation is better defined since we are dealing with $I_{3s}(X)$ alone. For this reason, the relation between

the target cell pressure, P, and $I_{3s}(X)$ at large X was used to determine the regions of linearity. Only pressures within these regions were employed in the measurements of charge transfer cross sections.

The pressure dependence of I(X) was studied extensively at 75, 150, and 250 keV energy for targets of nitrogen, argon, hydrogen, and helium. The larger targets, nitrogen and argon, were found to exhibit the most pronounced departure from linearity. Figure 12 displays the data for nitrogen.

Obviously, one needs to use as low a target pressure as possible to avoid the departure from the ideal linear dependence of I(X) upon P or, alternatively, use the actual data for I(X) versus pressure to make empirical corrections to the observed intensity. If one follows the latter course, it is very difficult to guarantee that the proper corrections are being employed for the 3p and 3d states. In this work, it was possible to make the measurements of I(X) versus X for pressures which appeared to be sufficiently small to avoid appreciable multiple collision effects for all three states.

In addition to investigating the relationship between target pressure and intensity, an attempt was made to measure the cross sections Q_i and Q_X for argon at 75, 150, and 250 keV energy. The results of this work are summarized in Appendix I.

Effect of Cascade

In the last section, we discussed mechanisms for populating the n = 3 states in addition to direct charge transfer that could obscure the meaning of our measured cross sections. These mechanisms arose only through

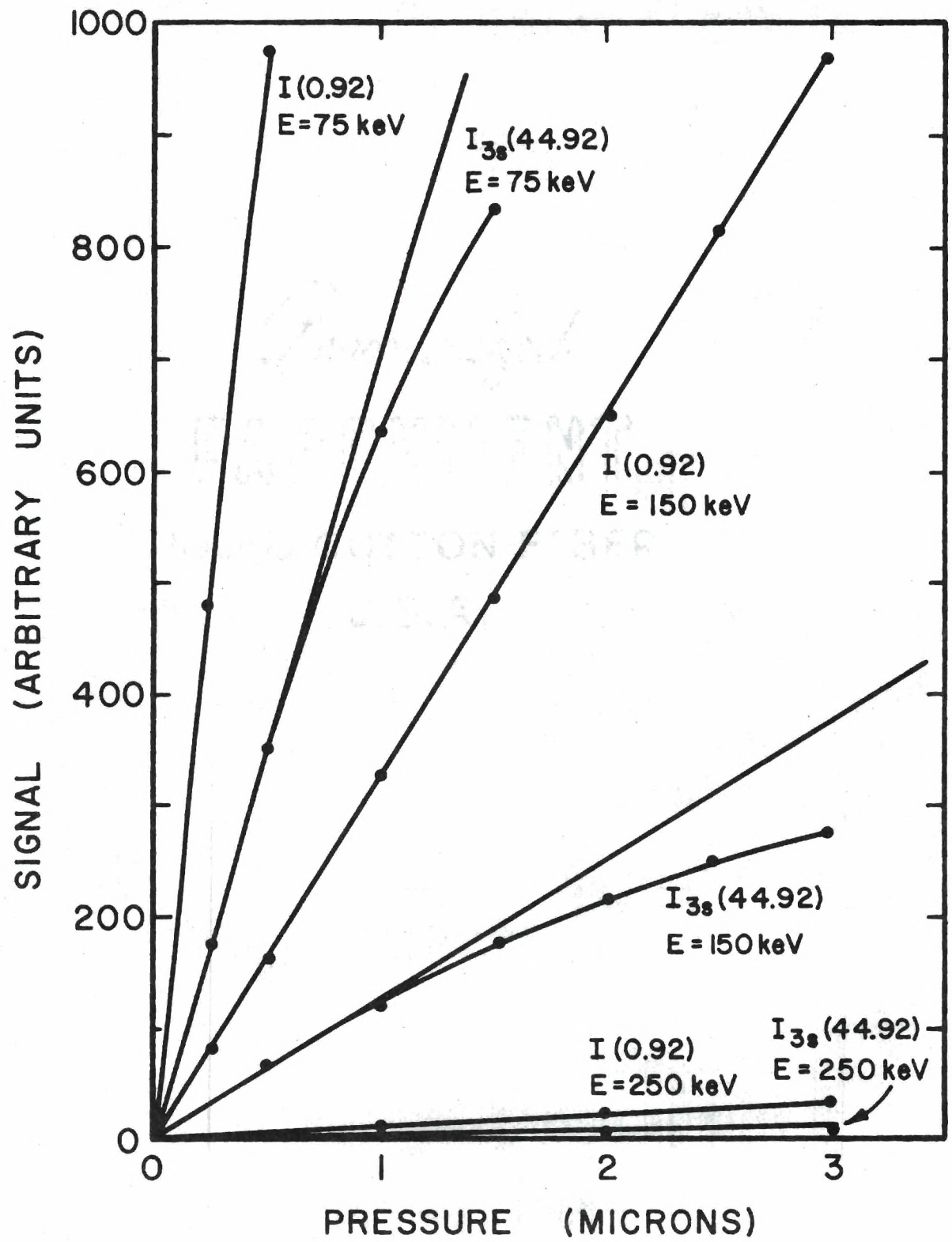

Figure 12. Experimentally Observed Effects of Multiple Collisions for a Nitrogen Target: I(X) vs Target Pressure.

secondary (multiple) collisions which vanish at sufficiently low target density. The 3s, 3p, and 3d states can, however, be additionally populated by cascade from higher states; this mechanism does not require the conditions for multiple collisions. The population by cascade is determined primarily by the direct collisional formation of the higher states (n>3) and the selection rules for downward transitions into the n = 3 level.

The magnitude of the effects of cascade appear to be neglible within the accuracy of our measurements. This might be explained on the basis of three facts:

1. Branching ratios for decay into the n = 3 states are generally small (0.5). Two exceptions are the branching ratios for the 5f and 4f to 3d transitions which are 0.637 and 1.000 respectively.

2. Our measurements of 3ℓ capture cross sections suggest that states with higher orbital angular momentum are less populated.

3. The population of higher states appears to have a n^{-3} dependence upon principal quantum number as suggested by Oppenheimer[11]. If this n^{-3} law is valid, the population of the multitude of states above n = 3 is very sparse; for example, the sum of all ns state capture cross section between n = 4 and n = 500 is only 1.08048 Q_{3s}.

Effects of Cascade in the Target Cell

If terms describing the population due to cascade are introduced into Equation 12, we derive the rate equation:

$$N'_{3\ell}(X) = \frac{F^{+}\rho Q_{3\ell}}{V} - \frac{N_{3\ell}(X)}{X_{3\ell}} + \sum_{n'>3} \sum_{\ell'} \frac{B_{3\ell}^{n'\ell'} N_{n'\ell'}(X)}{X_{n'\ell'}} \qquad (39)$$

$B^{n'\ell'}_{3\ell}$ is the branching ratio for the decay from $n'\ell'$ into the 3 state. From the dipole selection rules, $B^{n'\ell'}_{3\ell}$ is zero unless $\ell = \ell \pm 1$. $X_{n'\ell'}$ is the decay length of the $n'\ell'$ state, $V\tau_{n'\ell'}$.

The solution to Equation 35 can be obtained directly:

$$N_{3\ell}(X) = \frac{F^{+}\rho X_{3\ell}}{V} Q_{3\ell} + \sum_{n'} \sum_{3} \sum_{\ell'} B^{n'\ell'}_{3\ell} Q_{n'\ell'} \left(1 - e^{-X/X_{3\ell}}\right) \tag{40}$$

$$- \sum_{n'} \sum_{3} \sum_{\ell'} \frac{B^{n'\ell'}_{3\ell} Q_{n'\ell'}}{X_{3\ell}} \frac{e^{-X/X_{3\ell}} - e^{-X/X_{n'\ell'}}}{\frac{1}{X_{n'\ell'}} - \frac{1}{X_{3\ell}}}$$

Effects of Cascade Beyond the Target Cell

From Equation 40, we can calculate the population factors, $N_{3\ell}(X)$ and $C_{3\ell}(X)$ at the termination of the cell, X = L. However, beyond the cell, the intensity function is not simply given by Equation 17; the existing higher states continue to populate the n = 3 levels by cascade. In this region, the population $N_{3\ell}(X)$ contains additional cascade terms:

$$N_{3\ell}(X) = N^{0}_{3\ell}(L)\, e^{-X/X_{3\ell}} + \sum_{n'} \sum_{3} \sum_{\ell'} D^{\ell}_{n'\ell'} \frac{e^{-X/X_{3\ell}} - e^{-X/X_{n'\ell'}}}{\frac{1}{X_{n'\ell'}} - \frac{1}{X_{3\ell}}} \tag{41}$$

$N^{0}_{3\ell}(L)$ is the population $N_{3\ell}(X)$ (given by Equation 40) evaluated at the termination of the target cell; in the equation, this is the point X = 0. $D^{\ell}_{n'\ell'}$ is given by the equation:

$$D^{\ell}_{n'\ell'} = \frac{B^{n'\ell'}_{3\ell} N^{0}_{n'\ell'}(L)}{X_{n'\ell'}} \tag{42}$$

Again, $N^0_{n'\ell'}(L)$ is the population $N_{n'\ell'}(X)$ at the termination of the cell; however, this population can be approximated, neglecting cascade from $n''>n'$, by Equation 13.

Magnitude of Cascade Effects

From Equations 43 and 44 calculations of hypothetical intensity functions were made for several possible sets of 4ℓ cross sections. As an example, Figure 13 compares an actual measured intensity, $I_0(X)$, for a nitrogen target at 150 keV with two intensities $I_1(X)$ and $I_2(X)$ calculated using the 3ℓ cross sections from I (X), $Q_{3p}/Q_{3s} = 0.378$ and $Q_{3d}/Q_{3s} = 0.051$. The n = 4 level cross sections are determined by assuming that $Q_{4s} = (3/4)^3\, Q_{3s}$ for $I_1(X)$ and $Q_{4s} = 5Q_{3s}$ for $I_2(X)$. In both cases the higher 4ℓ cross sections are estimated by the equations:

$$\frac{Q_{4p}}{Q_{4s}} = \frac{Q_{3p}}{Q_{3s}} \tag{43}$$

$$\frac{Q_{4d}}{Q_{4s}} = \frac{Q_{4f}}{Q_{4s}} = \frac{Q_{3d}}{Q_{3s}} \tag{44}$$

In all calculations we have assumed that $Q_{3s} = 1$.

In general the deconvolved intensity, I(X) (or $I_0(X)$ in Figure 12) will closely fit the observed intensity at low X even if the observed intensity if not the sum of three exponentials. This is true because at small X all three adjustable parameters (C_{3s}, C_{3p} and C_{3d}) come into play in the deconvolution process. At large X, however, the deconvolved intensity is, by definition, a single s-state decay function. If additional long lifetime states are present in the observed I(X) (as with cascade)

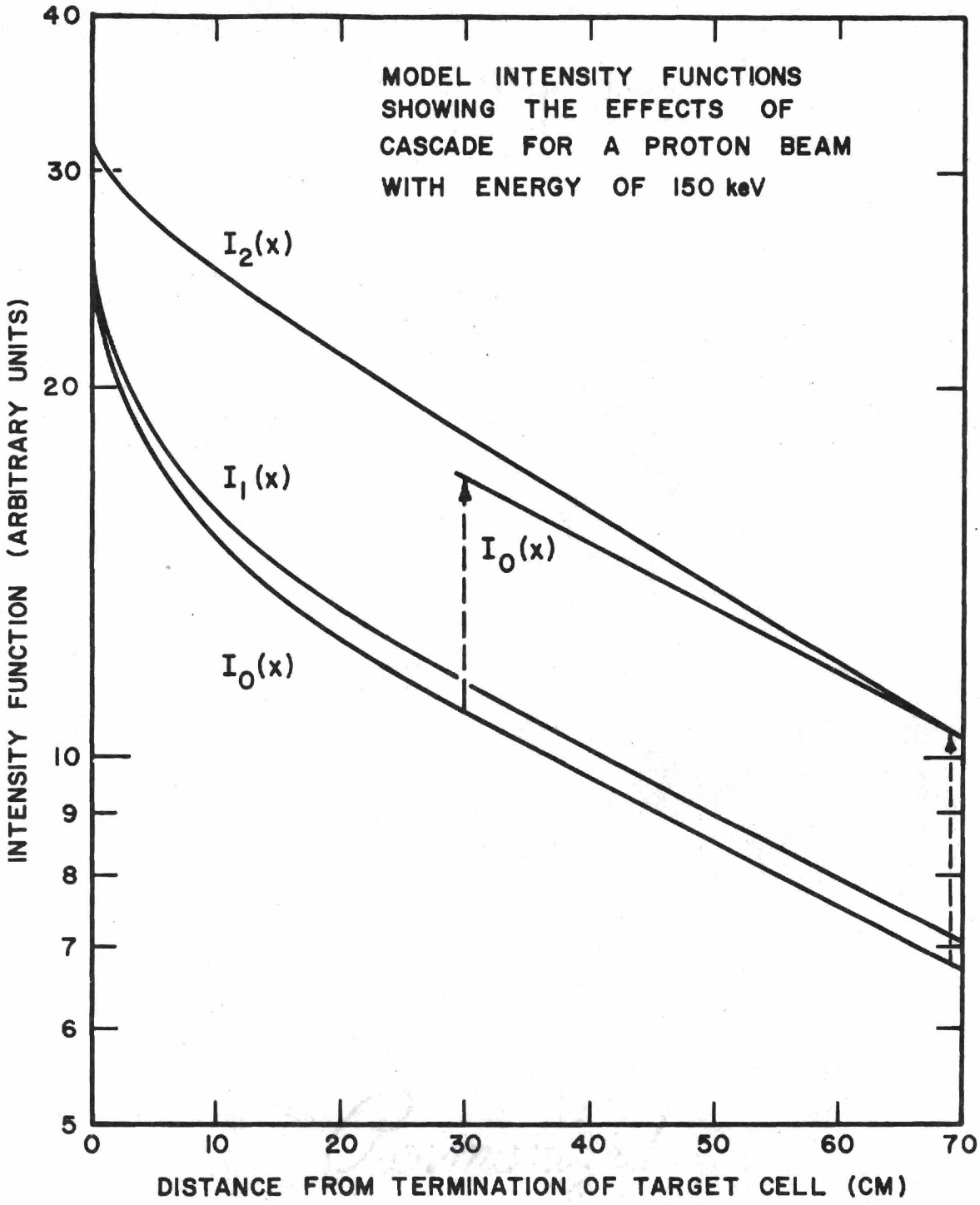

Figure 13. Effects of Cascade from the n=4 Levels at 150 keV Proton Beam Energy.

this function must necessarily deviate from the deconvolved intensity. This effect can be seen in Figure 12; note that $I_1(X)$ and $I_2(X)$ have slopes different from $I_0(X)$.

Unfortunately, unless the effects of cascade are large (as they are for $I_2(X)$), the resultant deviation from a pure 3s decay at large X is too subtle to be observed experimentally. Hence, we cannot verify the existance of effects on order of those described by $I_1(X)$.

Inspection of the deviation between the observed and deconvolved intensities can reveal the presence of cascade effects if the effects are large. At large X, $I_0(X)$ deviated very little from corresponding empirical intensity. For example, at 40 and 50 cm the deviations were only 0.2 and 1.0 percent respectively.

Therefore, we do have experimental evidence that large cascade effects are not present in this data. It seems reasonable to then estimate the magnitude of the errors due to cascade in terms of the assumptions forming basis of the calculation of $I_1(X)$. These errors are summarized in the next chapter.

Stark Effect

Thus far, we have assumed that the excited n = 3 atoms in the beam were fully characterized by the individual free field hydrogenic eigenstates of the quantum numbers, n, ℓ, j, and m_j. This assumption allowed the separation of the total intensity, I(X), into the three components for each orbital angular monentum state, ℓ. If electric fields are present, this assumption is no longer valid; the excited atoms must be described by the Stark perturbed states.

The Weak Field Stark Effect

In the presence of a weak electric field, the quantum states of hydrogen can be described as a superposition of the field free states. Consider an atom in an initial pure state, $|n, \ell, j, m_j\rangle$. If a small electric field is applied, $|n, \ell, j, m_j\rangle$ is perturbed into a state which is a superposition of $|n, \ell, j, m_j\rangle$ and the most nearly energy degenerate neighboring states. If the field is increased, more remote states must be included. The importance of the contribution from a given neighboring state $|n', \ell', j', m_j\rangle$ can be gauged by the ratio, $\langle n, \ell, j, m_j | \mathcal{H}_s | n', \ell', j', m'_j\rangle / E_s$, where $\mathcal{H}_s$ is the Stark Hamiltonian, (ez), and E_s is the field free energy separation between the states. The matrix elements, $\langle n, \ell, j, m_j | \mathcal{H}_s | n', \ell', j', m'_j\rangle$, have been calculated by Rojansky[23] and Schlapp[24]. Since the operator m_j commutes with $\mathcal{H}_s$, the matrix elements are zero unless $m_j = m_j'$.

Since states with the same n, and j and m_j but different ℓ are separated only the Lamb shift, they are the most easily mixed by small electric fields. Larger fields will mix states of different j. When the Stark matrix elements are comparable to the energy separations between states of different principle quantum number, we have complete mixing of all states. Now, the system is described by the well known parabolic quantum numbers n_1 and n_2. Ultimately, m_j is the only surviving original quantum number.

Stark Effect for the n = 3 Level

Spurious fields encountered by the beam are sufficient to mix only states with the same ℓ but different n, j. Further, by the argument of Andreev in Chapter I, we may assume that the atoms are produced in states

of definite ℓ and if fields are present, they will quickly evolve into the Stark perturbed states:

$$|3s_{1/2}\ ;\ m_j\rangle \rightarrow |E'(3s_{1/2});\ n = 3,\ j = 1/2,\ mj\rangle \tag{45}$$

$$|3p_{1/2}\ ;\ m_j\rangle \rightarrow |E'(3p_{1/2});\ n = 3,\ j = 3/2,\ mj\rangle \tag{46}$$

$$|3P_{3/2};\ m_j\rangle \rightarrow |E'(3p_{3/2});\ n = 3,\ j = 3/2,\ m_j\rangle \tag{47}$$

$$|3d_{3/2};\ m_j\rangle \rightarrow |E'(3d_{3/2});\ n = 3,\ j = 3/2,\ m_j\rangle \tag{48}$$

$$|3d_{s/2};\ m_j\rangle \rightarrow |3d_{5/2};\ m_j\rangle \tag{49}$$

The perturbed states are eigenstates of n, j, and m_j only. Their energy, E', depends slightly upon their initial state when the field was zero; thus, the perturbed states have a memory of their orgin. The admixture of the neighboring ℓ state depends upon m_j through the Stark matrix element. To make actual calculations for the effect of Stark mixing, we would have to know the initial m_j populations exactly.

It is convenient to define a critical field, f_c, as the field which fully mixes a given state; that is, the field for which the percentages of different ℓ states are essentially equal. Beyond the critical field, the percentages remain constant until, ultimately, states with different j appear. For $j = 1/2$, the critical field is 58 volts/cm; for $j = 3/2$, however, f_c is only 1.9 volts/cm assuming in both cases that $j = m_j$.

It is possible to calculate the lifetime of the perturbed states as a function of field (see Appendix IV). The perturbed lifetime does

not depend upon the initial m_j state at the critical field, where it differs most from the field free lifetime of the initial state. For the critical field, the lifetime of $j = 3/2$ states is 0.786×10^{-8} sec. For the $j = 1/2$ state, the lifetime is 1.04×10^{-8} sec.

Stark Perturbed Intensities

Since f_c is so large for $j = 1/2$, we need consider only the $j = 3/2$ states. Obviously, the effect will depend upon the population of the various m_j states which are unknown; we shall assume that the distribution among the j states is statistical. To calculate the maximum effect, we can further assume $m_j = j$.

It is convenient to investigate the effects of fields in the target cell and observation chamber separately. Fields in the target cell require only a reinterpretation of the initial population factors, C_{3p} and C_{3d}. Fields in the observation chamber alter the ideal form of Equation 17.

Fields in the Target Cell. If we assume a field greater than or equal to f_c extending over the entire cell, half the intensities, $I_{3p}(X)$ and $I_{3d}(X)$, build up according to $(1 - 3^{-X/X^s_{3p,d}})$, where $X^s_{3p,d}$ is the decay length of the Stark perturbed state. If we assume the perturbing fields vanish at the termination of the cell, we can calculate the percent change in C_{3p} and C_{3d}. In Table 5 we compare the factors $(1 - e^{-L/X_{3d}})$ and $(1 - e^{-L/X^s_{3p,d}})$ for several energies. Since L is greater than X_{3p}, X_{3d}, and $X^s_{3p,d}$, the changes in C_{3p} and C_{3d} are small.

Table 5. Effect of Fields in the Target Cell

Energy (keV)	$(1-e^{-L/X_{3p}})$	$(1-e^{-L/X_{3d}})$	$(1-e^{-L/X^{s}_{3p,d}})$	Percent Change In C_{3p}	Percent Change In C_{3d}
75	.999148	.910115	.99052	-0.43	+ 4.40
150	.99325	.91799	.96291	-1.53	+ 8.86
250	.97918	.73280	.92208	-2.92	+12.91
350	.96209	.67225	.88434	-4.04	+15.77

The errors given in this table can be considered as maximum errors since they are calculated for the worst possible case.

Fields in the Observation Region. Fields in the observation region result in more severe difficulties since the ideal form if I(X) is altered. Using the techniques described in Chapter II, we may investigate the effects of the perturbed states on the deconvolution procedure.

Table 6 summarizes the predicted effect of fields in the observation region. Here, we continue to employ our initial assumptions of the populations of j and m_j. Further, we again use a typical set of measurement positions, (X_i). The percent deviation between the ideal intensity, I(X), and the perturbed intensity, I'(X), is generally very small. For example, at 150 keV energy the maximum deviation occurs around X = 9 cm and is only about two percent. Table 6 gives the percent deviation between the deconvolved population factors, C''_{3p} and C''_{3d}, and the ideal population factors, C_{3p} and C_{3d} for several energies; these ideal factors are representative of a nitrogen target.

Table 6. Effect of Stark Mixing of the $3p_{3/2}$ and $3d_{3/2}$ upon the determination of C_{3p} and C_{3d} population factors.

Energy (keV)	ΔC_{3p}	ΔC_{3d}	ΔR_{3p}	ΔR_{3d}
75	+23.3	-13.3	+24.2	-12.7
100	+22.0	-12.81	+22.9	-12.2
125	+21.2	-12.6	+22.0	-12.0
150	+20.6	-12.5	+21.4	-11.9
200	+19.5	-12.1	+20.3	-11.5
250	+18.4	-11.5	+19.2	-11.0
300	+17.4	-10.8	+18.2	-10.2
350	+16.3	- 9.98	+17.2	- 9.32
400	+15.4	- 9.13	+16.3	- 8.4

Here, ΔC_{3p}, ΔC_{3d}, ΔR_{3p} and ΔR_{3s} have the same meaning as in Chapter II, $\Delta C_{3\ell}$ is the percent change in the coefficient, $C_{3\ell}$, and $\Delta R_{3\ell}$ is the percent change in the ratio, $C_{3\ell}/C_{3s}$.

Possibility of Stray Fields

Some care was taken to avoid the possibility of stray fields in the region of the beam. For example, the beam axis was located as far as possible from the window in the observation chamber since it is always possible for charges to accumulate on insulators near the beam. Furthermore, the cell and observation chamber were constructed to avoid exposing the beam to contact potentials. Fields in the region of the Faraday cup were shielded from the flight path of the beam.

Motionally induced fields can arise from magnetic fields with vector components transverse to the beam axis. This can pose a significant problem at these high energies since the induced field is proportional to velocity.

Stray magnetic fields were avoided by using non-magnetic materials in the region of the beam. Unfortunately, the terrestial field could not be shielded out over the entire excitation and observation region; it, therefore, made a significant contribution to the spurious motionally induced field.

The total motionally induced field may, in fact, exceed the critical field for $j = 3/2$ at energies as low as 75 keV. However, our experimental test indicate that if non-colinear magnetic fields accompany the perturbing electric field, the Stark effect is reduced somewhat.

Hughes also attempted to verify this fact but his test were inconclusive[2].

Experimental Assessment of the Effect of Fields

Since exact calculations were not possible for the effects of stray fields upon the intensity, I(X), an experimental investigation of these phenomena was undertaken. It was found that the errors suggested by the

calculations of Tables 5 and 6 were, in all probability, overestimates.

Experimental Technique. Special electrodes were introduced into the observation chamber in order to expose the beam to various types of electric fields. One set of electrodes consisted of two parallel plates extending over the region in which the p and d states decay. These plates were separated by 4.3 cm. and provided a gross field transverse to the beam. A second electrode configuration provided a longitudinal field in the region of the decay of the p state (from X = 0 to X = 4.5 cm). It was possible to terminate this field abruptly at either X = 0 or X = 4.5 cm.

In order to observe subtle differences in the perturbed decay, special modifications were made to the data control system. It was made possible to alternate the data acquisition cycles with either a zero positive or negative voltage applied to the plate system in the observation chamber. Thus, it was possible to alternately observe the intensity, I(X), under three field conditions at each point X a number of times; a single scan, therefore, yielded three complete scans for each field condition. The sequence of field configurations could be changed from point to point as additional insurance against systematic errors. The format of the program was recorded by an encoding parameter taking the place of the elapsed time parameter, ENC, mentioned earlier. This parameter allowed the computer to automatically separate the data for the three field configurations and perform three deconvolutions.

The experiments were made more practical by using H_2^+ projectiles for a source of excited hydrogen; the dissociation reaction for H_2^+ yields intensity functions rich in p and d state emission.

Conclusion. In general, the full effects of Stark mixing were not realized. Since rather large fields were employed (greater than 30 volts per cm.), this behavior cannot be explained by assuming that the preponderance of the $3p_{3/2}$ and $3d_{3/2}$ atoms are formed in the $m_j=1/2$ substrate. However, it could be explained by assuming that most of the p state is $j = 1/2$ and most of the d is $j = 5/2$. If this very unusual condition prevailed, our experimental test would be rather meaningless insofar as they assess the effects of fields on the decay of p and d states produced by charge transfer. To test this hypothesis, very large fields were applied (>58 volts per cm.); again, very little effect was observed.

Most likely, these observations can be explained by the effects of accompanying magnetic fields. At any rate, these experiments provide strong evidence that stray fields have little effect on the decay of the p and d states even if they exceed the critical field.

It would be very interesting to observe the effects of fields of sufficient strength to mix the different j states. Unfortunately, such fields are on the order of 500 volts per cm. The plate system employed in this measurement could not handle the required voltages.(>2 kilovolts).

The Quantitative Measurement of Beam Emission

As mentioned earlier, the determination of the 3s., 3p, and 3d state populations requires a knowledge of the intensity function, I(X), which is defined as the total number of Balmer alpha photons emitted per second per unit length of beam. The quantitative measurement of I(X) is actually made in terms of S(X), the number of photons detected per second at position X. The relationship between I(X) and S(X) is dependent upon the

characteristics of the detector and the nature of the emitted Balmer alpha radiation. In determining this relationship, it is convenient to isolate three basic problems:

1. Photon signals measured at a position X are due to the detection of emanations from a finite beam region about X, $\{[X - \Delta/2, X + \Delta/2]; Z^2 + Y^2 = R^2\}$, rather than a point. Obviously, one must determine the dimensions of this region, Δ (the length), and R (the beam radius), in order to integrate I(X). Further, it may be that photons emitted from different points within the region are detected with different efficiencies.

2. The radiation emitted from a given point within the observation region may exhibit some inherent anisotropy. In this experiment, there are two distinct aspects to this problem. One, there exists the possibility of a particular angular distribution of the 3p and 3d state radiation due to polarization. Two, because the radiating hydrogen atoms in the beam have relatively high velocities, all λ_α radiation from the beam displays an angular and velocity dependent Doppler shift.

3. Finally, the determination of the absolute efficiency of the photon detector must be made. This requires the establishment of an absolute emission standard and its interpretation in terms of beam emission.

In this section, the three problematic areas defined above are treated in four subsections. The first deals with the interpretation of radiation from a finite observation region. The next two are concerned with the anisotropic effects of polarization and the Doppler shift. The last subsection describes the absolute calibration of the photon detection system.

Finite Dimensions of the Observation Region

The finite dimensions of the observed portion of the beam introduces several possible sources of systematic error. Theoretically, these errors can be made arbitrarily small by reducing the size of the observed portion of the beam; in practice, however, one is ultimately limited by the requirement of sufficient signal strengths.

As defined previously, the longitudinal dimension of the beam is described by the coordinate X. Y and Z describe the transverse dimensions with Y perpendicular to the photon detector axis defined by Z.

The transverse dimensions of the beam can be estimated from the configuration of the beam collimators and the magnitude of the scattered currents in the target cell and observation chamber by assuming a symmetric excited projectile current density $J^{3n}(X, \sqrt{Y^2 + Z^2})$ with mean radius $\bar{A}(X)$. The transverse beam dimensions $\bar{A}_Y(X)$ and $\bar{A}_Z(X)$ are then simply assumed to be $\bar{A}(X)$. As will be pointed out, the smallness of the upper bounds that can be confidently placed upon $\bar{A}(X)$ suggest that we need not really be too concerned about the actual cross sectional structure of the beam.

Transverse Dimensions of the Beam. The transverse dimensions of the beam are rather small in comparison to the beam to detector distance, d. This distance, d, is measured from the observation point (defined by the intersection of the beam line and detector axis Z) to the front face of the first lens and is roughly 12 cm. $\bar{A}(X)$ is sharply defined at X = 0 and is about .08 cm. Near the entrance to the Faraday cup (X $\sim$65 cm.), the beam is more diffuse; but, from scattered current measurements, it is certain that $\bar{A}(X)$ is much less than 0.4 cm.

It is convenient to discuss the problem of the transverse extent

of the beam in terms of the separate effects due to the Y and Z dimensions. Before proceeding, however, it is necessary to describe the optical stop which defines the observation region. This stop consists of a flat black plate with a centered rectangular aperture which is pressed firmly against the end of the photomultiplier tube. The width of the rectangle, 0.6 cm., defines the X dimension of the observation region, Δ. The length, which extends over nearly the entire vertical diameter of the tube, poses essentially no constraint on the detection of emission along the Y axis of the beam.

Since $\bar{A}_Z(X)$ is finite, the observed segment of the beam is not perfectly focused. Furthermore, this condition is a function of position X. From the estimated range of $\bar{A}_Z(X)/d$, .007 to .03, it is, however, not likely that the correction due to $\bar{A}_Z(X)$ is significant.

Theoretically, the construction of the optical stop eliminates the need for a correction due to $\bar{A}_Y(X)$. One needs, however, to consider the possible variation of sensitivity over the face of the photomultiplier tube. For the tube used in this experiment, the sensitivity had been mapped over the area exposed to the beam. No variations greater than 5 percent were found.

Longitudinal Dimension of the Beam. The determination of the longitudinal extent of the observation region is certainly the most important consideration. Here we are faced with three complications: the variation in detection sensitivity over the Δ region, the extent to which the optical system defines a Δ segment of beam in terms of the optical stop's aperture width, and variation of the beam emission, I(X), over the interval $\{X - \Delta/2, X + \Delta/2\}$.

As mentioned previously, only small variations in the sensitivity were found across the face of the photomultiplier. The orientation of the tube was, in fact, adjusted to further minimize any variations in the X direction. It is also unlikely that additional variations arose from the transmission of the interference filter; some care was exercised to insure that the surfaces of the filter were uniformly clean.

The segment of beam viewed is not perfectly defined by the aperture width. Monochromatic aberrations and small internal reflections tend to slightly obscure the boundary of the observation region. The magnitude of these effects was assessed by placing a small light source (less than 1/4 mm. diameter) on the beam line and then scanning across the source; the ideal signal profile very nearly approximated a 6 mm. wide stepfunction. The actual signal profile indicated that some small effects did, in fact, exist but they were not sufficient to introduce an appreciable error. In addition to the obscurity of the observation region, there is also a small magnification factor introduced by the two lenses. This results in about a 1 percent loss in signal which is taken into account by the procedure for the overall calibration of the detector.

Finally, the variation of the emission function, I(X), over the observation region must be considered. Obviously, this effect is different for each component emission function, $I_{3s}(X)$, $I_{3p}(X)$, and $I_{3d}(X)$ since each component has a different derivative with respect to X. For a small enough observation region, the total integrated emission about X is simply $\Delta I(X)$; otherwise, each component emission function must be integrated separately. Since we assume that each function, $I_{3K}(X)$ is a pure exponential of the form $C_{3K} e^{-X/X_{3K}}$, the integration can be done exactly giving

a total integrated emission about X of X_{3K} Sin h $(\Delta/X_{3K})\cdot I_{3K}(X)$. As Δ/X_{3K} goes to zero, the hyperbolic sine rapidly converges to its argument; thus, $\Delta I(X)$ is generally a very good approximation. For cases where the decay length is not much larger than Δ, one must be careful to use the exact integration. This is the case for p states at low energy, for charge exchange and for p and d states produced by the dissociation of the more massive H_2^+ projectile.

Anisotropy Due to Polarization

In the determination of the cross sections for forming the 3s, 3p, and 3d states, it has been assumed that the number of photons detected per second from the decay of excited hydrogen atoms in the observation region is proportional to $\langle I\rangle\Omega_c/4\pi$ where Ω_c is the solid angle subtended by the detector and $\langle I\rangle$ is the total emission. Since $\langle I\rangle$ can be resolved into each ℓ component, we have the following relation for $Q_{n\ell}$:

$$Q_{n\ell} \propto \frac{\Omega_c}{4\pi} \langle I_{n\ell}\rangle \tag{50}$$

This assumption requires that the radiation from the decay of the states is isotropic. In this section, we shall discuss the validity of this assumption in light of the possible anisotropic effects due to polarization.

Emission Intensity. The Balmer alpha emission from the beam can be thought of as arising from an ensemble of electric dipole oscillators with polarization vectors oriented along the X, Y, and Z axes. We can ascribe an emission intensity per unit solid angle, I_X, I_Y, and I_Z, for each polarization orientation. The composite intensity function, I, can be written in terms of I_X, I_Y, and I_Z by recalling that for dipole radiation

the intensity at an angle θ with respect to the polarization vector axis is proportional to $\sin^2\theta$:

$$I = \sum_i I_i \sin^2 \theta_i \tag{51}$$

Here, θ_i is the angle the direction of observation makes with respect to the i^{th} axis. If we now choose a polarization axis about which the angular distribution of the radiation is measured, I can be characterized by two polar coordinates, θ and Φ, defined by the relations:

$$\cos \theta_x = \sin\theta \cos\Phi \tag{52}$$

$$\cos \theta_y = \sin\theta \sin\Phi \tag{53}$$

$$\theta_z = \theta \tag{54}$$

The total emission, $\langle I \rangle$ is obtained by integrating I over all space:

$$\langle I \rangle = \int_0^{2\pi} \int_0^{\pi} I \sin\theta \, d\theta \, d\Phi \tag{55}$$

Polarization Fraction and Anistropy. Neglecting the effects of any external magnetic or electric fields, we can assume that the polarization of the beam depends strictly upon the dynamics of the charge transfer process. Thus, the direction of the beam constitutes the only physically unique axis which we take to be the axis of polarization, X. By making use of the fact the collision process possesses an innate symmetry about X, it is possible to characterize the entire radiation distribution $I(\theta, \Phi)$ in terms of only one parameter, the polarization fraction. This parameter

can be simply defined along any axis perpendicular to X:

$$\underline{P} = \frac{I_{\parallel} - I_{\perp}}{I_{\parallel} - I_{\perp}} \tag{56}$$

$I_{\parallel}$ and $I_{\perp}$ are the intensities of radiation observed with electric vectors parallel and perpendicular to the X axis. Obviously, $I_{\parallel}$ is equal to I_X and from symmetry we have:

$$I_{\perp} = I_y = I_z \tag{57}$$

$\langle I \rangle$ and $I(\theta, \phi = \frac{\pi}{2})$ can now be expressed in terms of $I_{\parallel}$, $I_{\perp}$, and $\underline{P}$:

$$I(\theta, \phi = \tfrac{\pi}{2}) = I(\theta) = (I_{\parallel} + I_{\perp})(1 - \underline{P} \cos^2 \theta) \tag{58}$$

$$\langle I \rangle = 4\pi(I_{\parallel} + I_{\perp})(1 - \tfrac{1}{3}\underline{P}) \tag{59}$$

The anistropy of the radiation is completely described by the ratio of $I(\theta)$ to $\langle I \rangle$, which is solely a function of $\underline{P}$.

Experimental Determination of $\underline{P}$. By employing a polarization sensitive detector, it would, theoretically, be possible to measure the ratio:

$$r = I_{\perp}/I_{\parallel} \tag{60}$$

The polarization fraction would then be $(1 - r)/(1 + r)$. As we shall point out later, s-state radiation is unpolarized; we need consider only the effect due to the p and d radiation, which can be characterized by two component polarization fractions, $\underline{P}_{3p}$ and $\underline{P}_{3d}$. Since the p and d character of the emission vanishes with increasing X, the total polarization fraction, $\underline{P}(X)$, is a function of position:

$$\underline{P}(X) = \frac{\underline{P}_{3p} C'_{3p} e^{-X/X_{3p}}}{I(X)} \quad \frac{\underline{P}_{3d} C'_{3d} e^{-X/X_{3d}}}{I(X)} \tag{61}$$

with

$$I(X) - C_{3d} e^{-X/X_{3s}} + C_{3p} e^{-X/X_{3p}} + C_{3d} e^{-X/X_{3d}} \tag{62}$$

Here, C'_{3p} and C'_{3d} are the observed populations corrected for the inherent anisotropy due to $\underline{P}_{3p}$ and $\underline{P}_{3d}$. By making the approximations, $C'_{3p} = C_{3p}$ and $C'_{3d} = C_{3d}$, the parameters, $\underline{P}_{3p}$ and $\underline{P}_{3d}$ could, in principle, be deduced from two measurements of $\underline{P}(X)$ using previous determinations of C_{3s}, C_{3p}, and C_{3d}. In practice, we find that $C_{3s} > C_{3p} > C_{3d}$; this is a very unfavorable situation for the measurement and resolution of $\underline{P}_{3p}$ and $\underline{P}_{3d}$.

Using special counting techniques, it might be possible to measure $\underline{P}(X)$. For example, by continuously alternating the preference of the photon detector to $\perp$ and $\parallel$ polarized radiation and by accumulating the $\perp$ and $\parallel$ signals, $S_{\perp}(X)$ and $S_{\parallel}(X)$, in separate channels, one could calculate $\underline{P}(X)$ from $S_{\parallel}(X) - S_{\perp}(X)$. Because of low signal strengths, many alternate measurements would be required to obtain a statistically significant difference between $S_{\perp}(X)$ and $S_{\parallel}(X)$. In addition, the alternation time would have to be sufficiently short to avoid the effect of changes in pressure, beam current, and detection efficiency. With the present experimental apparatus, such measurements were not feasible.

Unfortunately, there is little direct experimental information about the polarization of radiation from neutralized protons. Hughes, Doughty, and Filippell[2] have measured $\underline{P}_{3p}$ and $\underline{P}_{3d}$ for charge transfer from nitrogen targets in the energy range 10 - 35 keV. $\underline{P}_{3p}$ appeared to be zero at the higher energies, but the measurement was of doubtful accuracy. $\underline{P}_{3d}$

appeared to maximize at 15 keV and then decrease steadily with increasing energy, always falling below a value of 0.3. Andreev, Arkudinov, Bobashev, and Matveev[5] have measured the total (3p + 3d) H_α polarization of emission from hydrogen produced by the neutralization of protons by argon in the 10 - 30 keV energy range. In addition they have measured the polarization of the accompanying L_α radiation. Gaily, Jaecks, and Geballe[25] measured the angular distribution of L_α radiation arising from the neutralization of both protons and deuterons by Noble gas targets for energies between 0.5 - 20 keV. Recently, Teubner, Kappila, Fite, and Girnius[26] measured the L_α polarization fraction for protons onto helium, neon, and argon at energies less than 30 keV. Their measurements were not in complete agreement with Gaily et al.

Maximum Error Due to Polarization. Although it is not possible to calculate the error due to polarization, the theoretical treatment of polarized emission does suggest well defined limits for $\underline{P}_{3p}$ and $\underline{P}_{3d}$. A discussion of this theory is outlined in Appendix III. It suggest limits of +0.421 to -.267 for $\underline{P}_{3p}$ and +0.479 to -0.315 for $\underline{P}_{3d}$.

Correction for Q_{3p} and Q_{3d}. Neglecting the finite angle subtended by the photon detector and the possibility of any polarization dependent features of the optical system, the correction for $Q_{3\ell}$ can be obtained by writing $\langle I \rangle$ in terms of $I(\frac{\pi}{2})$; further, $I(\theta)$ can be obtained from Equations 60 and 61 in terms of $\langle I \rangle$:

$$Q_{n\ell} \propto \Omega_c I(\theta) = \frac{\Omega_c \langle I \rangle}{4\pi} \frac{1}{(1 - \frac{1}{3}\underline{P})} \tag{63}$$

Hence, the actual cross section contains a factor of $(1 - \frac{1}{3}\underline{P})^{-1}$ which we must divide out to obtain the ideal cross section of relation:

$$Q_{n\ell} = \frac{(3 - P)}{3} Q_{n\ell} \text{ (measured)} \tag{64}$$

Using the limits for $\underline{P}_{3p}$ and $\underline{P}_{3d}$, we can now find the range of error of $Q_{n\ell}$ associated with anistropy due to the polarization of emission. For Q_{3p}, the maximum possible error is -14 to +9 percent. For Q_{3d}, the errors are slightly larger, -16 to +11 percent.

Doppler Effects

The observation of radiation from moving atomic systems can be complicated by the Doppler effect at sufficiently high velocities. Classically, one expects the wavelength observed along a direction at an angle θ with respect to the velocity, $\vec{v}$, to be given by the following simple relation providing the point of observation is many wavelengths away from the source of the radiation:

$$\lambda = \lambda_o(1 - \frac{v}{c} \cos\theta) \tag{65}$$

Here, λ_o is the observed wavelength when the observer is at rest with respect to the radiating system.

The Relativistic Doppler Shift. The derivation of this relation assumes that an observer in the laboratory frame of reference would observe natural processes evolving in time at the same rate as an observer in the rest frame of the moving system. To the contrary relativity predicts that the observer in the laboratory frame sees all processes in the rest frame of the moving system slowed by virtue of the relativistic time transformation:

$$t_{LAB} = \left(\sqrt{1 - v^2/c^2}\right)t \tag{66}$$

This time dilation is then reflected in the laboratory frame by the observation of radiation increased in wavelength by a factor of $(1 - v^2/c^2)^{-\frac{1}{2}}$. Hence, the complete--relativistic--Doppler shift relation if given by:

$$\lambda = \frac{\lambda_o(1 - v/c \cos \theta)}{\sqrt{1 - v^2/c^2}} \tag{67}$$

Observations made on a perpendicular axis, $\theta = 90°$, to the velocity, $\vec{v}$, are affected solely by time dilation. This can amount to a positive shift of 2.4 Angstroms for Balmer alpha radiation at a velocity representative of a 350 keV proton. This can be compared to the classical shift of 37.3 Angstroms just 12 degrees off the perpendicular axis of observation.

Correction for Doppler Shift. Figure 14 shows the shift in wavelength of the Balmer alpha line for various velocities and equivalent proton energies as a function of θ for the range of angles appropriate to the acceptance cone of the optical system, $\theta^+ = 78$ to $\theta^- = 102$ degrees. For these shifts in wavelength, there are appreciable changes in the transmission of the optical system due to narrow pass band of the interference filters employed to isolate the Balmer alpha line. Therefore, the overall photon detection efficiency is a function of incident proton energy. At a particular energy, however, the separation of the three states is unaffected since the Doppler shift is essentially the same for each component of the Balmer alpha line.

The correction for this energy dependent efficiency can be obtained in a very straightforward manner. Consider the radiation entering the acceptance cone through an infinitesimal solid angle segment dw defined by an infinitesimal angular interval dw about θ. This radiation produces a signal ds proportional to dw which can be expressed as:

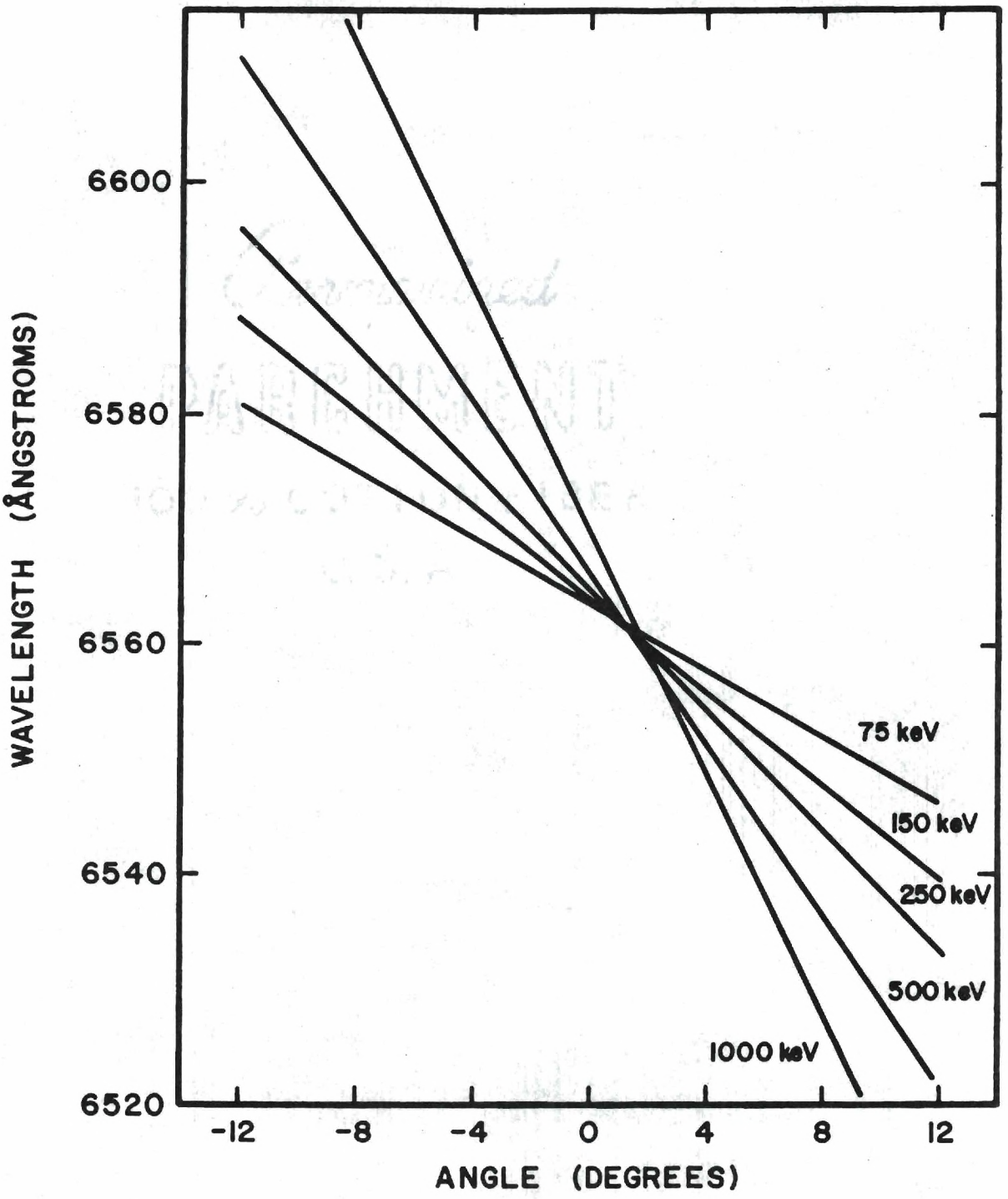

Figure 14. Wavelength of Observed H_α Emissions as a Function of Angle about a Perpendicular Axis to the Beam Direction.

$$ds = \epsilon T^S(\theta)\ T^F(\lambda(\theta,v))\ Q(\lambda(\theta,v))\ I(\theta)d\theta \tag{68}$$

Here, $T^S(\theta)$ represents the transmission of the optical system to radiation impinging at an angle θ. $T^S(\theta)$ contains the inherent dependence of dw upon θ and is assumed to be independent of the particular filter used. $T^F(\lambda(\theta))$ is the transmission of the filter for radiation of wavelength $\lambda(\theta)$. $Q(\lambda(\theta))$ is the quantum efficiency of the photomultiplier detector. $I(\theta)$ is the density of radiation emitted between θ and $\theta + d\theta$. Since we neglect anisotropic effects such as polarization, $I(\theta)$ can be considered a constant representing the emissitivity of the beam, which, of course, is implicitly dependent upon beam velocity through the cross section. Finally, ϵ represents the detection efficiency for pluses received from the photomultiplier tube. This quantity is determined by the counting electronics and the optimization of the signal to noise ratio as described in a previous chapter. Integrating θ over the acceptance cone, one obtains the total signal:

$$S(v) = I(v(E))\epsilon \int_{\theta-}^{\theta+} T^S(\theta)\ T^F(\lambda(\theta,v))\ Q(\lambda(\theta,v))d\theta \tag{69}$$

Taking the limit $V \rightarrow 0$ of the integral, the expression for S(V) reduces to:

$$S(v \rightarrow 0) = I(v(E))\epsilon\ \ T_0^S\ T^F(\lambda_\alpha)\ Q(\lambda_\alpha) \tag{70}$$

where T_0^S is the total transmission of optical system. $T^F(\lambda_\alpha)$ is the transmission of the filter to Balmer alpha radiation, and $Q(\lambda_\alpha)$ is the corresponding quantum efficiency. Obviously, it is convenient to write the functions $T^S(\theta)$, $T^F(\lambda(\theta,v))$, and $Q(\lambda(\theta,v))$ in the following way:

$$T^S(\theta) = T_0{}^S\, t^S(\theta) \tag{71}$$

$$T^F(\lambda(\theta,v)) = T^F(\lambda_\alpha)\; t^F(\lambda(\theta,v)) \tag{72}$$

$$Q(\lambda(\theta,v)) = Q(\lambda_\alpha)\; q(\lambda(\theta,v)) \tag{73}$$

Now, it is possible to write S(v) in terms of a beam velocity dependent "Doppler efficiency":

$$S(v) = \epsilon I(v(E))T_0{}^S\; T^F(\lambda_\alpha)Q(\lambda_\alpha) \int_{\theta-}^{\theta+} t^S(\theta)t^F(\lambda(\theta,v))q(\lambda(\theta,v))d\theta \tag{74}$$

$$S(v) = S(v \to 0) \int_{\theta-}^{\theta+} t^S(\theta)\; t^F(\lambda(\theta,v))q(\lambda(\theta,v)) = S(v \to 0)D(v) \tag{75}$$

D(v) can be determined by approximating its integral representation by a finite sum:

$$D(v) = \sum_K t^S{}_K(\theta_K)t^F(\lambda(\theta_K,v))q(\lambda(\theta_K,v)) \tag{76}$$

Measurement of Filter Transmissions. The filter transmission $t^F(\lambda)$ from which D(V) is calculated was determined for the two filters employed in this experiment by using the tungsten lamp and spectrometer described in the section on absolute calibration. The monochromator's wavelength scale was calibrated at the Balmer alpha wavelength using a hydrogen discharge lamp. Figure 15 shows the transmission curves obtained. Filter 1 has a full width at half maximum of 13.2A. Filter 2 is much wider with a width of 30.8 Å.

Determination of Relative Quantum Efficiency. The relative quantum efficiency, q(λ), for the 9558 EMI photomultiplier tube was estimated from

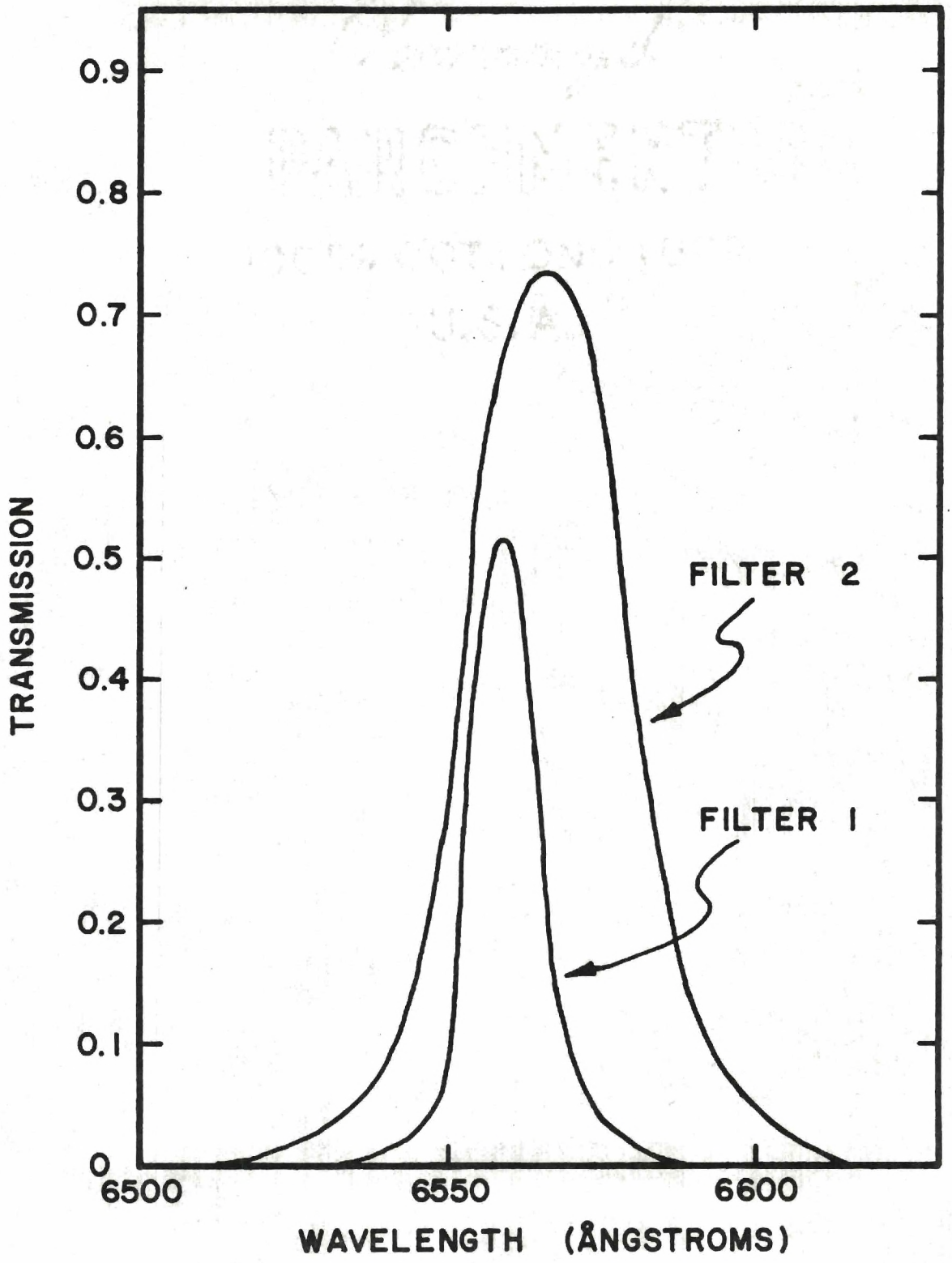

Figure 15. Transmission of Interference Filters as a Function of Wavelength.

the published spectral response data of the manufacturer. The total change in $q(\lambda)$ over the entire range of λ never exceeds 10 percent in the calculations for $D(\nu)$.

Determination of Optical Transmission. $t^S_K(\theta_K)$ can be defined by dividing the acceptance cone into a finite number of segments represented by symmetrically placed imaginary vertical chords on the first circular aperture of the optical system defined by the mount for the first lens. This is shown in Figure 16. The radiation impinging anywhere in the K^{th} segment is assumed to have wavelength $\lambda(\theta_K)$ where θ_K is the acceptance angle defined by any point on a vertical besector of the segment. Over a sufficiently small range of wavelengths, the average transmission of the filter is simply porportional to the average wavelength. The average wavelength (defined in terms of the integral of $\cos(\theta)$ over the K segment) is, in turn, approximately equal to $\lambda(\bar{\theta})$.

In defining the transmissions of the K segments, it is assumed that the segmented regions defined on the front line of Lens 1 represent the regions defined by intersection of the circular aperture lying in a plane perpendicular to the optical axis and the constant θ radiation cones. Actually, these intersections are hyperbolae which are increasingly more eccentric as one moves away from the optical axis. Because of the relatively large distance between the aperture and beam line, one can, in fact, treat the bounding chords as lines of constant θ.

For each K segment, θ_K is calculated from the center of the observation region; i.e., the intersection of the optical axis and beam line. Actually, light is received in any K segment from all points in the observation region $X - \frac{\Delta}{2}$ to $X + \frac{\Delta}{2}$. Light originating at points other than the

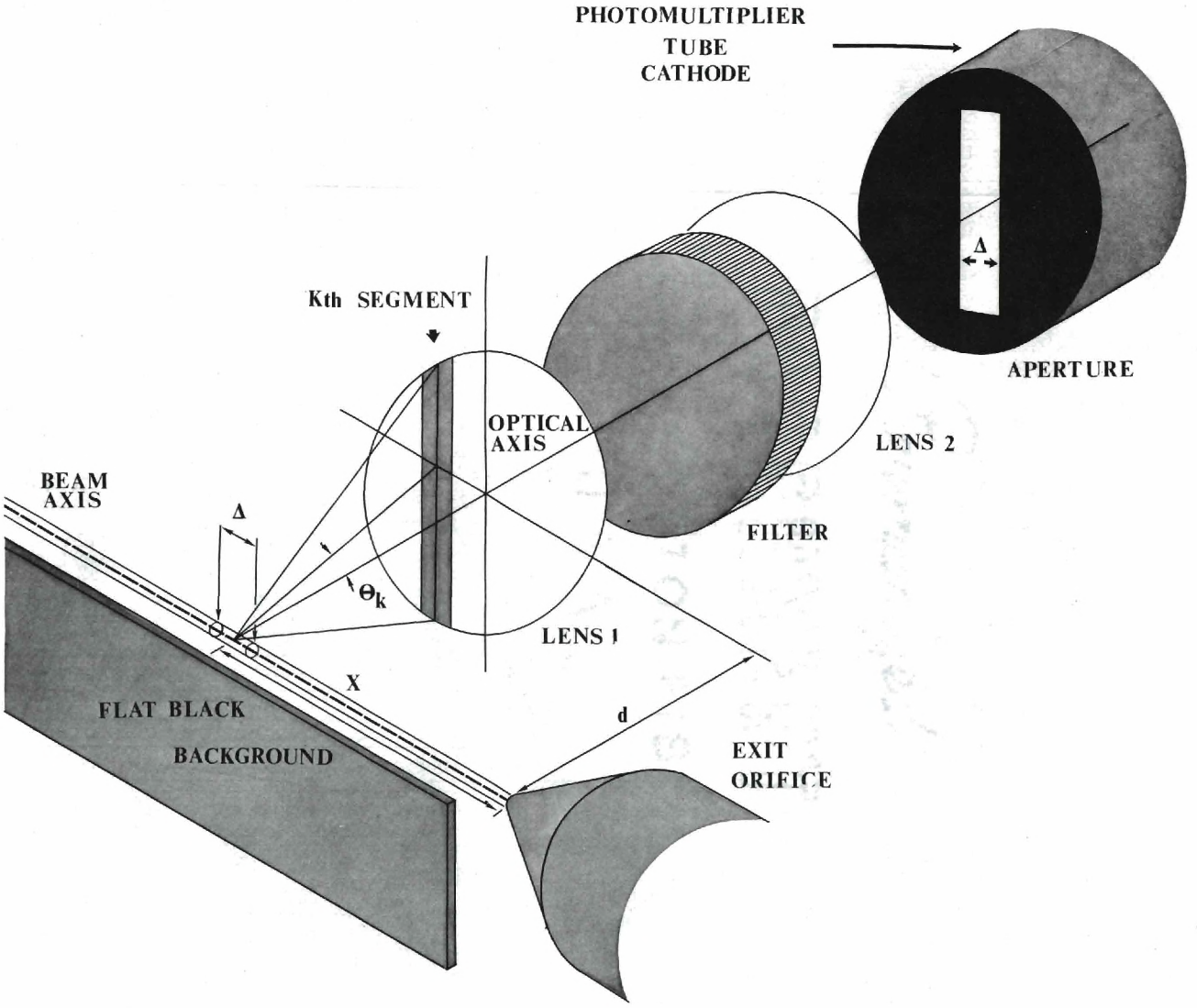

Figure 16. Diagram of Optical System.

center of the observation region will impinge at angles other than θ_K. Ideally, one would define θ_K as a function of position, $\theta_K(X)$. Then the entire Doppler correction could be integrated over the interval $[X - \frac{\Delta}{2}, X + \frac{\Delta}{2}]$. In practice, it would appear that very little accuracy would be gained by this additional effort. Corrections due to the transverse dimensions of the beam are even less significant than those due to the longitudinal dimension, Δ.

Two procedures were employed to determine $t_K(\theta_K)$. In the first (Procedure 1) $t_K(\theta_K)$ was evaluated, experimentally, for eleven values of K. In Procedure 2, $t_K(\theta_K)$ was calculated geometrically; thus, it was possible to integrate Equation 75 numerically.

Procedure 1. The transmission of each K segment, $t_K(\theta_K)$, was measured separately using three different filters. First, the two Balmer alpha filters were used to observe 6562.8 Å radiation from the dissociation-excitation of molecular hydrogen by high energy proton beam. Secondly, a 4439 Å filter was used to observe a helium target excitation line. Both measurements gave very nearly the same values of $t_K(\theta_K)$.

Experimentally, the K segments were defined by optical stops inserted between the lens and filter. This was done to facilitate the rapid change from one segment to another in order to provide the best determination of relative transmission. This procedure introduces some inherent errors. The constant θ chords defined in front of Lens 1 are not optically projected onto the filter as perfectly straight lines, but rather as nearly straight parabolas. The deviation from a straight line depends upon the departure of Lens 1 from an ideal thin lens. For the lens used, the departure is small.

Procedure 2. A computer program was devised to integrate Equation 75 numerically. $t_K(\theta_K)$ was calculated geometrically by introducing the parameter d_K which is the distance from the center of the K segment to the optical axis. Hence, $t_K(\theta_K)$ was given by the equation:

$$t_K(\theta_K) = \frac{\Delta d_K \sqrt{A^2 - d_K^2}}{\pi A^2} \tag{77}$$

Here, Δd_K is the width of K^{th} segment. A is the radius of the first optical aperture which defines the acceptance cone for receiving radiation of the observation region of the beam.

Experimental Test for Doppler Corrections. As an overall check on the determination of the Doppler efficiencies, $D_1(E(V))$ and $D_2(E(V))$ for Filters 1 and 2, the signal strengths due to 3s emission in the beam for both filters were compared at a number of energies. Figure 17 shows the comparison between the actual measured ratio of signal strengths S_2/S_1 and the ratio S_2'/S_1' predicted from $D_1(E(V))$ and $D_2(E(V))$. From Equation 74, it is obvious that the ratio S_2'/S_1' must reduce to the ratio of the transmissions of the two filters at $\lambda\alpha$ in the limit $V \to 0$:

$$\lim_{v \to 0} \frac{S_2'}{S_1'} = \frac{S_2' \ (v \to 0)}{S_1' \ (v \to 0)} = \frac{T_2^F(\lambda_\alpha)}{T_1^F(\lambda_\alpha)} \tag{78}$$

From Equation 75, it is evident that in general:

$$\frac{S_2'}{S_1'} = \frac{T_2^F D_2(V)}{T_1^F D_1(V)} \tag{79}$$

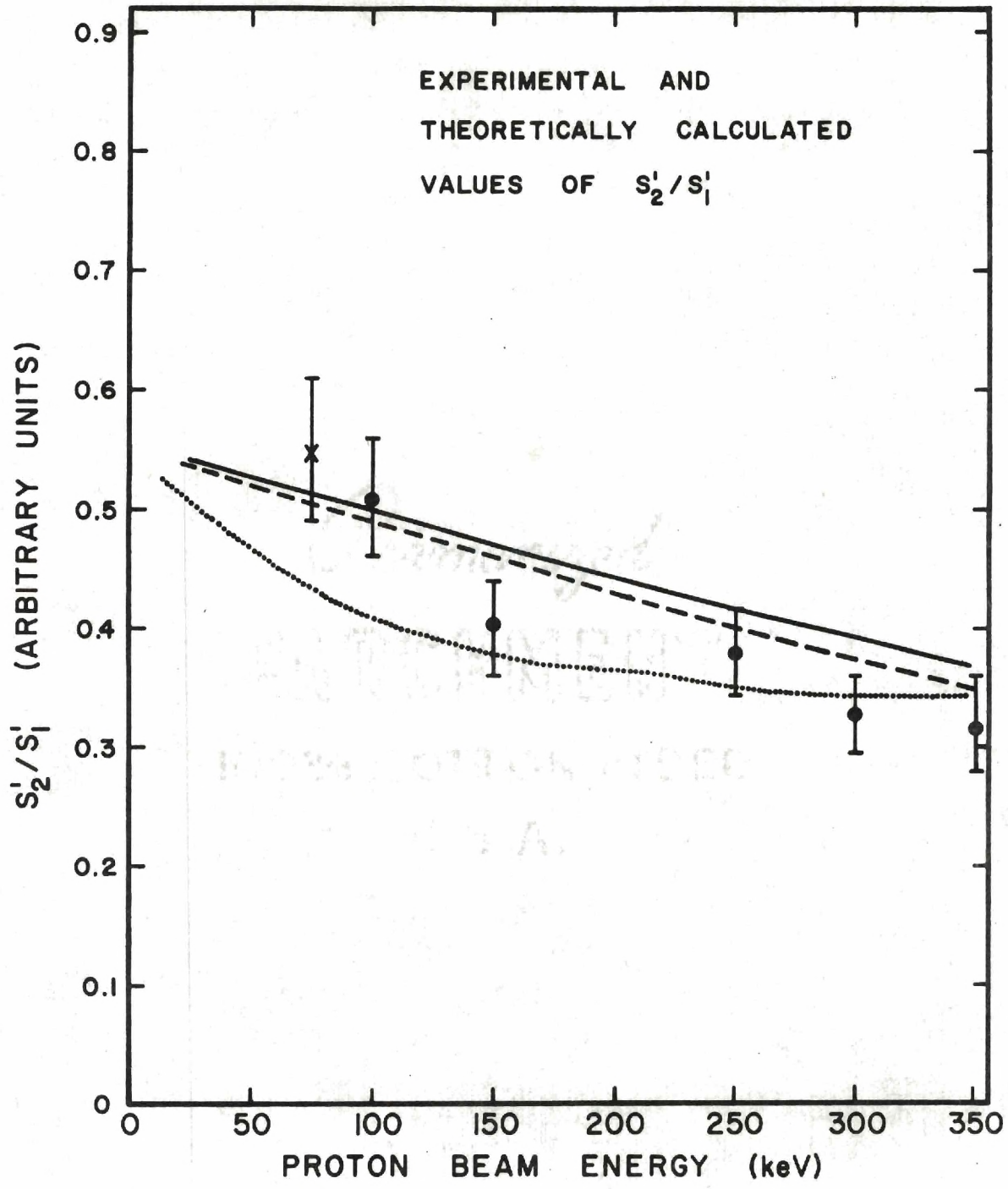

Figure 17. Experimental Verification of Doppler Corrections.

The star point represents measurements made using the dissociation H_2^+ projectiles. The solid points were determined using a nitrogen target to neutralize protons. The use H_2^+ projectiles allows for measurements over a wider range of beam velocities.

The dotted line represents the ratio of S_2'/S_1' predicted using the eleven experimentally measured $t_K(\theta_K)$ values. The dashed line represents a numerical integration for 33 segments; the solid is a numerical integration for 2000 segments. It appears that one must employ more than eleven segments to obtain a sufficiently fine integration of Equation 75 at the lower energies. (This is due to the sharpness of the transmission curve for Filter 2). A numerical integration of 3000 segments, however, does not give results significantly different for those represented by the 2000 segment integration.

The Doppler corrections $D_1(E)$ and $D_2(E)$ are rather sensitive to the symmetry of $t_K(\theta_K)$. For the numerical integration procedure, symmetry is assumed. The validity of this assumption is not completely born out by the results of Figure 17 and the experimentally measured $t_K(\theta_K)$ values.

Absolute Calibration.

The absolute calibration of the photon detection system requires first the establishment of an absolute emission standard. From this standard, secondary standard sources can be calibrated and then utilized later in the calibration procedure. The secondary standards can be designed to conform with the particular properties of the given detection system in terms of both geometry and intensity.

Standard Sources. A suitable primary absolute standard must be a source of radiation for which the power radiated in a wavelength band $d\lambda$

about λ is a precisely known function of λ. Furthermore, radiation from the source should be of known polarization. Such a radiation source can be characterized by an emission function, $E(\lambda, \theta, \Phi)$, describing the number of quanta radiated in a band $d\lambda$ about λ in a direction, $\{\theta, \Phi\}$, per steradian of solid angle per unit area of source. If the radiation were polarized, $E(\lambda, \theta, \Phi)$ could be resolved into two components.

$$E(\lambda, \theta, \Phi) = E_{\perp}(\lambda, \theta, \Phi) + E_{\parallel}(\lambda, \theta, \Phi) \tag{80}$$

Here, $E_{\perp}$ and $E_{\parallel}$ would represent the fractions of radiation with perpendicular and parallel polarization with respect to the plane defined by the direction of propagation and polarization axis.

In photometric measurements, the classical absolute standard has generally been an isothermal cavity in an incandescent blackbody. This is a particularly useful standard since $E(\lambda, \theta, \Phi)$ is described by the well known Planck function. Blackbody radiation is unpolarized and entirely determined at a particular wavelength, by the blackbody temperature. For example, the radiation power density (per unit of source area per steradian) emitted from a deep cylindrical hole in a blackbody in a direction d making an angle θ with respect to the hole's axis is given by:

$$I(\lambda) = E_B(\lambda, T) \cos\theta \, d\lambda \tag{81}$$

where

$$E_B(\lambda, T) = \frac{C_1}{\lambda^5 (e^{C_2/\lambda T} - 1)} \tag{82}$$

C_1 and C_2 are functions only of the fundamental atomic constants c, h, and k.

In practice, blackbody sources can be constructed by boring small holes into hollow opaque bodies which are then heated to incandescence. Provided attention is paid to such details as internal reflections and temperature gradients, one has a radiation standard accurately defined by Equations 81 and 82.

Since the blackbody temperature must be very uniform and rather high to obtain sufficient emission in the optical region, the blackbody enclosure and heating apparatus are generally complicated. For laboratory applications such as ours, one needs a simplified approximation to a blackbody source. In this calibration work, a tungsten ribbon filament lamp was employed.

Because of temperature limitations, blackbody sources are unsatisfactory in the UV region. In the past few years, synchrotron sources (electron storage rings) have found considerable application as UV standards. Today, they are generally regarded as well understood from a theoretical standpoint as blackbody sources. As standards in the Balmer alpha region, they may also be superior to blackbody sources for beam emission calibration work. At temperatures easily measured pyrometrically, blackbody sources are enormously intense in the Balmer alpha region--many orders of magnitude stronger than typical beam emission sources. Synchrotron sources, on the other hand, can be made much weaker at these wavelengths and hence more compatible with beam emission detection systems.

It is convenient to also establish secondary optical standard sources (calibrated at particular wavelengths in terms of the absolute primary standard). These standards can be designed to be of optimum compatibility with the detection system which is to be calibrated. In

addition, they can be used to periodically monitor the sensitivity of the detector. The general design constraints on these standards are flexibility in the range of possible geometries, proper intensity, long term stability, and freedom from the need to measure or reproduce any operational conditions (such as temperature or operating voltage). Several possible sources appeared particularly attractive for applications in this experiment. These sources can be grouped into two general categories, quantum and electroluminescent sources.

A simple quantum radiation source can be formed by combining a phosphor with a radioactive activator. Certain care is required in the selection of a phosphor-activator combination. For example, radium activated sources are generally unstable because of alpha radiation degradation of the phosphor. Beta ray activated sources, on the other hand, are usually quite stable--and in addition free from accompanying gamma ray radiation. In fact, sources using beta emitters such as tritium or Krypton 85 can be sealed in glass and made completely free from radioactive emanations. Furthermore, activators such as H^3 and Kr^{85} have long half lives (12.26 and 10.3 years, respectively).

High energy beta radiation from various radioisotopes can also be used to produce bremsstrahlung, Cherenkov, or transition radiation. (Transition radiation occurs when a charged particle traverses the interface of two distinct dielectrics.)

Electroluminescent lamps can be used to provide constant low intensity sources. Hooper and Pace[27] found such lamps to have a stable and reproducible emission at ~4900Å wavelength when operated in an overvoltage condition. These lamps were further found to be quite useful as

extended area sources.

In this work, tritium activated scintillation sources were used. These were supplied by Canrad Precision Industries and consisted of small tubes containing H^3 gas which had a phosphorescent coating on the interior walls of the tube. These sources have a very small negative temperature coefficient which constitutes no error when used in the normal range of room temperatures. They appear to be quite stable and non-sensitive to slight mechanical vibration. Unfortunately, their emissions are not particularly uniform in intensity over their surfaces; however, small segments of the tube (of order a few millimeters), with a nominally constant emission distribution, can be selected.

Calibration Procedure. The calibration procedure is essentially a three-step process. First, a selected segment of the cylindrical tritium source was calibrated against the same segment of the tungsten filament at the Balmer alpha wavelength, λ_α. The emission, $E_{TL}(\lambda_\alpha, T)$, of the tungsten filament was then determined in terms of the perfect blackbody emission $E_B(\lambda_\alpha, T)$ given by Equation 87 by measuring the filament's temperature. Secondly, from the λ_α calibration point, the tritium source emission function $E_{TR}(\lambda)$ was determined. Finally, the standard tritium source was placed in the field of view of the photomultiplier in a way that very nearly resembled an actual segment of beam. From the signal of the secondary source, the total photon detection efficiency of the system was inferred.

In order to calibrate the tritium source in terms of the tungsten filament, a special apparatus was constructed. Figure 18 shows a diagram of this apparatus and the associated electronics. The tritium source,

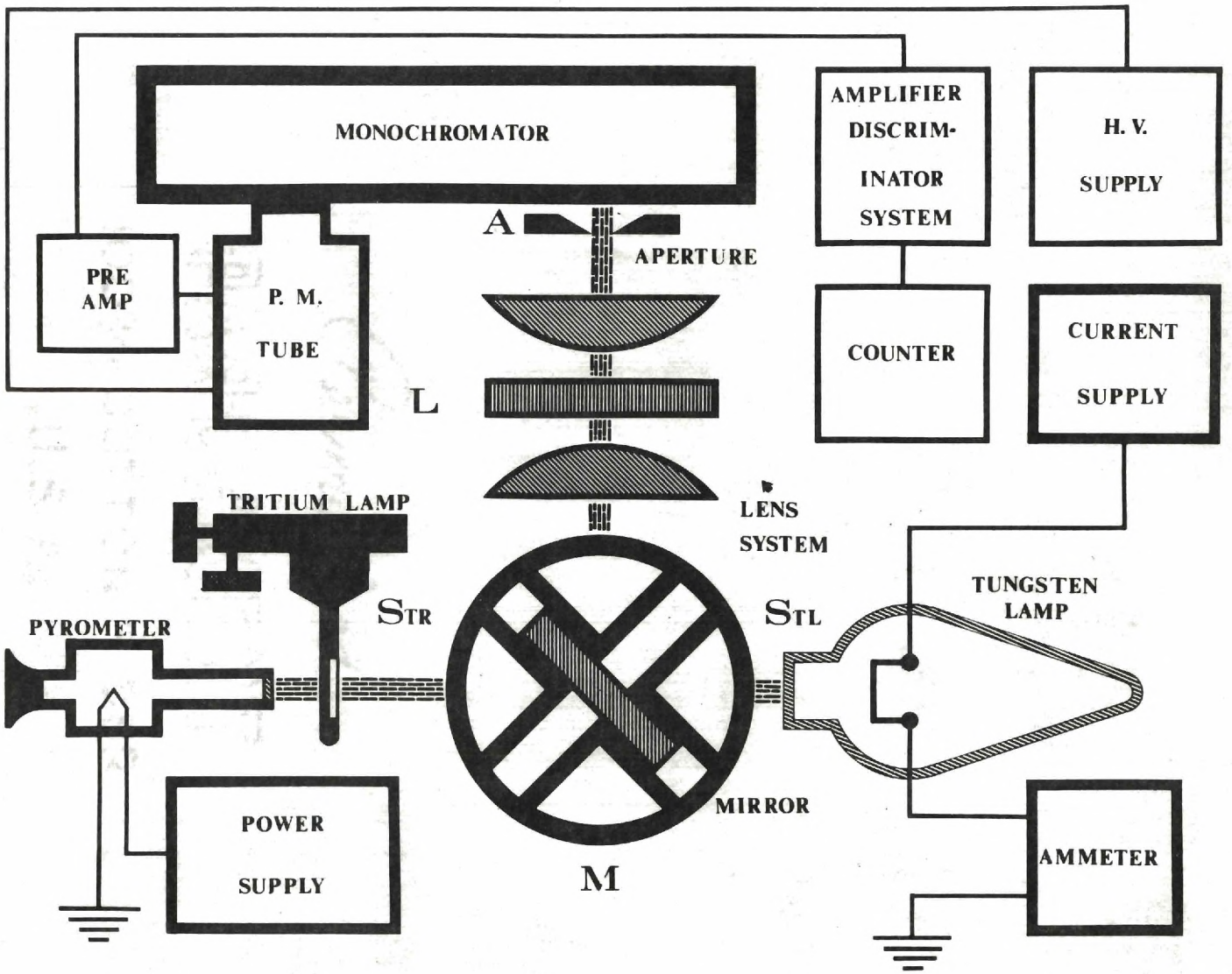

Figure 18. Diagram or Apparatus for the Calibration of the Tritium Lamp.

S_{TR} and standard lamp S_{TL} were mounted on a sturdy platform. A mirror, M, mounted halfway between these sources, could be rotated to reflect an image of either the tritium source or tungsten filament through the lens assembly L onto the entrance aperture, A, of a Jarrell-Ash 1/2 meter Ebert-Fastie monochromator; thus, the same length of source was viewed for both sources. The monochromator was fitted with an EMI 9558B photomultiplier operated in the pulse counting mode. The lens assembly L was an exact duplicate of the assembly used in the photon detection system of the main experimental apparatus; thus, the interference filters could be inserted between the two lenses and the calibration apparatus could also be used to measure filter transmissions.

Emission of Tritium Source. The first objective in the calibration procedure was to determine the absolute emission function, $E_{TR}(\lambda)$, for the tritium source over an interval $\{\lambda-,\lambda+\}$ about the Balmer alpha wavelength λ_α. Since the detected signal from either source is directly proportional to the source emission, the variation of the emission of the tritium source, $\epsilon_{TR}(\lambda)$, at wavelength λ from the emission at λ_α, $E_{TR}(\lambda)$, is equal to the ratio of the detected signal $S_{TR}(\lambda)$ to $S_{TR}(\lambda_\alpha)$.

$$E_{TR}(\lambda) = E_{TR}(\lambda_\alpha)\, \epsilon_{TR}(\lambda) \tag{83}$$

$$\epsilon_{TR}(\lambda) = S_{TR}(\lambda)/S_{TR}(\lambda_\alpha) \tag{84}$$

By measuring the ratio of the signal from the tungsten filament at λ_α, $S_{TL}(\lambda_\alpha)$, to that of tritium source, the emission of tritium can be written entirely in terms of the emission of the tungsten filament:

$$E_{TR}(\lambda) = \frac{S_{TR}(\lambda_\alpha)}{S_{TL}(\lambda_\alpha)} E_{TL}(\lambda_\alpha) \epsilon'_{TR}(\lambda) \tag{85}$$

By measuring the filament temperature, T, $E_{TR}(\lambda)$ can be expressed in terms of the fundamental Planck emission function, $E_B(\lambda,T)$ via the emissivity of the tungsten filament, $\epsilon_{TL}(\lambda,T)$:

$$E_{TR}(\lambda) = E_B(\lambda_\alpha,T)\ \epsilon_{TL}(\lambda\alpha,T)\ \frac{S_{TR}(\lambda_\alpha)}{S_{TL}(\lambda_\alpha)}\ \epsilon_{TR}(\lambda) \tag{86}$$

Emissivity of the Tungsten Filament. The emissivity, $\epsilon_{TL}(\lambda,T)$, is defined as the ratio of emission for a tungsten surface at wavelength λ to that of a blackbody at the same temperature. It should be further stipulated that the emission is normal to the surface in which case $\epsilon(\lambda T)$ is often referred to as the normal spectral emissivity.

Only normal radiation from an incandescent surface is unpolarized. This often overlooked condition of normality can lead to systematic errors in calibration measurements. In the present experiment, the radiation from the tungsten filament was however, so nearly normal to the filament surface that it was not at all likely that any possible polarization dependent features of the calibration apparatus affected comparison with the tritium source.

The emissivity function, $\epsilon_{TL}(\lambda,T)$ can have values between 0 and 1. Its dependence upon λ and T is characterized not only by the purity of tungsten but also by surface conditions which are determined largely by the manufacturing process for the filiment. The dependence of $\epsilon_{TL}(\lambda,T)$ upon is quite complicated; for a given λ, however, the dependence upon T is generally simple (nearly linear). Unfortunately, it is not possible to

calculate $\epsilon_{TL}(\lambda,T)$ from theory. $\epsilon_{TL}(\lambda,T)$ can, however, be measured directly by comparison with a blackbody or indirectly (by Kirchhoff's law) by measuring the absorptivity or reflectivity. De Vos[28] gives an accurate determination for $\epsilon_{TL}(\lambda,T)$ made by a direct comparison of a tungsten filament--very similar to the one used in this work--with a blackbody source.

Determination of Filament Temperature. The filament temperature was measured directly by use of an optical pyrometer. As pointed out by De Vos[29], such measurements constitute a determination of the brightness temperature rather than the true temperature. The brightness temperature, $T_b(\lambda)$, is defined as the temperature at which the surface emission of a radiator is equal to the emission of a blackbody at a true temperature T and wavelength λ. Using Wien's radiation law, De Vos[29] derives an equation giving $T_b(\lambda)$ in terms of T and the emissivity of tungsten; he evaluates $T^B(\lambda)$ for $\lambda = 6500$ Å. This is the same wavelength sampled by the pyrometer. Further, De Vos takes into account the transmission factor of the window used in tungsten filament lamps such as the one employed here.

In addition to the problem of the interpretation of the measured temperature, certain other precautions must be taken. For example, the segment of filament viewed was located at the center of the filament where longitudinal temperature gradients were at a minimum. Generally, longitudinal gradients are quite steep at the ends of the filament but become essentially zero over a fairly large central zone. The shape of the temperature distribution curve is symmetrical for filaments heated by A.C. currents. For D.C. currents, on the other hand, the curve is shifted a small amount in a direction depending upon the polarity. This shift

is attributed to thermoelectric effects[30].

Because of the length and construction of the filament used in this calibration, errors due to longitudinal temperature gradients were avoided.

In addition to longitudinal gradients, one need also consider the transverse variation in temperature over the width of the filament. Heated filaments display a slight inherent symmetric transverse temperature profile. For gas filled lamps, such as the one used here, there is an additional asymmetric factor. Because of convection currents, the lower portion of the filament is cooler.

In the measurement of temperature, it was not possible to distinguish transverse variations. Since the perceptual limit for distinguishing a temperature difference is about 3 - 5 K° for the pyrometer employed here, the actual transverse variations in temperature were most likely less than this limit.

Changes of 10 percent in the heater current are likely to produce corresponding changes on the order of 7 percent in the temperature. Thus, it is very important to maintain a constant current during the measurement process. The current supply depicted in Figure 18 was stabilized to within 0.05 percent. For successive measurements, the temperature was reproducible to within the perceptual limit mentioned above.

Calculated Tritium Source Emission. The tritium source was compared to the tungsten filament at four temperatures, 1354 K°, 1376 K°, 1377 K°, and 1380 K° at the Balmer alpha wavelength λ_{α}. The wavelength scale of the monochromator had been previously set to λ_{α} by observing the Balmer alpha line from a hydrogen discharge lamp. From Equation 86, $E_{TR}(\lambda)$ was

then determined using the measured values of T.

Calibration of the Detection System. By placing the tritium source in the field of view of the scanning photon detector, the overall efficiency of the detector was determined. For a detected photon count rate from the tritium source of S_{TR}, the efficiency is given by:

$$\Theta = S_{TR}/S_{TOTAL} \tag{87}$$

Here, S_{TOTAL} is the total photoemission from the tritium source. This is given directly by:

$$S_{TOTAL} = E_{TR}(\lambda_{\alpha'}) \; \langle\langle\langle\Delta\lambda\rangle\rangle\rangle \; \Delta \; 4\pi \tag{88}$$

Δ is the length of source viewed (6mm). $\langle\langle\langle\Delta\lambda\rangle\rangle\rangle$ is the effective band width averaged from the variations in the emission function, transmission of the interference filter, and detector quantum efficiency about the $\lambda\alpha$ wavelength. $\langle\langle\langle\Delta\lambda\rangle\rangle\rangle$ was calculated directly by a graphical evaluation of the integral:

$$\langle\langle\langle\Delta\lambda\rangle\rangle\rangle = \int_{\lambda^-}^{\lambda^+} \varepsilon_{TR}(\lambda) \; t^F(\lambda) q(\lambda) \lambda d \tag{89}$$

(Note that limits $\lambda-$ and $\lambda+$ were determined by the interference filter.) It should be further noted that Equation 88 is simply a convenient representation of the relation:

$$S_{TOTAL} = 4\pi \; \Delta \int_{\lambda^-}^{\lambda^+} E_{TR}(\lambda) \; \xi(\lambda) \; d\lambda \tag{90}$$

where $\xi(\lambda)$ is known dependence upon wavelength of the detector efficiency.

By adding the energy dependent Doppler efficiency factor, the total

detector efficiency is given as:

$$(E) = D(E) \frac{S_{TR}}{E_{TR}(\lambda) \langle\langle\langle \Delta\lambda \rangle\rangle\rangle \Delta 4\pi} \tag{91}$$

CHAPTER IV

SUMMARY OF DATA

In this chapter we shall summarize the data for charge transfer. It is most convenient to present the data in a format which essentially outlines the actual program of measurements. The procedure for measuring $Q_{3\ell}$ for the targets of N_2, Ar, H_2, and He was divided into four phases.

1. For each target, the cross section ratios, Q_{3p}/Q_{3s} and Q_{3d}/Q_{3s} were determined as a function of energy.

2. The ratio of each 3s state cross section, Q_{3s}, for Ar, H_2, and He to Q_{3s} for nitrogen was then measured as a function of energy. The observations of the intensity, I(X), were made at a distance of 44.92 cm from the termination of the target cell; hence, it was not possible for the p and d intensities to contribute.

3. Following these measurements, the energy dependence of the 3s state for nitrogen was carefully established. Again, observations were made at X = 44.92 cm. The data was taken using the 30 Å wide interference filter to minimize the Doppler shift correction.

4. Finally, Q_{3s} for nitrogen was measured at 150 keV energy. Immediately following this measurement, the photon detection system was calibrated against the standard tritium source. Thus, Q_{3s} for nitrogen was determined absolutely at 150 keV. From this measurement, all the absolute cross sections were calculated.

The procedure was followed to minimize the effects of long term drifts and systematic errors. The direct measurement of cross section

ratios does, in general, eliminate a number of possible experimental errors.

The data for N_2, Ar, H_2, and He is followed by a statement of the 3s state cross sections for the molecular targets: O_2, NO, CO, CO_2, CH_4, C_2H_6, C_2H_4, and C_3H_8. Again, from Q_{3s} for nitrogen, the absolute cross sections were calculated. Further, some limited data was obtained for targets of D_2 and Ne.

Data concerning the cross section for the collisional destruction of the 3s state and the production of the 3s state by the collisional excitation of neutrals is summarized in Appendix I. Included is a brief discussion of the significance and interpretation of these data.

Appendix II contains a summary of the production of 3ℓ excitation by the dissociation of H_2^+ and H_3^+ projectiles.

Finally, this chapter is concluded with a summary and review of the more significant errors associated with the measurement of the charge transfer cross sections.

Separation of the 3s, 3p, and 3d States

Table 7 gives Q_{3p}/Q_{3s} and Q_{3d}/Q_{3s} for nitrogen, argon, hydrogen, and helium. For values deleted by "----" no measurement was performed; for values deleted by "...." measurements were attempted but there was insufficient statistical accuracy to warrant a meaningful separation of the state in question.

Comparison of Q_{3s} for N_2, Ar, H_2, and He

Table 8 summarizes the observed ratios for the 3s state cross sections. Here, Q_{3s} for nitrogen is normalized to unity. These relative cross sections display an interesting dependence upon energy. This

Table 7. Ratios of 3s-State Cross Sections

Proton Energy	Nitrogen		Argon		Hydrogen		Helium	
	P/S	D/S	P/S	D/S	P/S	D/S	P/S	D/S
75	.456	.076	.557	.027	.580	.009	.251	.021
100	.556	.070	.401	.031	.424	.013	.230	.025
125	----	----	.405	.029	.361	.014	----	----
150	.348	.064	.316	.049	.745	.025	.152	.008
200	----	----	.124	.065	----	----	----	----
250	.123	.084	.295	.074	1.671	....	.188	.046
300	----	----	.274	.240	2.701	....	....	.066
350	.628	.069	.541	.278	1.577	....	----	----

Table 8. Experimentally Measured Relative 3s Cross Sections

Proton Energy	Nitrogen	Argon	Hydrogen	Helium
75	1.000	1.023	.563	.352
100	1.000	.937	.353	.323
125	1.000	.850	.235	.280
150	1.000	.771	.198	.283
200	1.000	.593	.130	.257
250	1.000	.507	.119	.269
300	1.000	.434	.126	.242

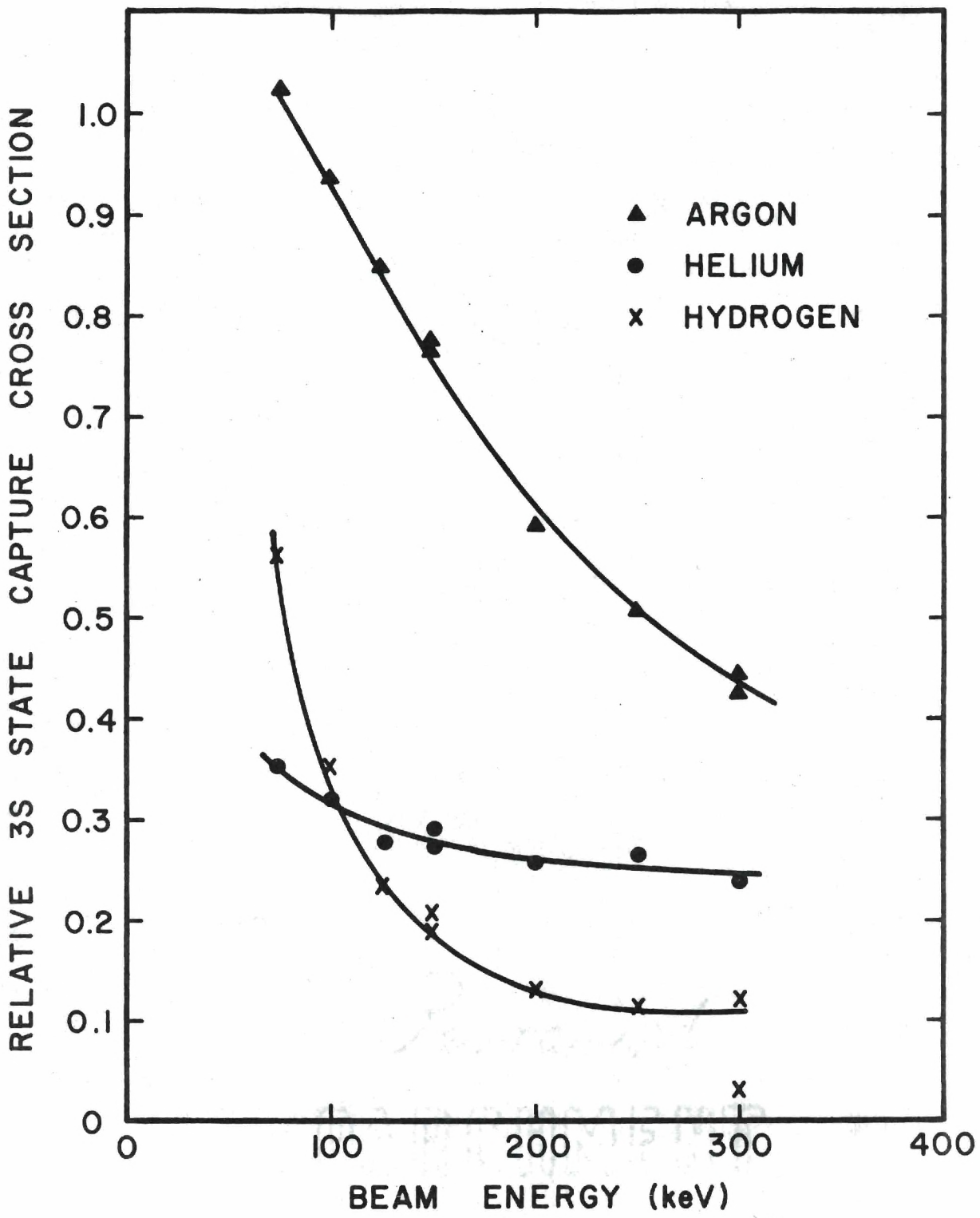

Figure 19. 3s State Charge Transfer Cross Sections for Targets of Ar, H_2 and He where the 3s Cross Section for N_2 is Unity.

is illustrated by Figure 19. Here again, Q_{3s} for nitrogen is unity; only the relative cross sections for Ar, H_2, and He are shown.

Absolute Cross Sections

From the calibration of the detection system and the data of Tables 7 and 8, the complete set of absolute cross sections can be calculated. These data, corrected for the Doppler shift and the target density profile, are summarized in Table 9. Figures 20, 21, 22, and 23 better illustrate the dependence of the cross sections upon energy.

Table 9. Absolute Cross Sections in Units of 10^{-20} cm^2

Nitrogen Target			
Proton Energy	Q_{3s}	Q_{3p}	Q_{3d}
75	452	206	34.2
100	330	183	23.0
125	213	----	----
150	138	48.0	8.83
200	60.5	----	----
250	28.9	3.44	2.34
300	14.1	----	----
350	7.48	4.70	.519
400	4.74	----	----
500	1.99	----	----
600	1.01	----	----
700	.556	----	----
Argon Target			
Proton Energy	Q_{3s}	Q_{3p}	Q_{3d}
75	462	257	12.7
100	309	124	9.50
125	181	73.1	5.29
150	106	33.6	5.26
200	35.9	4.46	2.38
250	14.1	4.17	1.05
300	6.13	1.68	1.47

Table 9. (Continued)

Hydrogen Target			
Proton Energy	Q_{3s}	Q_{3p}	Q_{3d}
75	254	148	2.26
100	117	49.4	1.49
125	49.9	18.0	.685
150	27.3	20.4	.669
200	7.88		
250	3.32	5.54	.300
300	1.78	1.17	.250
Helium Target			
Proton Energy	Q_{3s}	Q_{3p}	Q_{3d}
75	159	39.8	1.90
100	107	24.6	1.57
125	59.5	....	....
150	39.0	5.91	.312
200	15.6	....	....
250	7.50	1.39	.342
300	3.42	.224	.224
400	1.03	----	----
450	.630	----	----
550	.263	----	----

Complex Molecular Targets

The complex molecular targets were studied in three groups: $\{N_2, O_2, NO\}$, $\{O_2, CO, CO_2\}$, and $\{H_2, CH_4, C_2H_4, C_2H_6, C_3H_8\}$. Data were acquired at three energies, 75, 150, and 250 keV. The relative and absolute cross sections are given in Table 10. The absolute cross sections are determined from nitrogen and, therefore, are corrected for the Doppler shift and target density profile. Further, as for all 3s cross sections, the measurements were made at X = 44.92 cm.

Noble Gases

The cross section for 3s state capture was measured for neon at 150 keV. Thus we can compare the 3s cross sections for the first three

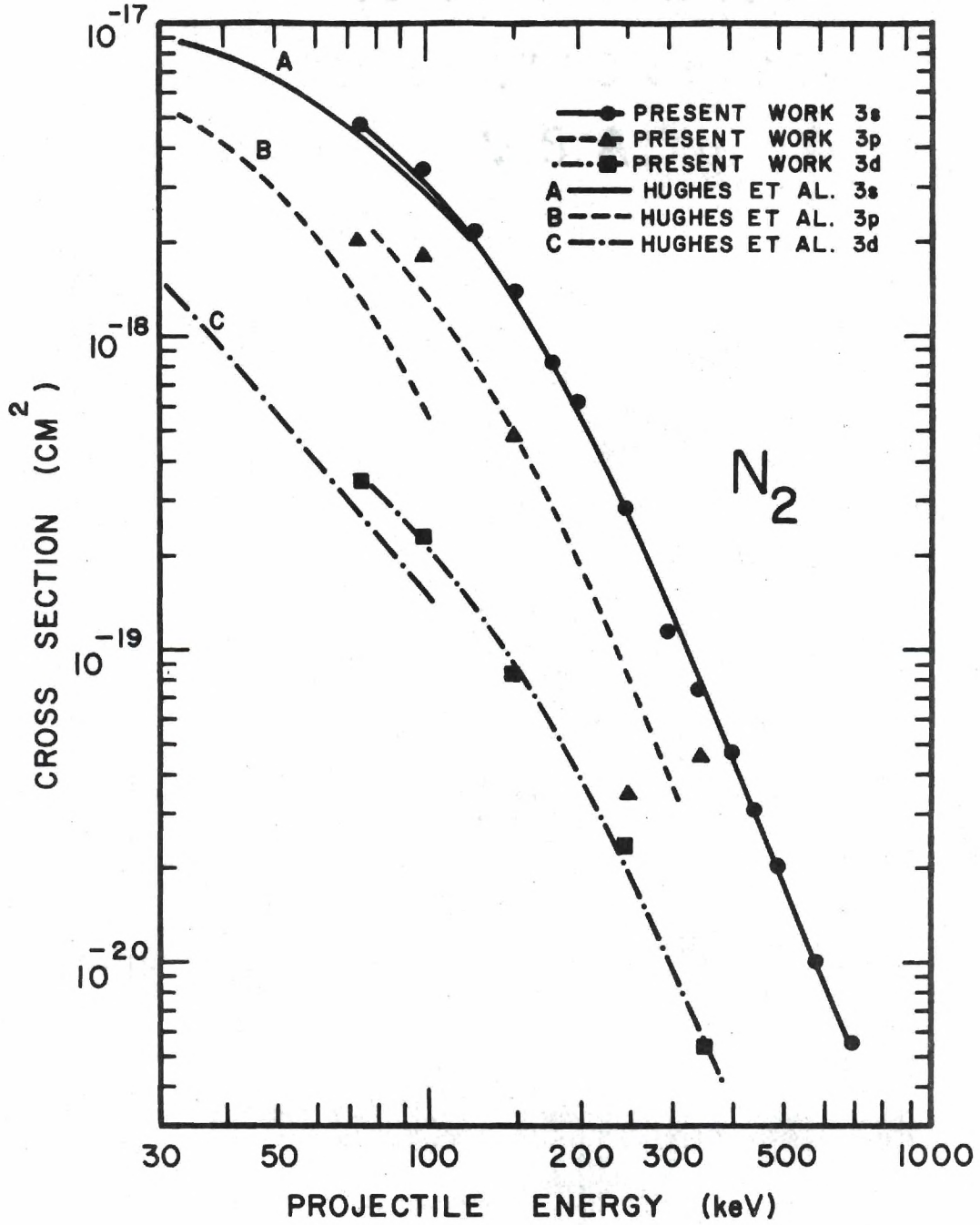

Figure 20. Absolute Cross Section for the Formation of Hydrogen in the 3s, 3p and 3d States of Excitation by the Charge Transfer Neutralization of Protons by a Target of Nitrogen. Also shown are the measurements of Hughes et al.[52]

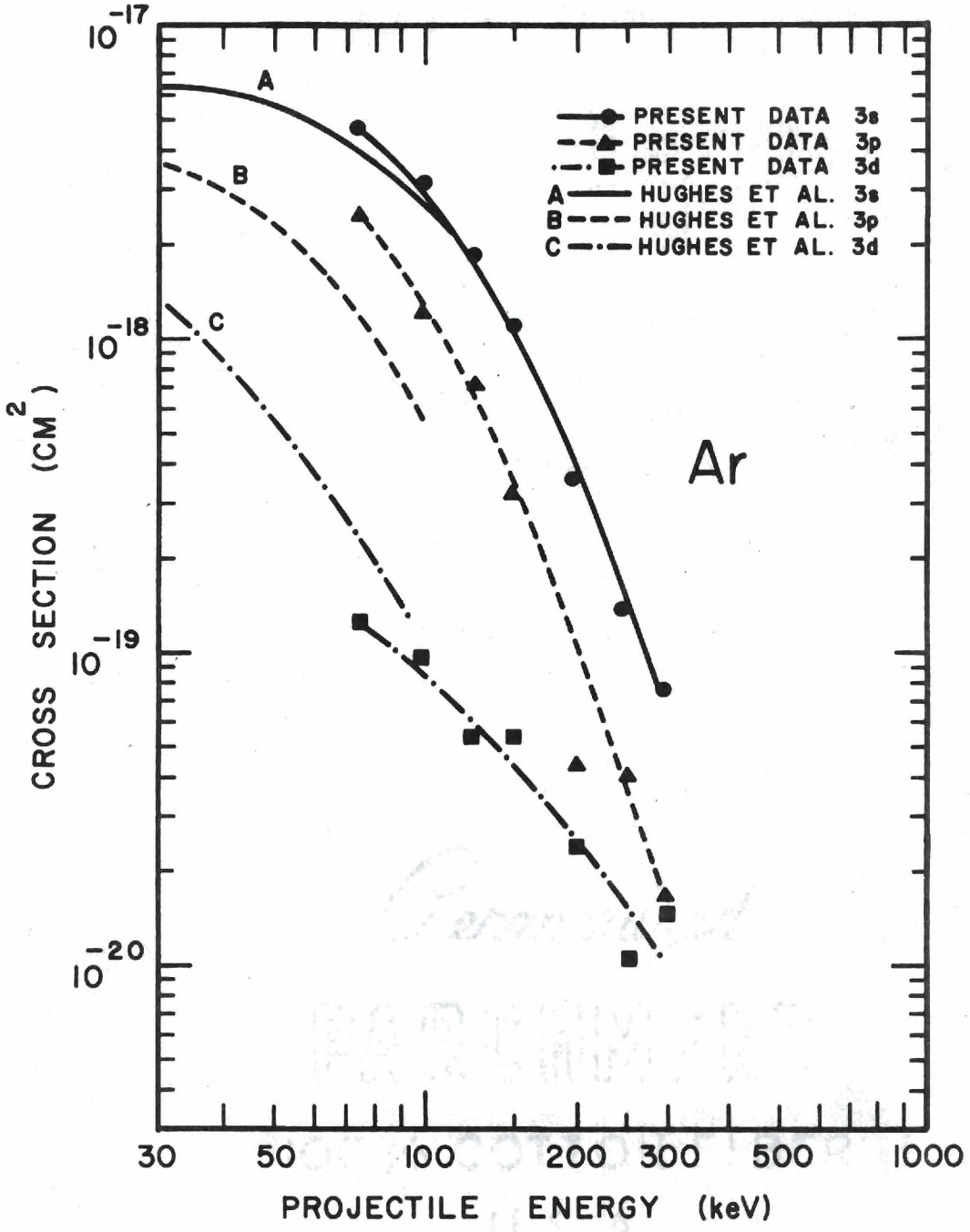

Figure 21. Absolute Cross Section for the Formation of Hydrogen in the 3s, 3p and 3d States of Excitation by the Charge Transfer Neutralization of Protons by a Target of Argon. Also shown are the measurements of Hughes et al.[32]

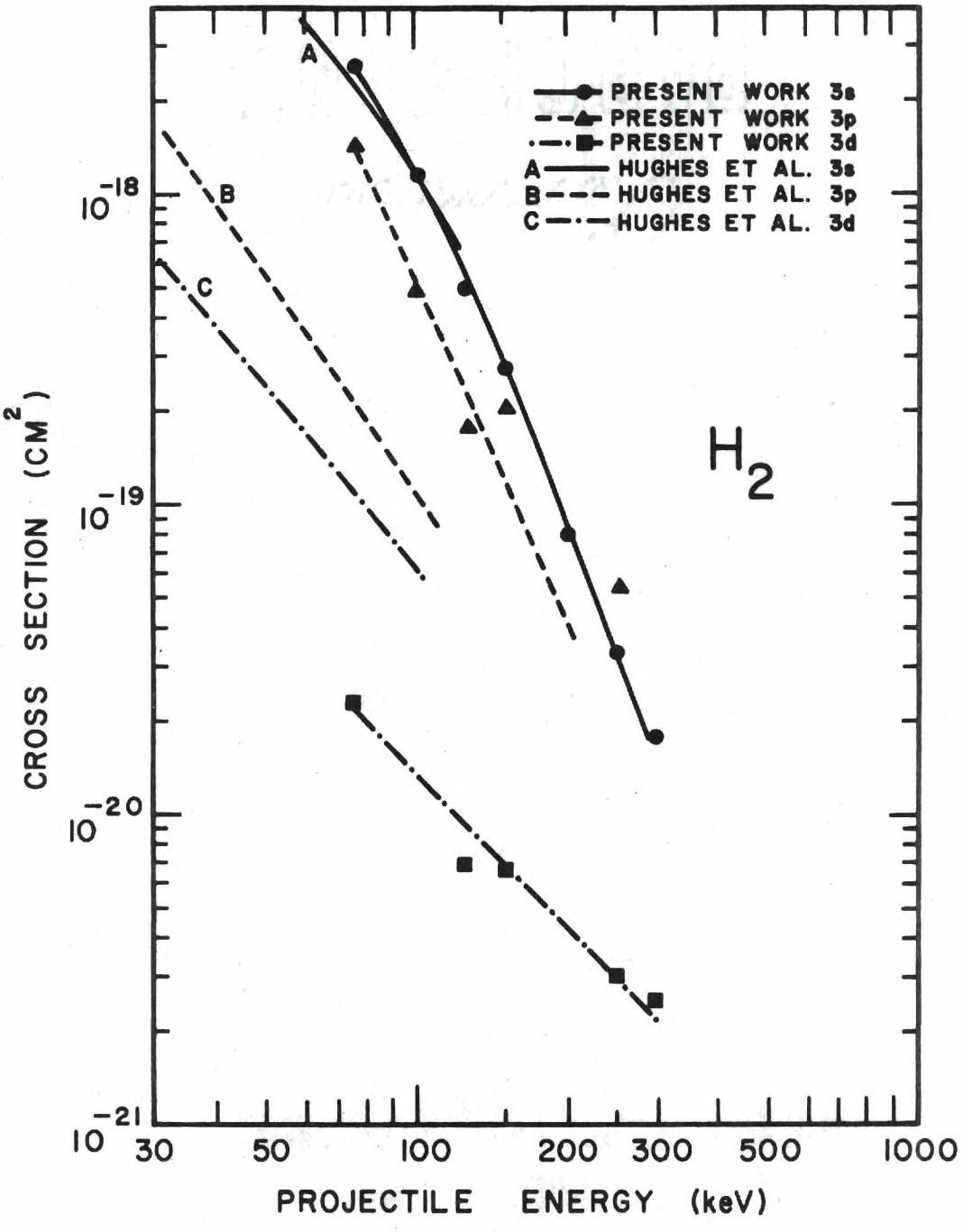

Figure 22. Absolute Cross Section for the Formation of Hydrogen in the 3s, 3p and 3d States of Excitation by the Charge Transfer Neutralization of Protons by a Target of Hydrogen. Also shown are the measurements of Hughes et al.[32]

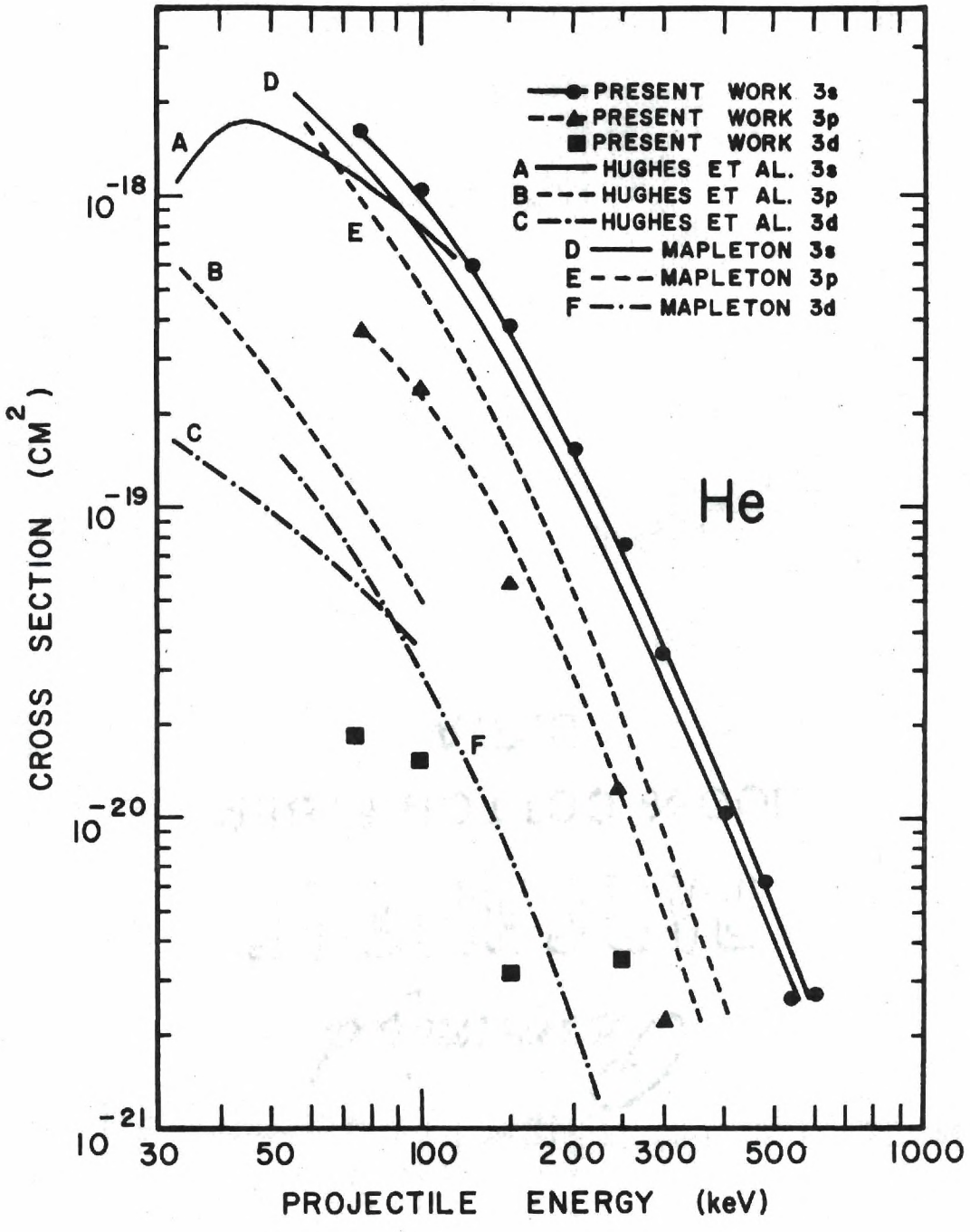

Figure 23. Absolute Cross Section for the Formation of Hydrogen in the 3s, 3p and 3d States of Excitation by the Charge Transfer Neutralization of Protons by a Target of Helium. Also shown are the measurements of Hughes et al.[32] and the theoretical cross sections of Mapleton.[9]

Table 10. 3s Cross Section for Complex Molecular Targets; Absolute Cross Sections in Units of 10^{-20} cm^2

Group 1						
Proton Energy	Cross Section	N_2			O_2	NO
75	Relative	1.00			.903	1.01
	Absolute	452			408	456
150	Relative	1.00			1.17	1.07
	Absolute	138			161	148
250	Relative	1.00			1.44	1.25
	Absolute	27.9			40.1	34.8
Group 2						
Proton Energy	Cross Section	N_2			O_2	NO
75	Relative	1.00			1.06	1.36
	Absolute	405			431	549
150	Relative	1.00			.789	1.26
	Absolute	161			127	204
250	Relative	1.00			.713	1.12
	Absolute	40.1			28.6	44.7
Group 3						
Proton Energy	Cross Section	H_2	CH_4	C_2H_4	C_2H_6	C_3H_8
75	Relative	1.00	2.45	3.02	3.43	4.41
	Absolute	254	624	768	874	1121
150	Relative	1.00	5.26	----	8.57	11.2
	Absolute	27.3	147	----	235	306
250	Relative	1.00	5.19	7.89	8.34	10.3
	Absolute	3.32	17.2	26.1	27.7	34.3

noble gas atoms. These cross sections are given in Table 11.

Table 11. 3s State Cross Sections for Noble Gas Atoms at 150 keV; Absolute Cross Sections in Units of 10^{-20} cm^2

Proton Energy		He	Ne	Ar
150	Relative	1.00	2.31	2.73
	Absolute	39.0	90.1	106

Deuterium

For the sake of curiosity, a comparison was made between the 3s state capture cross section for a target of deuterium and hydrogen. Deuterium appears to be seven percent higher than hydrogen. This difference is, however, within the probable error for the measurement.

Examples of Intensity Functions

An example of the intensity function, I(X), is given in Figure 24 for targets of N_2 and He at 150 keV energy. The ordinate is the observed photons per second for an initial beam current of one microampere and a target density representative of one micron of pressure at 30°C. The abscissa is the distance from the termination of the target cell to the point of observation in units of centimeters. The solid lines are the best fit intensity curves. The straight line behavior at large X is due to a single exponential decay.

Figure 25 gives a detailed deconvolution for the intensity observed for 250 keV protons onto a target of argon. The straight dashed lines are the deconvolved component intensities, I_{3s}, I_{3p}, and I_{3d}. The solid line

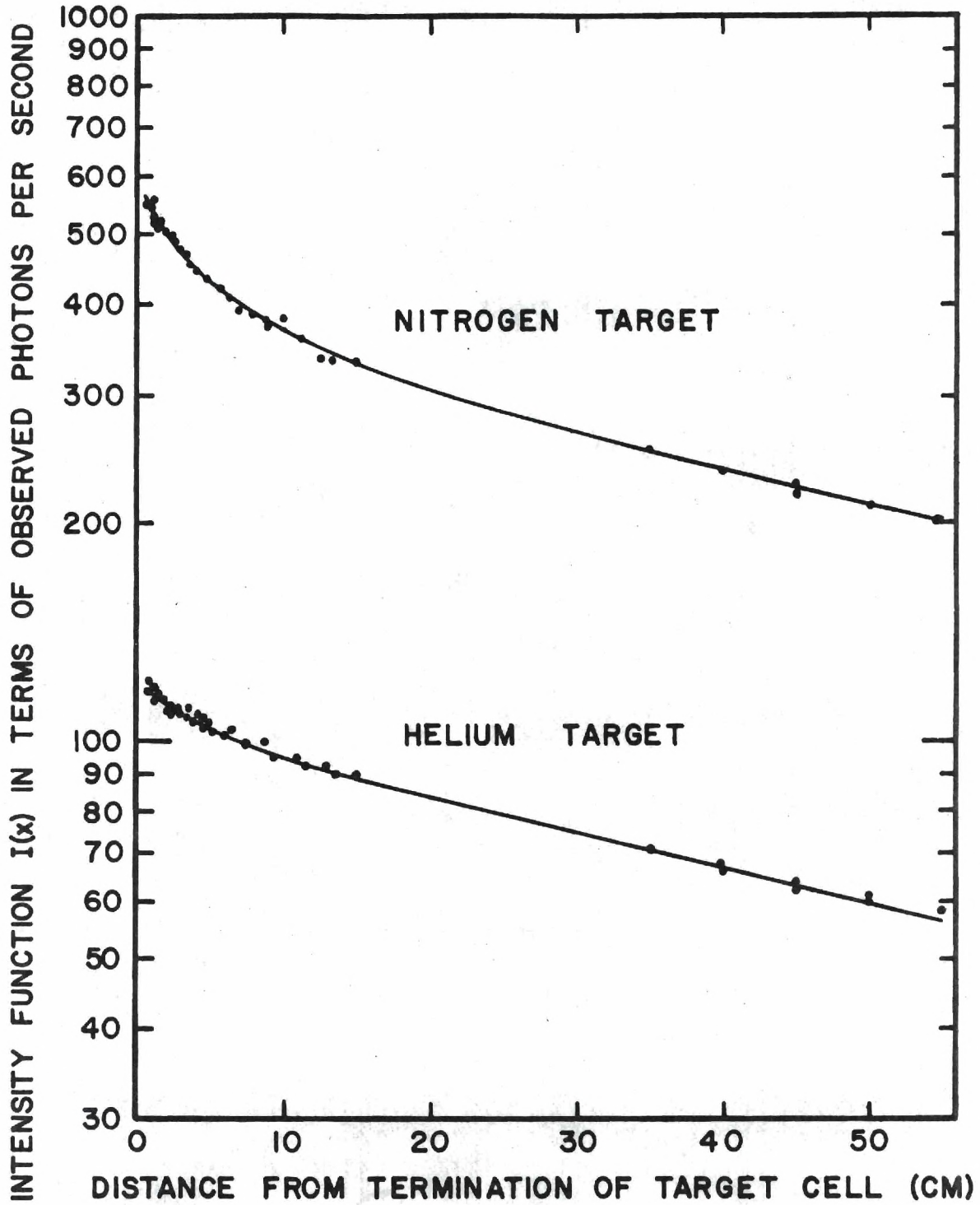

Figure 24. Samples of Balmer Alpha Radiation Intensity Functions Due to the Decay of Fast Hydrogen Atoms Produced by the Charge Transfer Neutralization of 150 keV Protons by Targets of Nitrogen and Helium.

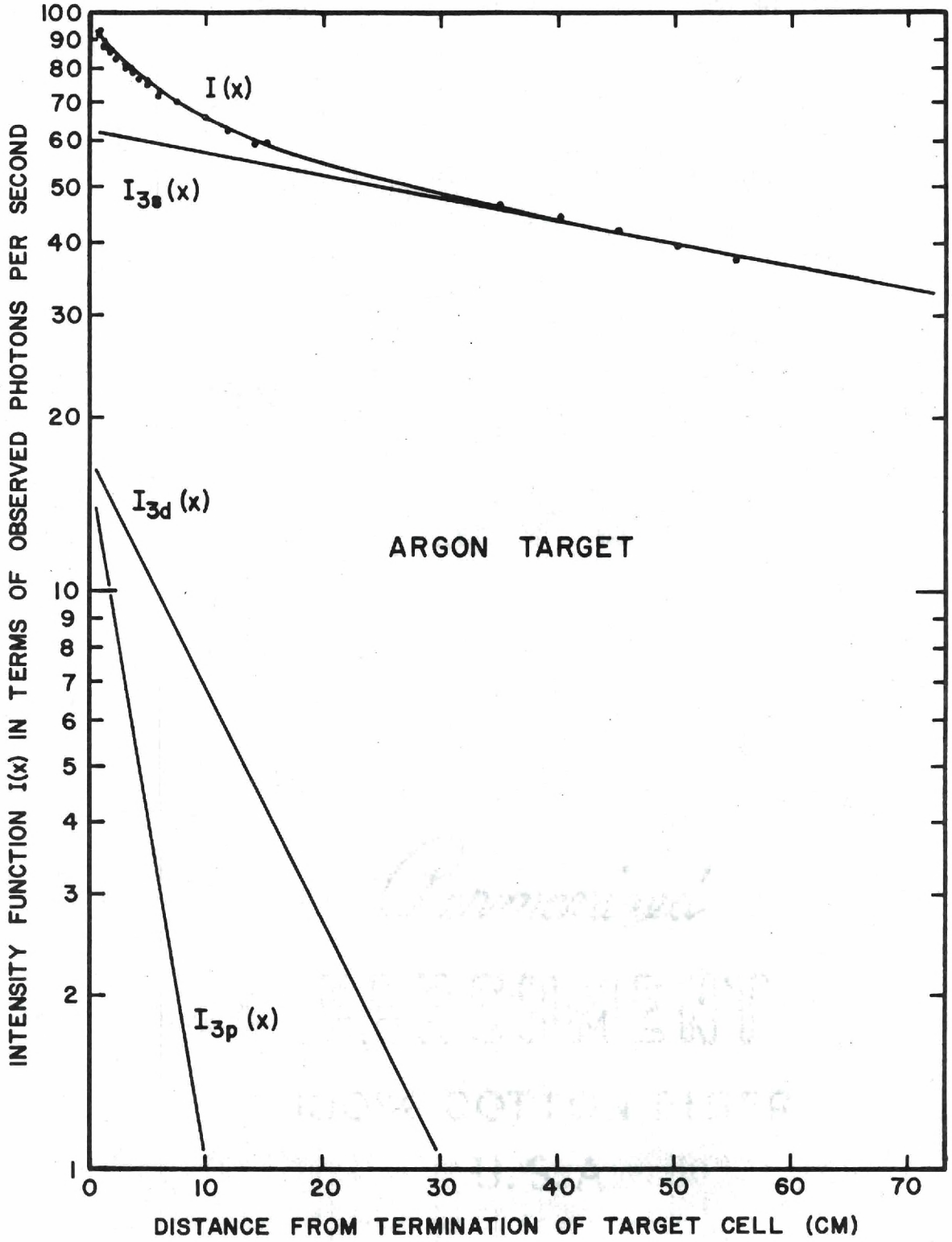

Figure 25. Sample of a Deconvolved Balmer Alpha Intensity for 250 keV Protons Neutralized by Argon.

represents the sum of these intensities. The circles are the actual data points. Here, we employ the same axes as in Figure 24.

Summary of Significant Errors

In this last section, we shall summarize the major experimental errors presented in this chapter.

Absolute Calibration Errors

Significant errors affecting the determination of the absolute cross sections arise from the calibration of the photon detection system and absolute measurement of target pressure and beam flux.

The calibration of the photon detection system is estimated to be accurate within 15 percent. The error in the measurement of target pressure is probably no greater than 6 percent. The error in the measurement of beam flux is less than 2.5 percent.

Errors in Measurement of $Q_{3\ell}$

The errors in the correction for the target density profile will have a negligible effect on the values of the Q_{3s} cross sections. Errors due to beam neutralization are estimated to be no bigger than two percent. The effects of multiple collisions are most pronounced for the 3s state cross sections for nitrogen at a beam energy of 75 keV; thus, the resultant error in Q_{3s} (due to multiple collision effects) can be considered as an upperlimit for the error due to multiple collisions for all Q_{3s} cross sections. This error is given in the next section. The errors due to multiple collisions are most likely negative for Q_{3s}. For Q_{3p} and Q_{3d} the direction of the error is uncertain.

Errors due to cascade are estimated to be no bigger than 16 percent

for the 3p and 3d cross sections and no bigger than 6 percent for the 3s cross section at all energies. Further, the errors in Q_{3p} and Q_{3d} are likely to be negative while those for Q_{3s} are likely to be positive. The limits of errors due to polarization were estimated to be -14 to +9 percent for Q_{3p} and -16 to +11 percent for Q_{3d}. By the arguments of Chapter III, there is no error in Q_{3s} due to polarization. Finally, errors in the Doppler shift corrections will have essentially no effect on the values of the Q_{3s} cross sections.

Errors in Q_{3s}. Errors in the measurement of Q_{3s} are due primarily to the natural statistical fluctuations in the intensity, I(X) and the effects of multiple collisions mentioned in the preceding chapter. The errors due to multiple collisions are largest for nitrogen and, for this case, they never exceed 5 percent. The errors due to statistics are summarized in Table 12.

Errors in Q_{3p} and Q_{3d}. The Q_{3p} and Q_{3d} cross sections are effected most severely by random statistical errors in I(X). The errors in Q_{3p} and Q_{3d} were obtained, with aid of the model calculations of Chapter II, as a function of the initial value of I(X) and the approximate (measured) ratios, C_{3s}/C_{3s}. For a given measurement, the initial value of I(X) will depend not only upon the actual cross sections, Q_{3s}, Q_{3p}, and Q_{3d} but also the operating target cell pressure and beam current.

For helium, the 3p and 3d contributions to I(X) are very small; hence, for this target the accuracy of Q_{3p} and Q_{3d} is generally low. For the same reason, the errors in the measurement of Q_{3d} for H_2 are large. Additional difficulties are encountered in the measurement of Q_{3p} for hydrogen due to large background signals resulting from the interaction of

Table 12. Errors in Q_{3s} Due to Statistical Fluctuations in I(X)

Energy	Percent Error For Target Of			
keV	N_2	A	H_2	He
75	6	5	5	8
100	8	8	9	11
125	7	9	13	12
150	4	7	14	12
200	4	7	12	8
250	3	4	14	6
300	5	8	30	25
350	5	----	----	----
400	8	----	----	15
450	7	----	----	----
500	8	----	----	16
550	20	----	----	50
600	----	----	----	50
700	35	----	----	----

the beam with hydrogen escaping from the target cell.

Finally, the accuracy is highest for nitrogen and argon. Not only do these targets yield larger p to s and d to s cross section ratios but the Q_{3s} cross section is considerably larger than for H_2 and He. (See Figure 19).

In Table 13 we summarize the errors in Q_{3p} and Q_{3d} associated with statistical fluctuations in I(X).

Table 13. Errors in Q_{3p} and Q_{3d} Due to Statistical Fluctuations in I(X)

Energy	Percent Error in Q_{3p} and Q_{3d}							
	N_2		Ar		H_2		He	
	Q_{3p}	Q_{3d}	Q_{3p}	Q_{3d}	Q_{3p}	Q_{3d}	Q_{3p}	Q_{3d}
75	10	6	18	12	12	49	44	58
100	10	7	19	21	15	58	56	70
125	----	----	17	13	22	96	----	----
150	11	8	16	12	30	130	56	78
200	----	----	30	22	----	----	----	----
250	22	18	34	28	40	200	100	160
300	----	----	58	47	50	200	110	180
350	45	38	65	54	50	200	----	----

CHAPTER V

COMPARISON OF RESULTS WITH OTHER AVAILABLE EXPERIMENTAL AND THEORETICAL DATA

In this final chapter we shall compare the present results with the currently available experimental and theoretical data. As we shall point out, these results are in good agreement with the only available experimental data which overlaps our energy range, 75 - 700 keV, and in reasonable agreement with existing theory.

In the last section of this chapter, we shall discuss our results for the formation of 3s hydrogen by the more complex molecular targets. Particular attention will be paid to the failure of the additive cross section rule found for total neutralization cross sections.

Experimental Data

Measurements of Hughes

The high energy data of Hughes[32] represents the only available work which can be directly compared to the results presented here. Hughes' measurements were made using a field free time-of-flight technique (similar to the technique employed here) which is discussed in Chapter II.

The present measurements are compared with those of Hughes[32] in Figures 20, 21, 22, and 23. On these graphs, the curves labeled A, B, and C represent the data of Hughes for the 3s, 3p and 3d states respectively. Generally, there appears to be a slight overall disagreement with Hughes of about 5 percent due to a difference in the overall absolute calibration

of the two experiments. This discrepancy is, however, well within the estimated limits of accuracy for our calibration procedure.

For all four targets, N_2, Ar, H_2, and He, the 3s state cross sections are in excellent agreement. The 3d states are in reasonable agreement, considering the large inherent error in the measurement of Q_{3d}. For the 3p states, on the other hand, Figures 20, 21, 22, and 23 all show a systematic disagreement with Hughes. We can give no satisfactory explanation for this difference. However, failure to consider the target density profile (Chapter III) will generally introduce negative errors in the measurement of Q_{3p}. These errors become larger in magnitude at lower energies. For the present experiment, the correction necessary for the 3p state is about 6 percent at 75 keV. If a larger diameter cell exit orifice is used, the error will increase in size substantially. The design of the exit orifice is determined by the speed of the pumping systems in the observation chamber and the characteristics of the beam collimation. If Hughes employs larger orifices (which might be the case since he quotes smaller cell to observation chamber pressure ratios, 60:1) and fails to account for the depression in the target density profile he would, indeed, measure 3p cross sections smaller than ours. Our cross sections, being consistently larger than Hughes', are in better agreement with the theory of Mapleton[9].

Although the data of Hughes are the only experimental measurements which can be compared directly with our results, a brief review of other related measurements might be instructive.

Measurements of Andreev

Using the Stark Effect method discussed in Chapter II, Andreev et al[4]

have measured the charge transfer cross sections for formation of the 3s, 3p and 3d states below 30 keV. These measurements are in good agreement with Hughes for the 3s state. The 3p state compares well in magnitude with Hughes but shows a distinctly different dependence upon energy. Andreev's 3d state is considerably larger than Hughes (by a factor of about four).

Measurements of Berkner for n = 6 States

Berkner[33] has measured the Balmer delta radiation ($n = 6 \rightarrow n = 2$) from a beam of protons (and also deuterons) neutralized by targets of Mg and Ne at impact energies below 70 keV. It is doubtful that a meaningful interpretation of these data can be made in terms of the $Q_{6\ell}$ cross sections.

Measurement of n = 2 States

The balance of the investigation of the formation of excited hydrogen by the electron capture of protons has been concerned with the formation of the n = 2 states. This case has been studied extensively. The bulk of this work has been done for energies below 40 keV.

Comparison with Theory

There are presently no available theories describing the formation of 3ℓ state hydrogen by the charge transfer neutralization of protons by targets other than atomic hydrogen and helium. For helium, there is only one theory describing the formation of the n = 3 states, the Born Approximation treatment of Mapleton[9], which we shall discuss in this section. In addition to the calculations of Mapleton, there are a few other theories which might be extended to our data; we shall also review briefly some of these theoretical treatments.

Born Approximation of Mapleton

Mapleton[9] has carried out calculations for the formation of 3s, 3p and 3d hydrogen from protons neutralized by helium atoms at energies from 7 to 1000 keV. By employing Born's approximation, he calculates capture cross sections for both "prior" and "post" collision potentials. Mapleton chooses a rather simple helium wave function:

$$\psi(r_1, r_2) = \frac{Z^3}{4\pi a_o^3} \exp - (Z/a_o)(r_1 + r_2) \qquad (92)$$

with Z = 1.6875

The calculations are carried out for a number of final target states (1s, 2s, and 2p) for capture into the 1s, 2s, and 2p states. As we mentioned earlier, our cross sections represent a sum over all possible final target states. Mapleton's 1s, 2s, and 2p data suggest a rapid convergence of the cross section when summed over these target states. For example, his data indicates that about 90 percent of all electron capture processes leave the target in the ground state of the resulting ion. We shall assume, therefore, that comparing our data (for all final target states) with Mapleton's 3ℓ cross sections for a target left in the ground state is valid to within ten percent.

Comparison with the Experimental Results for Helium. Figure 23 compares Mapleton's calculations with our results for helium. The agreement for the 3s state is excellent becoming nearly exact beyond 250 keV. This agreement might indicate that the Born approximation is basically sound in this energy region.

Mapleton's 3p cross section is considerably higher than our

experimental measurements. Table 14 compares the experimental and theoretical p to s cross section ratios.

Table 14. Experimental versus Theoretical p to s Charge Transfer Cross Section Ratios

Energy (kev)	Experimental Ratios p to s	Theoretical Ratios For Prior Calculations	Theoretical Ratios For post Calculations
75	0.251	0.79	0.77
100	0.230	0.67	0.68
150	0.152	0.52	0.53
250	0.188	0.35	0.37

We note that while there is a large disagreement for p to s ratios, experiment and theory tend to merge with increasing energy. For example, at 75 the ratios differ by a factor of 3.2; at 250 keV, they differ by a factor of only 1.7.

The accuracy of the 3d cross section measurements is too small to make quantitative comparisons with theory. Qualitatively, however, theory and experiment are in agreement -- that is to say Q_{3d} is only a few percent of Q_{3s}. This is illustrated by Table 15.

Table 15. Experimental versus Theoretical d to s Charge Transfer Cross Section Ratios

Energy (keV)	Experimental Ratios d to s	Theoretical Ratios For Prior Calculations	Theoretical Ratios For Post Calculations
75	0.01	0.050	0.049
100	0.02	0.039	0.039
150	0.008	0.026	0.027
250	0.05	0.014	0.013

Conclusions. It is possible to compare our experimental cross sections for helium to Mapleton's Born approximation calculations for charge transfer leaving the target in the ground state. Our data are in excellent agreement for the formation of 3s states and in qualitative agreement for 3d states. The 3p state cross sections are consistently lower than theory. Experiment and theory do tend to merge at high energy.

One might conjecture that the disagreement regarding the 3p states might be resolved by the use of a better helium wave function. It is a well established fact that post and prior calculations agree when the wave function is exact. For the theoretical calculations quoted here, the post and prior agreed to within 20 percent for all the cross sections determined (for capture into the states 1s, 2s, 2p, 3s, 3p, and 3d). Mapleton[34] has recalculated the charge transfer cross sections for formation of ground state hydrogen by an He target using a six parameter Hylleras wave function for the target. This calculation yields post and prior differences of less than one percent. A calculation of the 3ℓ cross sections based on this wave function might yield a more realistic 3p cross section. It should be pointed out, however, that the work of Bransden and Sin Fai Lamb[35] for the formation of 1s hydrogen indicates that the cross section is, in general, not particularly sensitive to the type of helium wave function employed. Recently, this conclusion has been confirmed by Salin[36].

Calculations of Hiskes

Using a simplified form of the Brinkman - Kramers matrix element, Hiskes[37,38] has calculated the ratio of $Q_{n\ell}$ to the total cross section, Q_n, for a number of different targets. In these calculations, the target system electrons are described by Hartree - Fock wave functions. Both

post and prior interaction potentials are employed.

Hiskes' results are in qualitative agreement with Mapleton above 30 keV. Thus, his predications for the 3p cross section are too large to be agreement with the measurements presented here. For example, for Q_{3p}/Q_{3s} Hiskes obtains values of 0.7, 0.6 and 0.4 for energies of 60, 100 and 140 keV respectively.

Calculations of Brandsden and Sin Fai Lam

It might be argued that more coupling between states describing the active (transferred) electron duringthe collision process would yield better capture cross section than those presented by Mapleton. In Mapleton's calculations, the state for the transferred electron is initially represented by one ℓ eigen state. This evolves into the final bound hydrogenic state during the collision process. These final states determine the formation cross sections, Q_{3s}, Q_{3p}, and Q_{3d}. It is possible to describe the transferred electron by a more complete state with two initial and two final components. Such calculations have been carried out by Brandsden and Sin Fai Lam[10] for capture into the n = 2 level using an impact parameter formulation.

Comparison with Experiment. If these results are scaled to the n = 3 case (by multiplying by 8/27) using the n^{-3} rule[11], very good agreement is obtained for the ratio of p to s capture cross sections. For example, at 100 keV the scaled cross sections yield a p to s ratio of about 0.27; this is in very good agreement (within 17 percent) with our measurement of 0.23 (see Table 7). If the p to s ratios of Table 7 are extended graphically, one might easily expect the p to s ratio to go below 0.1; at 400 keV the scaled cross sections suggest a value of about 0.07.

The magnitude of the cross sections are in excellent agreement at 100 keV. The scaled cross sections suggest a value of about 1.06×10^{-18} (see Table 9).[2] Unfortunately, the scaled cross sections suggest a value of Q_{3s} of 1.7×10^{-20} at 400 keV.[2] This is about 70 percent higher than our measurement for Q_{3s}.

Conclusion. The scaled $Q_{2\ell}$ cross sections of Brandsden and Sin Fai Lam[10] yield p/s ratios which appear to be in agreement with our measurements. Further, our experimental values of Q_{3s} lies between the scaled cross sections and the results of Mapleton[9]. The experimental values agree better with the scaled cross sections at low energy. At high energy, the scaled cross sections appear to be too large; the experimental values merge with the results of Mapleton's one state approximation.

These results suggest strongly that the inclusion of a multistate approximation will force Mapleton's calculations into even closer agreement with experiment. Hopefully, such calculations will be made in the future.

Interpretation of Molecular Hydrogen Data

There are a number of calculations giving the factional contributions to the total n = 3 capture cross section due to the various 3ℓ cross sections, $Q_{3\ell}$. In this section we shall compare, briefly, these calculations with our measurements for molecular hydrogen.

Experimental Data

It is not possible to make meaningful comparisons with theory for Q_{3p} beyond 150 keV for molecular hydrogen. Accurate measurements of Q_{3p} at energies beyond 150 keV were not possible. This was due to the relatively rapid decrease in cross section with energy (see Figure 19) and an increasing percent contribution to I(X) due to background emission. This

background emission was produced by the interaction of the beam with H_2 gas from the target cell.

Comparisons with Theory

A number of estimates of the p to s cross section ratios for atomic hydrogen targets have been obtained by Bates and Dalgarno[39], Mapleton[40], May[41], and Jackson and Schiff[42]. These results are all in general agreement. Here, we shall quote a few results of Mapleton and May.

Using both the Born and Brinkman - Kramer approximations, Mapleton determined the ratio Q_{3p}/Q_{3s} for impact energies between 60 and 2000 keV for atomic hydrogen targets. His results are higher than our experiments would suggest. For example, at around 100 keV he predicts a ratio of 0.8 as opposed to our experimental value for H_2 of 0.4. At 600 keV, theory predicts a ratio of about 0.2. Our first three measurements of Q_{3p}/Q_{3s} (at 75, 100 and 125 keV) show a systematic decrease in Q_{3p}/Q_{3s}. Our larger values of Q_{3p}/Q_{3s}, beyond 125 keV, are most likely a result of the error effects discussed in Chapter II.

May has calculated Q_{3p}/Q_{3s} and Q_{3d}/Q_{3p} for energies between 59 and 550 keV. At around 100 keV, his data suggests a value of about 1 for Q_{3p}/Q_{3s} but, again, the ratio decreases with energy to about 0.2 at 550 keV.

For Q_{3d}/Q_{3s} May calculates a value of 0.09 at 150 keV. This ratio decreases slowly with energy to about 0.01 at 550 keV. This is qualitatively similar to our experimental observations.

Complex Molecular Targets

Toburen et al.[43] and Dague et al.[44] have successfully interpreted total capture and ionization cross sections for H^+ and H projectiles

impacting with a variety of different gases in terms of a simple additive rule. This rule assumes that at high impact velocities the projectile sees the molecular target as an assemblage of separate atoms; thus, molecular forces are assumed to be unimportant in the charge transfer process. For this simple additive rule, the cross section for the molecular target, A_nB_m, is taken to be:

$$Q(A_nB_m) = n\,Q(A) + m\,Q(B) \tag{93}$$

Here, Q(A) and Q(B) are the cross sections for the atomic targets A and B and n is the number of A atoms in the molecule A_nB_m and m the number of B atoms.

In this study, an attempt was made to fit the cross sections for formation of the 3s state to this simple additive rule. For example, using the notation of Equation 93, we might calculate the cross section for the molecule A_2B_3 from the cross sections for the molecules AB and AB_2:

$$Q(A_2B_3) = Q(AB) + Q(AB_2) \tag{94}$$

Experimental Data

If the additive rule of Equation 93 is applied to the data of Table 10, it is generally unsuccessful. The additive rule appears to give the best results for the group of targets, N_2, O_2, NO, CO, CO_2 at 150 keV. At 75 and 250 keV, the rule appears to be violated. An analysis of the cross sections for these targets does not, however, provide a conclusive test of the additive rule. This is due to the similarity of the cross sections and relatively large (1.5 to 5 percent) inherent experimental errors.

In order to obtain a sensitive test of the additive rule the hydrocarbons, CH_4, C_2H_4, C_2H_6, C_3H_8, were studied. For these targets the failure of the additive rule was very obvious. This failure is exemplified by the calculations of the carbon cross section from various target combinations:

$$Q_1(C) = Q(CH_4) - 2\,Q(H_2) \tag{95}$$

$$Q_2(C) = Q(C_2H_4) - Q(CH_4) \tag{96}$$

$$Q_3(C) = 2\,Q(C_2H_6) - 3\,Q(CH_4) \tag{97}$$

$$Q_4(C) = Q(C_3H_8) - 2\,Q(CH_4) \tag{98}$$

$$Q_5(C) = 3\,Q(C_3H_8) - 4(C_2H_6) \tag{99}$$

We summarize the calculations for the carbon cross sections in Table 16.

Table 16. Application of Additive Rule to Hydrocarbon Targets for 3s State Cross Sections at 75, 150 and 250 keV. Q_i is in Units of 10^{-20} cm^2

Energy (keV)	Q_1	Q_2	Q_3	Q_4	Q_5
75	+116	+114	-124	-127	-133
150	+92.4	...	+29	+12	-22
250	+10.6	+8.9	+3.8	-0.1	-7.9

Conclusion

It is definitely established that the simple additive rule described

by Equation 93 does not apply to the formation of 3s hydrogen by the neutralization of protons by targets of H_2CH_4, C_2H_4, C_2H_6 and C_3H_8. Recently, Wittkower and Betz[45] have found that the additive rule does not apply for electron capture by 12 Mev iodine ions onto targets of H_2, N_2, O_2, CO_2, N_2O, CH_4 and $(CH_2)_3O$. They conclude:

"for fast heavy ions, an ion velocity high enough to allow the molecular binding in the target to be overcome is not a sufficient criterion for the applicability of an additive rule for charge changing cross sections."

As a partial explanation for the difference between their results and the results of Toburen and Dagnac, they point out that there are a number of fundamental differences between H+ and I+ projectiles:

1. Large forces are exerted on the target by a heavy projectile; this may increase the importance of the role played by the inner electrons of the target.

2. The possibility exist for the target interacting simultaneously with more than one of the projectiles electrons.

3. Excitation of the projectile is possible; this may effect the charge changing process even after the collision has occurred.

From our data, we can only conclude that failure of the additive rule for formation of the excited state suggest some fundamental difference in the charge transfer process leading to neutralization into the ground state as opposed to the process leading to an excited state.

There is one interesting parallel between our studies and the work of Wihkower and Betz; in both experiments, the predicted cross sections are generally smaller than the measured cross sections. This becomes increasingly more obvious for the heavier targets, C_2H_6 and C_3H_8. One might expect that this could be due to the attenuation effects caused by

multiple collisions but, in this experiment, precautions were taken to avoid these effects. We can offer no explanation for this behavior other than to point out that, clearly, the molecular properties of targets are becoming more important for the more complex systems.

In addition to additive rule of Equation 93, a number of other simple rules were investigated (such as one based on the ionization potentials of the target systems). No satisfactory results were obtained; in general, no individual properties of the atomic constituents were found to predict the cross section of the collective system.

APPENDIX I

EXPERIMENTAL MEASUREMENT OF COLLISIONAL EXCITATION AND DESTRUCTION CROSS SECTIONS

Procedures for Measuring Cross Sections

Since the intensity function, $I(\rho,X)$, can be calculated exactly for the case of multiple collisions, we can, in principle, determine all the cross sections, $Q_{3\ell}$, $Q_{I;3\ell}$, and $Q_{X;3\ell}$, by fitting the complete intensity, $I'(\rho,X)$, to the observed experimental intensity. From Equations 18 and 37, $I'(\rho,X)$ is given by the equation:

$$I'(\rho,X) = \sum_{\ell} U_{3\ell}(\rho; Q_{+0}, Q_{0+}, Q_{I;3\ell}, Q_{X;3\ell}/Q_{3\ell}) C(\rho, Q_{3\ell}; X) \qquad (100)$$

Because of the complicated form of $U_{3\ell}$, one is, in general, forced to employ a rather tedious non-linear iterative fitting procedure. Further, since we are dealing with nine adjustable parameters, the inherent experimental errors in the observed $I(X)$ would make the measurements quite ambiguous. It is highly desirable to reduce the number of distinct cross sections by making a few plausible assumptions. One such assumption is that Q_I and Q_X are independent of the angular momentum state ℓ. Thus we have the equations:

$$Q_{I;3s} = Q_{I;3p} = Q_{I;3d} \qquad (101)$$

$$Q_{X;3s} = Q_{X;3p} = Q_{X;3d} \qquad (102)$$

As an alternative--and perhaps more satisfactory--approach, we can devise

an experiment which separates the three 3ℓ states; the target cell configuration is ideally suited to this type of measurement.

We may generate the data necessary to determine Q_I and Q_X measuring the intensity $I(X;\rho)$, as a function of either X or ρ. By measuring I(X) vs X, we can augment our deconvolution procedure to give the best fit for the optimum values of Q_I and Q_X. Since I(X) is determined solely by natural radiative decay in a vacuum, we must, of course, make our measurement in the target region.

Observation of I(X) in the Target Region

To make this type of measurement tractable, a number of simplifying assumptions are necessary. Since $I_{3s}(X)$, $I_{3p}(X)$, and $I_{3d}(X)$ are all present in the target region, we must forfeit some credibility and assume Equations 103 and 104. Further, to reduce the complexity of I(X), it is very desirable to neglect the long decay length terms

$$- \frac{Q_{+0}}{\frac{1}{X_3} + \rho Q_I - \rho(Q_{+0} + Q_{0+})} \left(1 - e^{- \rho(Q_{+0} + Q_{0+})L}\right)$$

and

$$+ \frac{Q_X}{Q_{3\ell}} \frac{Q_{+0}}{\frac{1}{X_{3\ell}} + \rho Q_I - \rho(Q_{+0} + Q_{0+})} \left(1 - e^{- \rho(Q_{+0} + Q_{0+})L}\right)$$

The success of this approximation requires some good fortune since removal of these terms results in a singularity in $C_{3\ell}'$ of Equation 36 at a target density, ρ_∞:

$$\rho_\infty = (X_{3\ell}(Q_{+0} + Q_{0+} - Q_I))^{-1} \qquad (103)$$

The two terms mentioned above are, in fact, quite small until one get fairly close to the density, ρ_∞. To determine ρ_∞, however, one must have a prior knowledge of Q_I. For a nitrogen target and a decay length of 84.903 cm (150 keV energy), the singularity occurs at 1.09 microns of pressure (temperature $\approx 30°C$) if Q_I is assumed to be 6×10^{-16} cm^2 and $Q_X = 0$. At a target pressure of 0.50 microns, however, the approximation is good to within 7.6 percent.

After the theoretical form of I(X), has been simplified, the experimental data can be deconvolved for a number of Q_I values. The Q_I yielding the best fit to the data can be taken to be the correct value; this fit, in turn, gives the three cross sections, $Q_{3\ell}$.

Following this approach, Edwards[8] measured Q_1 for N_2 and He in the energy range 75 to 400 keV. Q_X is assumed to be zero; hence, it is possible that these values of Q_I are too small.

Observation of I(X) as a Function of Target Pressure beyond the Target Region

In the present experiment, it was possible to isolate $I_{3s}(X)$ by making observations at a sufficiently large distance from the termination of the target cell. Therefore the assumption of Equations 102 and 103 was not necessary. Furthermore, the measurement of Q_I and Q_X required the variation of ρ, the parameter, which is more intimately associated with the multiple collision processes. It was also possible to retain all the terms in Equation 36.

The analysis for Q_I and Q_X can be described as follows: the position, X, was held constant. The Balmer alpha emission from the beam was recorded for several different pressures by the techniques described previously. A special Algol program was written for the reduction of this data which

included corrections for beam neutralization.

From the measurements of $I(\rho)$ vs ρ, the program constructed the empirical attenuation function, $U_{3s}^{e}(\rho; Q_I, Q_X/Q_{3s})$. A model function $U_{3s}^{T}(\rho)$ (calculated from Equations 36 and 37) was fitted to the empirical function, $U_{3s}^{e}(\rho)$, by systematically varying Q_I and Q_X/Q_{3s}; the optimum fit (governed in part by the experimental errors in ρ and $I(\rho)$) then determined Q_I and the value of Q_X/Q_{3s}.

Summary of Results

Due to the limitation of time, only the cross section for argon was investigated. $I(\rho,X)$ was measured over a pressure range of from .1 to 3.0 microns; the accuracy of the experiments would be enhanced considerably by extending this pressure range.

$Q_{I:3s}$ and $Q_{X:3s}$ were measured for a beam energy of 75, 150, and 250 keV. The results of these measurements are summarized in Table 17 and 18. Here, r is the ratio of the RMS deviation between the trial and experimental curves and the estimated RMS experimental error averaged over the data points. ϵ is the estimated experimental RMS error in $I(\rho)$ average of all the data points, $\{I(\rho),\rho\}$. Ideally, r should be equal to unity.

Table 17. $Q_{I;3s}$ and $Q_{X:3s}/Q_{3\ell}$ versus Energy

Energy (keV)	$Q_{I;3s}$ (cm^2)	$Q_{X:3s}/Q_{3\ell}$	r	
75	2.1×10^{-5}	10	1.18	3.4
150	2.1×10^{-5}	54	1.05	1.2
250	1.5×10^{-15}	180	1.31	2.9

As expected, one measures smaller values for $Q_{I:3s}$ if $Q_{X:3s}$ is assumed to be zero. These values of $Q_{I:3s}$ are given in Table 19.

Table 18. Absolute Values of $Q_{X:3s}$ as calculated from Table 9

Energy (keV)	$Q_{X:3s}$ (cm^2)
75	4.6×10^{-17}
150	5.7×10^{-17}
250	2.5×10^{-17}

Table 19. Values of $Q_{I:3s}$ for $Q_{X:3s} = 0$

Energy (keV)	$Q_{I:3s}$	r
75	4.7×10^{-16}	1.77
150	6.3×10^{-16}	1.59
250	7.0×10^{-16}	1.31

In general, the quality of the fit is not particularly sensitive to the actual value of $Q_{X:3s}$. Unfortunately, changes in $Q_{X:3s}$ do result in substantial changes in $Q_{I:3s}$ as revealed by Tables 17 and 19. At higher energies the experiment becomes even less sensitive to $Q_{X:3s}$. In fact, at 250 keV r for $Q_{X:3s}/Q_{3s} = 0$ differs only by a neglible amount from the r value for the optimum value of $Q_{X;3s}/Q_{3s}$; the determination of $Q_{X:3s}$, at this energy, is not conclusive.

It should be remembered that these cross sections are deduced from second order effects and are, as a result, not well determined. The error

in Q_I may be as high as 200 percent. Q_X should be considered as an order of magnitude estimation of the true value.

Interpretation of Cross Section

As we pointed out in Chapter III, $Q_{X:3s}$ and $Q_{I:3s}$ represent a number of possible processes. It may, however, be possible to interpret these cross sections simply in terms of fundamental cross sections.

Collisional Excitation

The collisional excitation term in Equation 35 is proportional to $F^oQ_{X:3s}$. The quantity, $Q_{X:3s}$, is an effective cross section grossly describing the production of 3s hydrogen atoms by neutral excitation. We can express $F^oQ_{X:3s}$ in terms of fundamental quantities:

$$F^o\, Q_{X;3s} = F^o \sum_{n'\ell' \neq 3,0}^{n'} \sum_{\ell'} f^{n'\ell'}\, q^{n'\ell'}_{X;3s} \tag{104}$$

Here, $f^{n'\ell'}$ is the fractional component of total neutral flux, F^o, due to atoms in the $n'\ell'$ state. $q^{n'\ell'}_{X:3s}$ is the cross section for the collisional production of a 3s atom from an incident neutral in the $n'\ell'$ state. If none of the partial cross sections, ($q^{20}_{X:3s}$, $q^{21}_{X:3s}$, $q^{31}_{X:3s}$, $q^{32}_{X:3s}$, $q^{40}_{X:3s}$...), are much larger than $q^{10}_{X:3s}$, then, $Q_{X:3s} \approx q^{10}_{X:3s}$ since f^{10} is about 0.9 times F^o. Thus, we may claim that it is very likely that the measured $Q_{X:3s}$ is approximately equal to the cross section for collosional excitation of ground state atoms.

There is very little available information concerning the collisional excitation of ground state neutrals. Bates and Griffing[46] have

calculated the cross section for the reaction.

$$H(1s) + H(1s) \rightarrow H(1s) + H(3s) \tag{105}$$

Their results indicate that $Q_{X:3s}$ for a hydrogen target maximizes around 30 keV and then falls off steadily with increasing energy. At 100 keV, they predict a cross section of about 1.6×10^{-18} cm^2. Increasing the energy to 200 keV reduces $Q_{X:3s}$ to about 1.8×10^{-19}.

Hughes[47] has measured $Q_{X:3s}$ for a molecular nitrogen target in the energy range 5 to 35 keV. The cross section maximizes to about 4×10^{-18} near 15 keV. It then appears to decrease slowly with increasing energy. In light of these data, it would appear that our values of $Q_{X:3s}$ are much too large.

Collisional Destruction

The collisional destruction cross section $Q_{I:3s}$ can also be expanded into partial cross sections.

$$Q_{I;3s} = \sum_{\substack{n' \\ n'\ell' \neq 3,0}} \sum_{\ell'} q^{n'\ell'}_{I;3s} + q^{+}_{I;3s} \tag{106}$$

$q^{n'\ell'}_{I;3s}$ represents the collisional production of a $n'\ell'$ atom from an incident 3s neutral. $q^{+}_{I:3s}$ represents the cross section for electron stripping for a neutral in the 3s state.

Bates and Walker[14] have calculated the stripping cross section for 3s neutrals using a classical impulse approximation. They imply that $q^{+}_{I;3s}$ dominates the expression for $Q_{I:3s}$; further, they suggest that $q^{+}_{I:3s} \approx q^{+}_{I:3p} \approx q^{+}_{I:3d}$. Calculations are given for $q^{+}_{I:1s}$ as a function of energy for targets of N_2, Ar, and He. In addition, $q^{+}_{I:3s}(E)$ is given for

nitrogen.

Our values of Q_I are much larger than those predicted by Bates and Walker. Their theoretical cross sections are more commensurate with our values of Q_I neglecting neutral excitation (setting $Q_X/Q_{3s} = 0$).

The large values for the measured $Q_{I:3s}$ cross sections may suggest that Bates and Walker's assumption,

$$q^+_{I;3s} >> \sum_{n'\ell' \neq 3,0}^{n'} \sum_{\ell'} q^{n'\ell'}_{I;3s} \tag{107}$$

is not valid in this case.

Very recently, Levy[48] has calculated the total collisional quenching cross section for metastable H(2s) atoms onto Argon at high energies. These cross sections are larger than Bates and Walkers ionization cross sections describing the quenching of H(3s). In fact, Levy's 2s quenching cross section is about the same as our measured values for the 3s quenching (destruction) cross section. Further, Levy's theoretical predictions are also in good agreement with Dose, Meyer and Sulzman's[49] experimentally measured 2s quenching cross sections.

APPENDIX II

FORMATION OF HYDROGEN IN THE 3s, 3p AND 3d STATES OF EXCITATION BY THE COLLISIONAL DISSOCIATION OF H_2^+ AND H_3^+ PROJECTILES

In this Appendix we shall discuss briefly the measurement of the cross sections for producing 3s, 3p and 3d hydrogen by the collisional fragmentation of H_2^+ and H_3^+ projectiles by helium atoms. (See Equations 2 and 3.)

Experimental Technique

The experimental technique employed to measure the cross sections, $Q_{3\ell}$, for dissociation is essentially the same as for charge transfer. Equation 17 describes the intensity, I(X), produced by the dissociation of molecular ions. The population factors, $C_{3\ell}$, are given by Equation 18 as before.

The analysis of the deconvolution procedure, given in Chapter II, does not apply here. The ratios of the initial population factors are quite different in the case of dissociation. For example, for the dissociation of H_2^+ ions the ratios, C_{3p}/C_{3s} and C_{3d}/C_{3s}, are on the order of 1 and 5 respectively.

In general, the intensity, I(X), can be measured much more accurately for dissociation because of larger cross sections. There does appear to be more beam scattering in this case but, generally, the divergent component of the main beam could be maintained at less than two percent of the total.

Interpretation

The discussion of interpretation in Chapter II applies, in general, to the case of dissociation. However, there are a few additional remarks necessary.

Target Density Profile

Corrections for the target density profile have been made for the case of dissociation. (See Figure 11.) For a given incident projectile energy, the excited atoms in the beam have a lower velocity than in the case of atoms produced from charge transfer neutralized protons. As a result, the excited atoms spend more time in transit through the exit orifice of the target cell. Since there is a severe target density depression in this region, there is an appreciable loss of the short lifetime p state population. In fact, the p state cross section could not be measured at the lower energies.

Multiple Collision Effects

For dissociation, multiple collision effects might conceivably be more complicated than suggested by Equations 35 and 36. However, plots of $I(X, \rho)$ versus target cell pressure at X = 45 cm. were very linear in the range of pressures used to measure the dissociation cross sections; therefore, for these measurements we assume single collision conditions prevailed.

Cascade

One might expect cascade to be a more serious problem for dissociation than for charge transfer. First, there is no reason to expect the cross sections for formation of the n = 4 states to be smaller than those for n = 3. Secondly, our present data for the formation of the n = 3

states suggest that all the ℓ states are produced in a similar abundance as opposed to charge transfer where the 3s state predominates. Since the branching ratio for decay into 3d level is unity for the 4f state, this state is most likely the largest contributor to cascade. Attempts were made to include the 4f level into the analysis of I(X). There appeared to be some small 4f contribution (some deviation from a pure 3s state decay at large X) but the inclusion of the 4f decay term did not appreciably alter the measured 3ℓ cross sections. The cross sections presented here neglect cascade; errors due to cascade should be within the errors quoted for the $Q_{3\ell}$ measurements.

Internal Excitation of Molecular Ion Projectiles

With molecular ions we are faced with an additional problem--namely the internal excitation of the projectiles prior to collision. Molecular ions, such as H_2^+ and H_3^+, can be rotationally and vibrationally excited. It is certainly possible that the 3ℓ state formation cross sections, $Q_{3\ell}$, depend upon these initial states of internal excitation.

The distribution of internal states of excitation is probably influenced most by the ion source conditions. It is not possible to assess these distributions for the RF discharge source employed in this experiment. Attempts were made to observe changes in I(X) due to a variation in source pressure; no changes in I(X) were observed.

It might be possible to produce molecular ion beams with known distributions of vibrational states using electron impact ionization sources. Unfortunately, the output from electron impact sources of reasonable size would not be sufficient for this experiment.

Projectile Orientation

Finally, we should point out that it is most likely that the orientation of the molecular ion is an important factor in the dissociation processes. The present experiment provides no information on the incident ion orientation with respect to the beam axis.

Summary of Results

The results of the dissociation experiments are given in Tables 20 and 21. These cross sections are subject to the same absolute errors mentioned in Chapter IV. Because $I_{3d}(X)$ constitutes a large percentage of I(X), the 3d cross sections were measured much more accurately than those for the charge transfer. We assign an estimate error of 15 percent for all the 3d cross sections. For 3s cross section we assign an error of about 20 percent.

As we mentioned earlier, the 3p cross section could not be determined except at high energy. For the 3p cross sections presented here, we assign a larger error of 50 percent.

Figures 26 and 27 illustrate the dependence of the 3 cross sections upon energy. These cross sections do not show striking decrease in cross section with increasing energy displayed by the charge transfer data.

Hughes[50] has studied the dissociation of H_2^+ ions for a number of target gases below 120 keV. Our Q_{3s} data of H_2^+ onto He are in good agreement with his measurements.

The data for H_2^+ projectiles shows a similar energy dependence to the total cross section for the formation of neutral hydrogen atoms by dissociation of H_2^+ as measured by McClure[51]. Unfortunately, there are no additional experimental or theoretical data to which our present measurements can be compared.

Table 20. Absolute Cross Sections (in units of 10^{-20}) for the Formation of 3ℓ Hydrogen Atoms by the Collisional Dissociation of H_2^+ ions by Helium.

Energy (keV)	Q_{3s}	Q_{3p}	Q_{3d}
75	221	....	284
100	201	....	277
150	188	....	233
200	182	110	181
300	133	104	152
400	112	158	125
500	107	160	127
700	82.1	96	105

Table 21. Absolute Cross Sections (in units of 10^{-20} cm^2) for Formation of 3ℓ Hydrogen Atoms by the Collisional Dissociation of H_3^+ ions by Helium

Energy (keV)	Q_{3s}	Q_{3p}	Q_{3d}
100	312	....	673
150	318	....	376
200	274	....	323
300	237	....	270
400	111	....	237
500	177	235	183
600	153	289	161
700	134	....	187

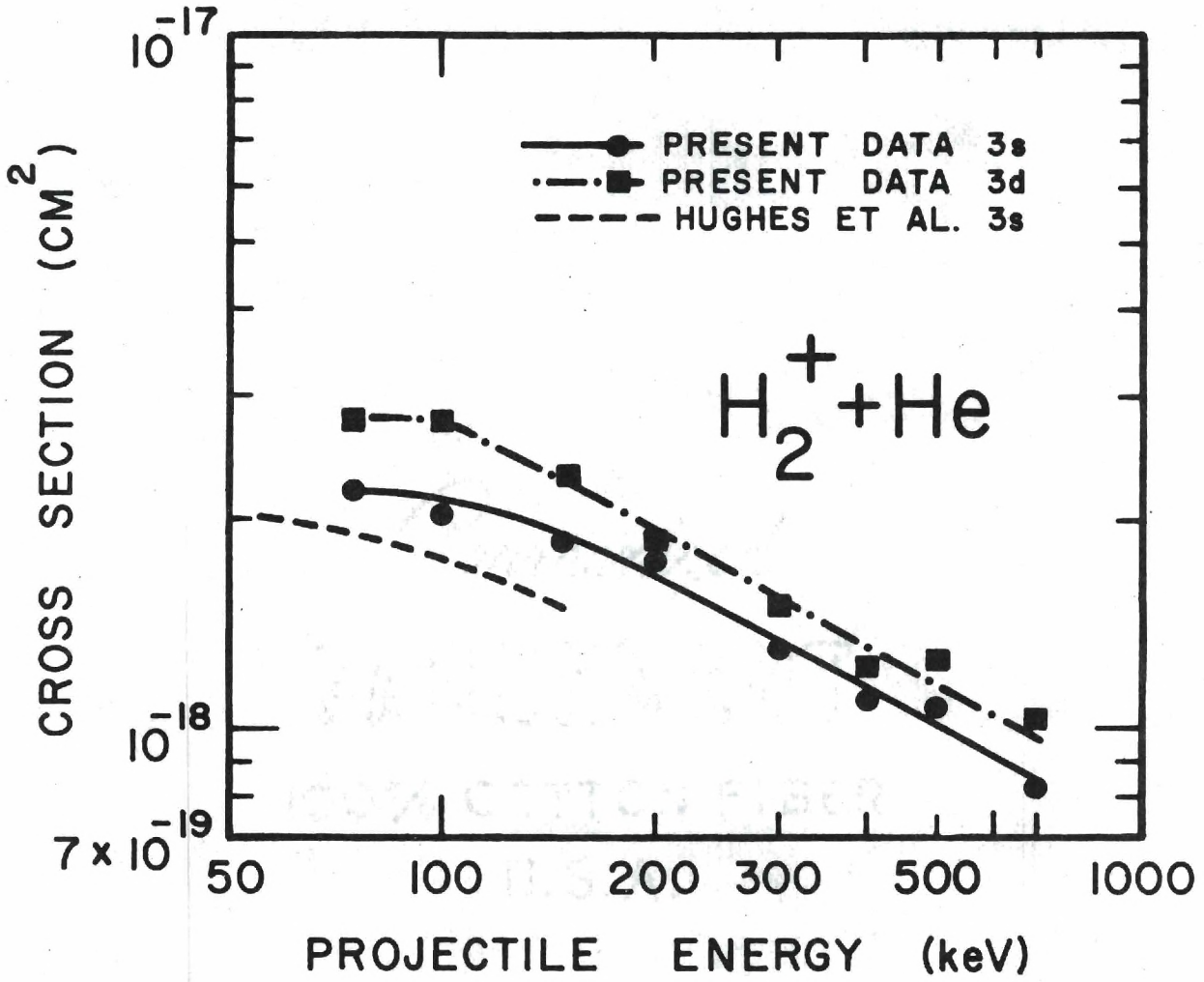

Figure 26. Absolute Cross Section for the Formation of Hydrogen in the 3s and 3d States of Excitation by the Collisional Dissociation of H_2^+ Projectiles Resulting from Impact with Helium Atoms. Also shown are the measurements of Hughes et al.[50]

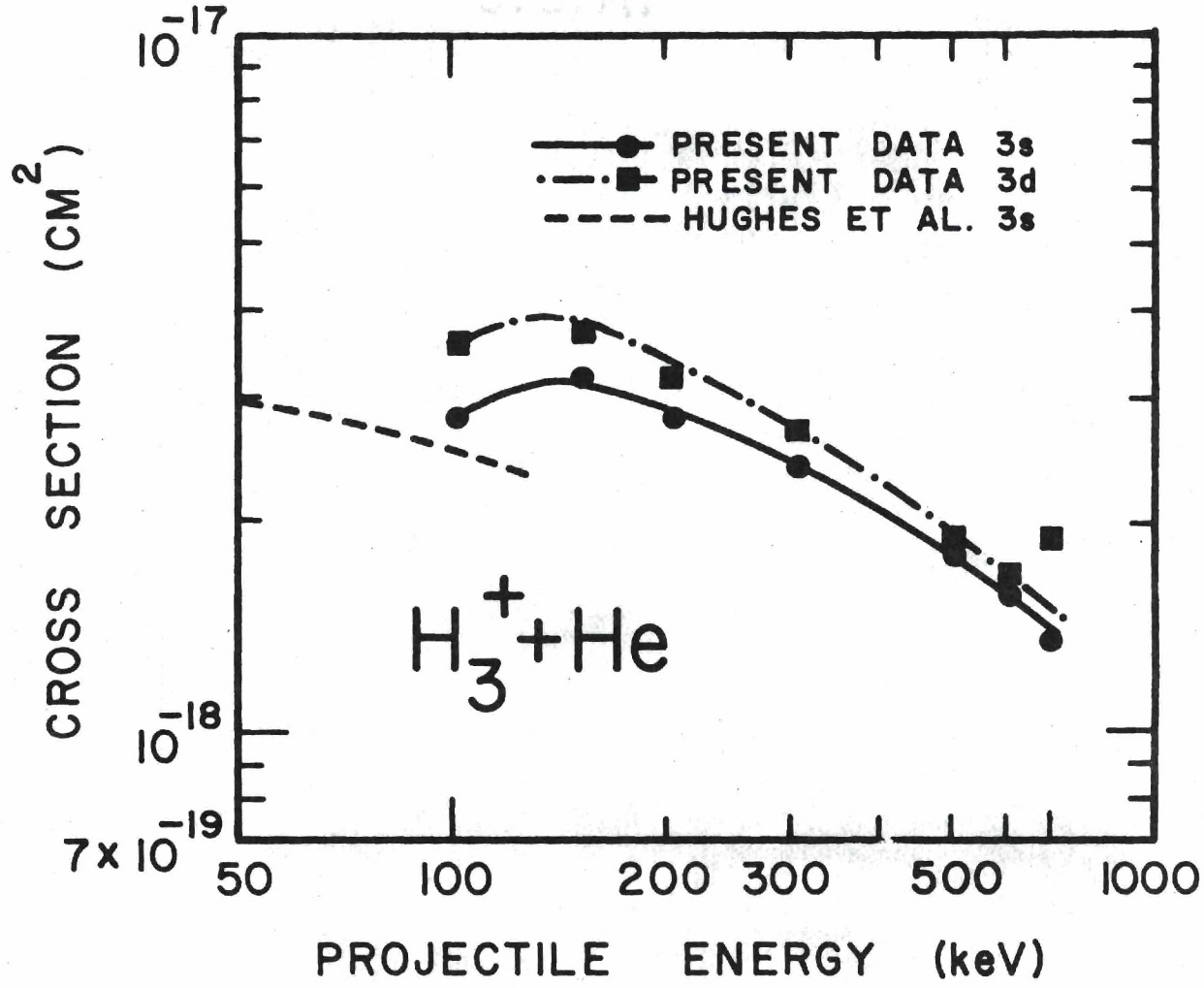

Figure 27. Absolute Cross Section for the Formation of Hydrogen in the 3s and 3d States of Excitation by the Collisional Dissociation of H_3^+ Projectiles Resulting from Impact with Helium Atoms. Also shown are the measurements of Hughes et al.[50]

APPENDIX III

CALCULATION OF THE LIFETIME OF STARK PERTURBED STATES OF DEFINITE j AND n

In this Appendix we shall discuss very briefly the calculation of the lifetime of the n = 3, j = 3/2, m_j states arising from the perturbation of the $3p_{3/2}$ and $3d_{3/2}$ states by static electric fields.

Time Independent Treatment

The $3p_{3/2}$ and $3d_{3/2}$ states are separated in energy only by the Lamb shift. This shift, ΔE_L can be represented by a phenomenological Hamiltonian, $\mathcal{H}_L$[52], which has the following properties:

$$\mathcal{H}_L \left| 3p_{3/2} \right\rangle = 0 \tag{108}$$

$$\mathcal{H}_L \left| 3d_{3/2} \right\rangle = \Delta E_L \left| 3d_{3/2} \right\rangle \tag{109}$$

We assume the perturbed states, $|E\pm\rangle$, are superpositions of $|3p_{3/2}\rangle$ and $|3d_{3/2}\rangle$:

$$|E_{\pm}\rangle = C^{\pm}_{3p} \left| 3p_{3/2} \right\rangle + C^{\pm}_{3d} \left| 3d_{3/2} \right\rangle \tag{110}$$

These states ($|E_{\pm}\rangle$) must obey the time independent Schrodinger equation:

$$\mathcal{H}_T \left| E_{\pm} \right\rangle = E_{\pm} \left| E_{\pm} \right\rangle \tag{111}$$

The total Hamiltonian, $\mathcal{H}$; can be resolved into three parts: the field

free Hamiltonian, $\mathcal{H}$, the Stark perturbation Hamiltonian, $\mathcal{H}_s$, ($\mathcal{H}_s = e|\vec{E}|Z$) and $\mathcal{H}_L$.

$$\mathcal{H}_T = \mathcal{H}_0 + \mathcal{H}_S + \mathcal{H}_L \tag{112}$$

Equation 111 can be written as a matrix equation by applying the states $\langle 3p_{3/2}|$ and $\langle 3d_{3/2}|$. This matrix equation (and the corresponding secular equation) determines the energy eigenvalues $E_{\pm}$. Further, we can find the ratio of $C^{\pm}_{3\ell}$ coefficients:

$$\frac{C^{\pm}_{3p}}{C^{\pm}_{3d}} = \frac{\frac{H^S_{3p,3d}}{\Delta E_L}}{1 \pm 1 + 4\frac{H^S{}^2_{3p,3d}}{\Delta E_L}} \tag{113}$$

Here, $H^S_{3p,3d}$ is the Stark matrix element, $\langle 3p_{3/2}|eZ|\vec{E}||3d_{3/2}\rangle$.

We can define a critical field to be that field for which

$$H^S_{3p,3d}/\Delta E_L = 1 \tag{114}$$

For fields greater than the critical field, the ratios $C^{\pm}_{3p}/C^{\pm}_{3d}$ tend toward unity; hence, $|3p_{3/2}\rangle$ and $|3d_{3/2}\rangle$ appear in $|E_{\pm}\rangle$ in equal amounts. When this is the case, the total probability for decay of the state, $|E_{\pm}\rangle$, can be taken to be $(A(3p_{3/2}) + A(3d_{3/2}))/2$. The corresponding lifetime is

$$\tau_{E_{\pm}} = \frac{2}{A(3p_{3/2}) + A(3d_{3/2})} = 0.786 \times 10^{-8} \text{ sec.} \tag{115}$$

Time Dependent Treatment

It is possible to treat this problem by using a time dependent

Hamiltonian. In this case, the radiative decay of the states is taken into account by introducing a radiative damping Hamilton with imaginary eigenvalues:

$$\mathcal{H}_D \, |3p_{3/2}\rangle = \frac{-ih}{2} A(3p_{3/2}) \, |3p_{3/2}\rangle \tag{116}$$

$$\mathcal{H}_P \, |3d_{3/2}\rangle = \frac{-ih}{2} A(3d_{3/2}) \, |3d_{3/2}\rangle \tag{117}$$

This leads to a set of two first order coupled fifferential equations for $C^{\pm}_{3p}$ and $C^{\pm}_{3d}$ [53].

$$\frac{d}{dt} C^{\pm}_{3p} = \frac{-i}{h} H^{S}_{3p,3d} \, C^{\pm}_{3d} \, e^{- i \Delta E_L t/h} - \frac{A(3p)}{2} C^{\pm}_{3p} \tag{118}$$

$$\frac{d}{dt} C^{\pm}_{3d} = \frac{-i}{h} H^{S}_{3p,3d} \, C^{\pm}_{3p} \, e^{- i \Delta E_L t/h} - \frac{A(3d)}{2} C^{\pm}_{3d} \tag{119}$$

The solutions to these equations lead to rather complicated time dependent coefficients, $C^{\pm}_{3p}(t)$ and $C^{\pm}_{3d}(t)$. By taking the right linear combination of solutions one can express the perturbed states as:

$$|E_{\pm},t\rangle = C^{\pm}_{3p}{}' \, |3p_{3/2}\rangle \, e^{-\lambda_{\pm} t} + C^{\pm}_{3d}{}' \, |3d_{3/2}\rangle \, e^{-\lambda_{\pm} t} \tag{120}$$

However, $\lambda_{\pm}$ is complex. The decay of the $|E_{\pm}\rangle$ is, in general, quasi periodic, the quasi period being a function of field.

In any real situation, it is difficult to realize the abrupt initial conditions of Equations 118 and 119 (Field - E_{max} at t = 0). In the present experiment it is not likely sharp field gradients existed for stray fields. Furthermore, oscillatory effects would tend to average out unless

the formation of the excited states and the subsequent perturbation were coherent. Using beam-foil excitation techniques abrupt field conditions can be obtained[54,55]. Further, since the formation of states takes place in a very sharply defined region (the intersection of beam and thin foil) coherent emission can be obtained. In experiments of this type oscillatory effects are observed.

In the present experiment, no oscillations in beam emission have been observed either in or beyond the target region. We assume, therefore, that a simple time independent treatment is adequate for assessing the magnitude of the effect of Stark mixing.

APPENDIX IV

THEORETICAL INTERPRETATION AND ASSESSMENT OF POLARIZATION

In Chapter III we pointed out that it is not possible to calculate the actual magnitude of the polarization of the 3p and 3d emission from the beam. Furthermore, there is no available experimental information at beam energies above 40 keV. However, the theoretical treatment of polarized emission suggests definite limits for the 3p and 3d polarization. In this appendix, we shall outline, briefly, the derivation of these limits.

In order to discuss the problem of polarization from a theoretical standpoint, we must express the cross sections for the production of the hydrogenic states, $|n = 3, \ell = 0, jm_j\rangle$, $|n = 3, \ell = 1, j, m_j\rangle$ and $|n = 3, \ell = 2, j, m_j\rangle$, in terms of the $(n\ell sm_\ell m_s)$ representation with the axis of quantization arbitrarily--but conveniently--chosen to be the beam axis X. We now must introduce the cross sections $Q_{n\ell sm_\ell m_s}$ describing the production of the various $n\ell sm_\ell m_s$ states.

Within this representation, some simplifying assumptions are immediately obvious. The beam, essentially non-relativistic, is incident with an isotropic proton spin distribution. The total spin of the target system is uncorrelated as well. Furthermore, since the interaction potentials involved in the charge transfer process are spin independent, the total spin angular momentum is conserved separately; consequently, the interaction defines no preferred spin direction and therefore $Q_{n\ell sm_\ell m_s}$ is expressed simply:

$$Q_{n\ell sm_\ell m_s} = \frac{1}{2s+1} Q_{n\ell m_\ell} \tag{121}$$

Because the system is symmetric about X, we need only consider the magnitude of :

$$Q_{n\ell sm_\ell m_s} = \frac{1}{2s+1} Q_{n\ell m_\ell} \tag{122}$$

It is possible to derive an expression for the polarization fraction, $\underline{P}_{n\ell}$, in terms of the cross sections, $Q_{n\ell m_\ell}$, for each ℓ angular momentum state. The intensity of radiation polarized along the i^{th} direction is proportional to the product of the probability per unit time for electric dipole transitions with polarization vector along the i^{th} axis, $A(3\ell sm_\ell m_s \rightarrow n = 2; i)$ and the cross section for production of the $|nlm_\ell>$ state summed over all m_ℓ values.

$$I_i = K \sum_{m\ell} A(3, \ell, s, m_\ell, m_s \rightarrow 2; i) Q_{3\ell|m\ell|} \tag{123}$$

The total radiation intensity is obtained by summing over i = X, Y, Z. By making the appropriate substitutions into Equation 56, the polarization fraction can be obtained. By taking $A(3\ell sm_\ell m_s \rightarrow 2; Y) = A(3\ell sm_\ell m_s \rightarrow 2; Z)$ and noting that the total transition probability, $A(3\ell sm_\ell m_s \rightarrow 2)$ is obtained by summing over i, Equation 52 can be expressed as:

$$\underline{P} = \frac{\sum_{m\ell} [3A(3\ell sm_\ell m_s \rightarrow 2; X) - A(3\ell sm_\ell m_s \rightarrow 2)] Q_{n,\ell|m\ell|}}{\sum_{m_\ell} [A(3\ell sm_\ell m_s \rightarrow 2; X) + A(3\ell sm_\ell m_s \rightarrow 2) Q_{n\ell|m\ell|}} \tag{124}$$

This equation can be written in terms of relative transition probabilities for the total decay of the 3_ℓ multiplet:

$$\underline{P} = \frac{3K_X - K}{K_X + K} \tag{125}$$

where

$$K_X = m_\ell \frac{3A(3\ell s m_\ell m_s \rightarrow 2;\ X) Q_{n\ell\, m\ell}}{A(3\ell s \rightarrow 2)} \tag{126}$$

$$K = m_\ell \frac{A(3\ell s m_\ell m_s \rightarrow 2) Q_{n\ell\, m_\ell}}{A(3\ell s \rightarrow 2)} \tag{127}$$

This is essentially the equation derived by Percival and Seaton[56] for the polarization fraction produced by collisional excitation. They outline the procedure for evaluating the transition probability factors for the general case of transitions between the multiplets, $s\ell$ and $s'\ell'$.

Equations 127, 128 and 129 suggest that polarization arises from unequal population of the various m_ℓ states. Thus, 3s emission is naturally unpolarized (having but one m_ℓ state). Percival and Seaton[56] calculate the polarization fraction for the decay of the 2p state:

$$\underline{P}_{3p} = \frac{Q_{310} - Q_{311}}{2.375\, Q_{310} - 3.749\, Q_{311}} \tag{128}$$

This relation holds approximately for the 3p decay. Hughes has extended the calculation to the 3d decay; he obtains the polarization fraction:

$$\underline{P}_{3d} = \frac{Q_{320} + Q_{321} - 2Q_{322}}{2.088\, Q_{320} + 3.842\, Q_{321} + 2.842\, Q_{322}} \tag{129}$$

From the multiplicity introduced by the sign of m_ℓ, we can write the n cross sections in terms of cross sections for the m_ℓ magnetic substates:

$$Q_{30} = Q_{300} \tag{130}$$

$$Q_{31} = Q_{310} + 2Q_{311} \tag{131}$$

$$Q_{32} = Q_{320} + 2Q_{321} + 2Q_{322} \tag{132}$$

Obviously we cannot calculate $\underline{P}_{3p}$ and $\underline{P}_{3d}$ without a knowledge of the m_ℓ cross sections. We can, however, estimate the range of $\underline{P}_{3p}$ and $\underline{P}_{3d}$. For $\underline{P}_{3p}$, the extremes occur when either Q_{320} or Q_{321} is zero. These conditions give polarization fractions of .421 and -.267, respectively. The limits for $\underline{P}_{3d}$ can be obtained by considering the extremes for momentum transfer to the captured electron. If the linear momentum transfer is along the X axis, there can be no angular momentum in that direction:

$$Q_{321} = Q_{322} = 0 \tag{133}$$

REFERENCES

1. R. H. Hughes, H. R. Dawson, B. M. Doughty, D. B. Kay, and C. A. Stigers, Phys. Rev. 146, 53, (1966).

2. R. H. Hughes, B. M. Doughty and A. R. Filippelli, Phys. Rev. 173, 172 (1968).

3. E. P. Andreev, V. A. Ankudinov, and S. V. Bobashev, Proceedings of the Fifth International Conference on the Physics of Electronic and Atomic Collisions, Leningrad, U.S.S.R., July 17-23, 1967 (Nauka Publishing House, Leningrad, 1967), p. 309.

4. E. P. Andreev, V. A. Ankudinov, and S. V. Bobashev, Fifth International Conference on the Physics of Electronic and Atomic Collisions, Leningrad, U.S.S.R., July 17-23, 1967 (Nauka Publishing House, 1967) p. 307.

5. E. P. Andreev, V. A. Aykudinov, S. V. Bobashev, V. B. Matveev, Sov. Phys.-JETP, 25, 232, (1967).

6. F. J. DeHeer, J. Van Eck, and J. Kistemaker, Proceedings of the Sixth International Conference on Ionization Phenomena in Gases, (SERMA, Paris, 1963), Vol. I, p. 73.

7. R. Suchannek, J. R. Murray, and J. R. Sheridan, Proceedings of the Seventh International Conference on the Physics of Electronic and Atomic Collisions, Amsterdam, Holland, July 17-23, 1971 (To be Published).

8. J. L. Edwards and E. W. Thomas, Phys. Rev. A 2, 2346, (1970).

9. R. A. Mapleton, Phys. Rev. 122, 528 (1961).

10. L. T. Sin Fai Lam, Proc. Phys. Soc., (London), 92, 67, (1967).

11. J. R. Oppenheimer, Phys. Rev. 31, 349, 1928.

12. L. D. Faddeev, Proceedings of the Fifth International Conference on the Physics of Electronic and Atomic Collisions, (Leningrad, U.S.S.R., July 17-23, 1967.

13. L. D. Faddeev, Proceedings of the Steklov Mathematical Institute, 69, 1953 (Transl.: ed. Israel Program for Scientific Translations, Jerusalem, 1965).

14. D. R. Bates and J. C. G. Walker, Planetary and Space Science, 19, 1367 (1966).

15. B. J. Eastlund and W. C. Gough, Closing the Cycle from Use to Reuse (Distributed by: Superintendent of Documents, U.S. Government Printing Office, Washington, D.C. 20402, WASH-1132) May, 1969.

16. H. Ishii and K. I. Nakayama, Transactions of the Eighth National Vacuum Symposium and Second International Congress, (Pergamon Press, Oxford 1962) p. 519.

17. T. Takaishi, Trans. Faraday Soc., 61, 840 (1965).

18. S. Dushman, Scientific Foundations of Vacuum Technique, (John Wiley and Sons, New York, 1962) Second edition pp. 58-59.

19. W. L. Wiese, M. W. Smith, and B. M. Glenon, Atomic Transition Probabilities, Volume I Hydrogen Through Neon, National Bureau of Standards, U.S. Department of Commerce, Distributed by: Superintendent of Documents, U.S. Government Printing Office, Washington, D.C. 20402, AD 634145.

20. E. L. Chupp, L. W. Dotchin and D. J. Pegg, Phys. Rev. 175 44, (1968).

21. P. M. Stier and C. F. Barnett, Phys. Rev. 103, 896, (1956).

22. C. F. Barnett and H. K. Reynolds, Phys. Rev. 109, 355 (1958).

23. V. Rojansky, Phys. Rev. 33, 1 (1929).

24. R. Schlapp, Proc. Roy. Soc. (London) A119, 313 (1928).

25. T. D. Gaily, D. H. Jaecks and R. Geballe, Phys. Rev. 167, 81 (1968).

26. W. E. Kauppila, P. J. O. Teubner, W. L. Fite and R. J. Girnius, Proceedings of the Fifth International Conference on the Physics of Electronic and Atomic Collisions, Cambridge, Massachusetts, U.S.A., July 28-August 2, 1969 (MIT Press, Cambridge, Mass.) p. 111.

27. M. O. Pace, "Absolute Experimental Cross Sections for the Excitation of Barium Ions by Electron Impact," (Thesis, Georgia Institute of Technology, 1970).

28. J. C. De Vos, Physica XX, 690 (1954).

29. J. C. De Vos, Physica XX, 715 (1954).

30. L. G. Leighton, Illuminating Engineering, Vol. LVII, No. 3, 121 (1962).

31. R. W. Wood, Physical Optics, (Macmillan, New York, 1934) Third Edition p. 784.

32. R. H. Hughes, C. A. Stigers, B. M. Doughty and E. D. Stokes, Phys. Rev. A 1, 1424, (1970).

33. K. H. Berkner, W. S. Cooper III, S. N. Kaplan, and R. V. Pyle, Phys. Rev. 182, 103, (1969).

34. R. A. Mapleton, Phys. Rev. 130 1839 (1963).

35. B. H. Bransden and L. T. Sin Fai Lam, Proc. Phys. Soc. (London) 87, 653 (1966).

36. A. Salin, J. Phys. B: Atom. Molec. Phys., 3, 937 (1970).

37. J. R. Hiskes, Lawrence Radiation Laboratory, Livermore, California, Report UCRL-50602, Unpublished.

38. J. R. Hiskes, private communication.

39. D. R. Bates and A. Dalgarno, Proc. Phys. Soc. (London) A65 919 (1952).

40. R. A. Mapleton, Phys. Rev. 126, 1477 (1962).

41. R. M. May, Nuclear Fusion, 4, 207, (1964).

42. J. D. Jackson and H. Schiff, Phys. Rev. 89, 359 (1953).

43. L. H. Toburen, M. Y. Nakai and R. A. Langley, Phys. Rev. 171, 114 (1968).

44. R. Daynac, D. Blanc and D. Molina, J. Phys. B, (London) 3, 1239 (1970).

45. A. B. Wiltkower and H. D. Betz, Seventh International Conference on the Physics of Electronic and Atomic Collisions (Amsterdam, Holland) To be Published.

46. D. R. Bates and G. Griffing, Proc. Phys. Soc. (London), A66, 961 (1953).

47. R. H. Hughes, A. R. Filippelli and H. M. Petefish, Phys. Rev. A, 1, 21, (1970).

48. H. Levy II, Phys. Rev. A, 3, 1987 (1970).

49. V. Dose, V. Meyer, and M. Salzman, J. Phys. B 2, 1357 (1969).

50. R. H. Hughes, D. B. Kay, C. A. Stigers, and E. D. Stokes, Phys. Rev. 167, 26, (1968).

51. G. W. McClure, Phys. Rev. 130, 1852, (1963).

52. H. A. Bethe and E. E. Salpeter, Quantum Mechanics of One-and-Two Electron Atoms (Academic Press, Inc., New York, 1957).

53. E. Wigner and V. Weisskopf, Z. Physik 63, 54, 288 (1930).

54. W. S. Bickel and S. Bashkin, Phys. Rev.162, 12, (1967).

55. I. A. Sellin, C. D. Moak, P. M. Griffin, and J. H. Biggerstaff, Phys. Rev. 184, 56, (1969).

56. I. C. Percival and M. J. Seaton, Phil. Trans. Roy, Soc. London, A 251, 113 (1958).

VITA

John C. Ford was born on May 27, 1944, to Mr. and Mrs. Arthur C. Ford of Atlanta, Georgia. He attended Southwest High School in Atlanta and graduated in June of 1962. In September of 1962, he entered the Georgia Institute of Technology where he received his Bachelor of Science degree in Physics in June of 1967. The following year he received a Master of Science degree in Physics.

In the Fall of 1968 he began work toward his Doctor of Philosophy degree. While working toward this degree, he was employed by the Georgia Institute of Technology as a Graduate Research Assistant.